

ANALYSIS OF SPALL PROPAGATION IN CASE HARDENED HYBRID BALL
BEARINGS

By

NATHAN BRANCH

A DISSERTATION PRESENTED TO THE GRADUATE SCHOOL
OF THE UNIVERSITY OF FLORIDA IN PARTIAL FULFILLMENT
OF THE REQUIREMENTS FOR THE DEGREE OF
DOCTOR OF PHILOSOPHY

UNIVERSITY OF FLORIDA

2010

© 2010 Nathan Branch

To Lee Patrick Branch

ACKNOWLEDGMENTS

I thank my graduate advisor Dr. Nagaraj Arakere for supporting me throughout graduate school with a sponsored project and for all of his guidance and help. Thanks also to Dr. Ghatu Subhash and Michael Klecka for all of their support, advice, collaboration, and experimental data. Sincere thanks to Dr. Nelson Forster, Vaughn Svendsen, and Dr. Lewis Rosado for all of their guidance and for supporting me during two summer internships at the Air Force Research Labs in Dayton, Ohio. Thanks also to Bob Wolfe, Dr. Bill Hannon, and Dr. Liz Cooke from Timken for supporting this project. Thanks also to David Haluck, Bill Ogden, and Herb Chin from Pratt and Whitney for sponsoring this project.

Special thanks to my graduate committee: Dr. Ghatu Subhash, Dr. Youping Chen, Dr. John Mecholsky, and Dr. Peter Ifju for reviewing my work.

Thanks also to my fellow PhD students and friends: Drew Wetzel, Shawn English, Mike Klecka, Erik Knudsen, Richard Parker, Matt and Laura Williams, Brian Wittstruck, Beth Haines, David Allen, Dan Johnson, Amanda Rollins, Amanda and Greg Hodges, Jesse and Aimee Durrance, Eban and Dani Bean, Chris Howe and Stephanie Harless, and everyone at TUMC. Thanks also to J.W. Post, Jeff Wilbanks, and all the Francos.

My utmost gratitude, however, is to my family. Thank you for supporting me throughout college and graduate school, for all of the help and advice, and for all the great memories and fun to come.

TABLE OF CONTENTS

	page
ACKNOWLEDGMENTS.....	4
LIST OF TABLES.....	8
LIST OF FIGURES.....	9
LIST OF ABBREVIATIONS.....	16
ABSTRACT.....	17
CHAPTER	
1 INTRODUCTION AND MOTIVATION.....	19
Jet Engine Performance.....	19
Bearing Design and Performance.....	20
Bearing Fatigue Failure.....	22
2 STATIC ANALYSIS OF INITIAL SPALL WIDENING.....	32
Motivation and Validation of Finite Element Model.....	32
Static Analysis of Ball over Circular Spall.....	34
Summary.....	38
3 DYNAMIC ANALYSIS OF BALL IMPACT WITH SPALL EDGE.....	39
Ball Impact with Spall Edge Drives Propagation.....	39
Finite Element Model.....	40
Finite Element Model Results.....	43
Summary.....	47
4 INDENTATION OF NON-GRADED MATERIALS.....	49
Relationship between Hardness and Yield Strength.....	49
Predicting Increase in Hardness of Strain Hardening Material.....	52
Representative Plastic Strain Background.....	55
Average Volumetric Plastic Strain as Representative Plastic Strain.....	59
Forward Analysis.....	61
Experimental Procedure.....	62
Finite Element Model.....	65
Results and Discussion.....	66
Representative Plastic Strain of an Initially Plastically Deformed Material.....	70
Key Points.....	72

5	INDENTATION OF GRADED MATERIALS.....	74
	History of Graded Materials.....	74
	Previous Methods to Determine Plastic Response of PGMs.....	76
	Proposed Method	78
	Material	81
	Experimental Procedure	82
	Constitutive Response.....	87
	Finite Element Model.....	92
	Results	93
	Variation in Strain Hardening Exponent.....	97
	Key Points	100
6	REVERSE ANALYSIS.....	102
	Nongraded Materials	102
	Experimental	105
	Analysis.....	107
	Results	111
	Key Points	116
	Reverse Analysis Graded Materials.....	116
	Experimental	117
	Variation in Flow Curve.....	119
	Key Points	130
7	SPALL MODELING	131
	Spall Propagation for 52100, M50, and M50 NiL Bearing Materials.....	131
	Finite Element Model.....	135
	Bearing Materials.....	137
	Residual Stress Profile M50 NiL.....	140
	Finite Element Model of Initial Residual Hoop Stress.....	141
	RESULTS.....	142
	M50.....	142
	52100.....	146
	M50 NiL	148
	Effects of Individual Contributions.....	150
	Residual Stress	150
	Gradient in Stress-Strain Curve.....	153
	Surface Hardness	155
	Ball Mass.....	156
	Key Points	158
	Limitations	159
8	SUMMARY.....	162
	APPENDIX: INDENTATION DATA.....	165

LIST OF REFERENCES 167
BIOGRAPHICAL SKETCH..... 171

LIST OF TABLES

Table	page
1-1 Material composition of primary alloying elements for the bearing steels in this study.....	25
1-2 Mode I fracture toughness of bearing steels in this study.	28
4-1 Tabor (1970) measured the increase in hardness of plastically deformed strain hardened materials	53
5-1 Material composition of P675 Stainless Steel.	81
6-1 The values for K , σ_y , C , and ϵ_r can be calculated for a variation in n	109
7-1 Critical stress and plastic strains for steel balls	151
7-2 No initial residual stress results in a 13.5 % increase in plastic zone depth.....	152
7-3 No residual stress results in a 10 % increase in plastic zone depth.	152
7-4 Effects of gradient in flow curve using steel balls and initial residual stresses are present.	154
7-5 Effects of gradient in flow curve using steel balls without initial residual stress present.....	155
7-6 Lower surface hardness results in larger plastic zones.	156
7-7 Both the maximum principal plastic strain and plastic zone size showed marked increases.	157
7-8 Effects of ball mass, without gradient in flow curve, and without initial residual stress.	158
7-9 Effects of ball mass, with gradient in flow curve, and with initial residual stress.	158
A-1 Micro Vickers indent field below macro indent of hard to soft PGM of P675 case hardened region.	166
A-2 Micro Vickers indent field below macro indent of soft to hard PGM of P675 case hardened region.	166

LIST OF FIGURES

Figure	page
1-1 USAF F-16 Fighter Jet	19
1-2 F-100 Pratt & Whitney Jet Engine	20
1-3 Single row deep groove ball bearings	21
1-4 Locations of ball and roller bearings of a twin-spool jet aircraft engine	21
1-5 Deformation due to contact forces between ball and raceways occurs in the form of elliptical contact patches.....	22
1-6 Stages of spall propagation.	23
1-7 Clearance created by spall allows engine shaft to misalign	24
1-8 Bearing test rig for life-endurance and spall propagation bearings at AFRL	25
1-9 Spall propagation characteristics for 52100, M50, and M50 NiL.....	26
1-10 Spall propagation trends for new (indented) bearings at 2.10 GPa maximum contact pressure.....	27
1-11 Spall propagation trends for 52100, M50, and M50 NiL at 2.41 GPa maximum contact pressure for previously life-endurance tested bearings.....	27
1-12 Initial residual stress profiles obtained by X-Ray Diffraction in hoop direction of the bearings in this study prior to installation and operation	29
1-13 Relative ball motion between leading and trailing spall edge for clockwise-rotating inner raceway.....	30
2-1 Hertzian contact solutions.....	32
2-2 Both pure-linear elastic and linear-plastic properties are used in this analysis for comparison.....	33
2-3 Symmetry exists as ball goes over circular spall	33
2-4 Maximum von Mises stresses within spall edge increase as ball approaches center of spall.	34
2-5 Cross-sections of von Mises stresses within spall edge as ball approaches spall center.	35
2-6 Maximum subsurface von Mises stresses increase as load on ball increases....	36

2-7	Maximum subsurface von Mises stresses within spall edge increase as spall diameter increases.	37
3-1	Relative ball motion causes ball impact with trailing spall edge	39
3-2	Cracks form on spall trailing edge. Typical spall depth is 127 μ m.	39
3-3	Cracks appear on the spall's trailing edge	40
3-4	Only segment of inner raceway is modeled.	41
3-5	Profilometer tracings of various spall edges.	42
3-6	Finite element model geometry and mesh.	42
3-7	Flow curve of M50 steel from in-house compression test	43
3-8	Radial stresses (11 direction) are highly compressive during ball impact.	44
3-9	Residual hoop (22 direction) stresses of cross section of impacted spall edge.	44
3-10	Residual maximum principal stress and residual hydrostatic pressure	45
3-11	Plastic zone size and maximum principal plastic strain contour at spall edge cross section after successive ball impacts.	46
3-12	Residual hoop stress profiles for blunt spall are similar to sharp spall	47
4-1	Vickers indenter geometry and linear relationship between Vickers indentation hardness and Yield strength.	50
4-2	Vickers hardness is essentially the contact pressure needed to yield the indented material for this specific indenter geometry.	50
4-3	Plastic deformation increases the yield strength and hardness of a strain hardening material.	51
4-4	Representative flow stress and plastic strain must be used in hardness measurements for strain hardening materials.	51
4-5	Vickers indentation strain-hardens the indented region, thus over-predicting yield strength of the material prior to indentation.	54
4-6	Schematic of typical instrumented indentation loading curve.	56
4-7	Average volumetric plastic strain induced by Vickers indent is independent of yield strength and elastic modulus	60

4-8	Wilson® Instruments Tukon™ 2100 B Vickers indenter and MTS® Alliance™ RT/30 machine.	63
4-9	Micro Vickers indentations within plastic zones of macro Vickers indent on P675 Core and Rockwell C indent on 303 Stainless Steel.....	63
4-10	Plot of measured increase in Vickers hardness within plastic zone of Vickers macro indent of P675 and Rockwell C indent of 303 stainless steel.....	64
4-11	Flow curves taken from compression tests of P675 and 303 stainless steels. ...	64
4-12	Finite element models of the Vickers macro indentation of P675 core and Rockwell C macro indentation of 303 stainless steel.....	66
4-13	Plastic strain contours for Vickers macro-indent of P675 stainless steel and Rockwell C macro-indent of 303 stainless steel.	67
4-14	Plastic strain contours beneath micro Vickers indents for P675 and 303 stainless steels.	68
4-15	Predicted versus measured hardness values beneath macro Vickers indent of P675 and Rockwell C indent of 303 stainless steel.	68
4-16	Vickers hardness as a function of plastic strain for P675 and 303 stainless steels.....	69
4-17	Schematic of the micro-Vickers indent of a pre-strained material.....	71
4-18	Plastic strain contours of Vickers micro-indent on pre-plastically strained P675 steel.....	72
5-1	Graded materials seen in nature (Grand Canyon) and in human-history (Japanese Katana).....	74
5-1	Schematic of the relationship between indentation hardness and plastic response at any given depth within the plastic zone of a PGM.....	80
5-2	Variation in micro-Vickers hardness with depth within a virgin P675 graded material.	82
5-3	Core region provides lower bound of possible plastic material behavior. PGM is plastically deformed by macro-Vickers indentations..	83
5-4	Wilson® Instruments Tukon™ 2100 B Vickers indenter and MTS® Alliance™ RT/30 machine.	84
5-5	Micro-Vickers indent (200 g) map within plastic zone induced by the macro-Vickers indentation	85

5-6	Experimentally measured micro-Vickers hardness along the centerline of the macro indent.....	86
5-7	MTS load frame is used to determine flow curve obtained from compression test of the homogeneous core.	87
5-8	Possible trends in strain hardening exponent, n , must converge to core value as this is the lower bound of possible plastic behavior.	88
5-9	Expanding cavity model for strain hardening materials assumes hemispherical deformation below tip of indent.	89
5-10	Strength coefficient K and Yield strength as function of depth.....	91
5-11	Power -law flow curves as function of hardness and ratio of hardness to flow stress at the corresponding representative plastic strain.	91
5-12	FE model of the macro-Vickers indentation of a PGM.....	93
5-13	Equivalent plastic strain contours within the plastic zones induced by Vickers macro-indents on hardest and softest surfaces of the PGMs.	94
5-14	Predicted versus measured micro-Vickers hardness values along the plastic zone's centerline for both hardest and softest PGMs.	95
5-15	Predicted versus measured micro-Vickers hardness values for the hardest and softest PGMs within the entire plastic zone of the macro-Vickers indentations.	96
5-16	New trend in strain hardening exponent (n) is created to determine how material properties affect predicted hardness values.	98
5-17	Representative plastic strain as function of strain hardening exponent, n	99
5-18	New trends in σ_y , K , and n allow for new flow curves to be created as function of hardness.	99
5-19	Predicted versus measured indentation hardness values for two different sets of material properties.	100
6-1	Schematic of instrumented indentation loading.	103
6-2	Micro-Vickers indents along centerline of cross section of macro-Vickers indent.	106
6-3	Measured Vickers hardness within plastic zone of macro-Vickers indent	106
6-4	Expanding cavity model for strain hardening materials assumes hemispherical deformation below tip of indent.	108

6-5	Flow curves all have same elastic modulus and virgin hardness. An increase in n must decrease σ_y to preserve same virgin hardness values.	109
6-6	Gradient in yield strength within plastic zone affects measured contact pressure.	110
6-7	FE model of the macro-Vickers indentation.	111
6-8	Load displacement curve from FE model is the same for all flow curves since virgin hardness is same for all and hardness is independent of indent depth. ..	112
6-9	Plastic strain gradient along centerline of plastic zone for all material test cases.	113
6-10	Average volumetric plastic strain induced by Vickers indent is function of n only	114
6-11	Predicted hardness values within plastic zone of macro-Vickers indents.	115
6-12	Compression test of P675 core region results in power law curve fit.	115
6-13	Virgin hardness profile for M50NiL.	118
6-14	Measured increase in Vickers hardness along centerline of plastic zone of M50 NiL.	119
6-15	For P675 in Chapter 5, all logical trends in n must converge to core value.	120
6-16	Constant strain hardening exponent with depth as two initial test cases.	121
6-17	Flow curve variation for M50 NiL virgin hardness trend.	121
6-18	Constraint factor C as function of depth for $n = 0.05$ and $n = 0.10$ trends with depth.	122
6-19	Finite element model of macro indentation of M50 NiL.	122
6-20	Constant trends in strain hardening exponent do not provide adequate match to measured hardness values.	123
6-21	Two new trends in strain hardening exponent.	124
6-22	Flow curve variation for linear gradient in n with depth.	124
6-23	Constraint factor C for linear trend in n and for Trend a.	125
6-24	“Linear” and “Trend a” test cases provide better fit to measured hardness data.	125

6-25	Trend b falls between upper and lower bounds determined by trends “linear” and “a.”	126
6-26	Variation in strength coefficient K and yield strength σ_y for Trend b.	126
6-27	Constraint factor C and flow curve variation for Trend b.	127
6-28	Equivalent plastic strain distribution along centerline of plastic zone for all test cases shown here.	127
6-29	Trend b provides best fit to predicted hardness data and falls between upper and lower bounds provided by “Trend a” and “Linear.”	128
6-30	The sensitivity to strain hardening exponent decreases with decreasing plastic strain.	129
7-1	Spall propagation characteristics for M50, M50 NiL, and 52100 bearing steels.	132
7-2	Spall propagation trends for new (indented) bearings at 2.10 GPa (305 ksi) maximum contact pressure.	133
7-3	Spalls propagate faster on life-endurance bearings.	134
7-4	Schematic showing relative ball motion between leading and trailing spall edge for clockwise-rotating inner raceway.	135
7-4	Only segment of inner raceway is modeled.	136
7-5	Finite element model and mesh of impact analysis.	137
7-6	Flow curves for 52100 and M50 steels.	138
7-7	Flow curves for M50, 52100, and the surface of M50 NiL.	138
7-8	Virgin hardness profile for M50 NiL.	139
7-9	Residual hoop stress profile for 52100, M50, and M50 NiL prior to bearing operation.	140
7-10	Compressive residual hoop stress state within raceway segment prior to ball impact.	142
7-12	Residual hoop (22 direction) stresses in proximity of spall edge.	143
7-13	Residual maximum principal stress and residual hydrostatic stress in proximity of spall edge for M50 steel	143

7-14	Plastic zone size and maximum principal plastic strain within spall edge of M50 material.....	145
7-15	Spall edge geometry from profilometer tracings. Spall edge shape is similar throughout spall propagation.	145
7-16	Residual hoop (22 direction) stresses in proximity of spall edge.	146
7-17	Residual hydrostatic stress and residual maximum principal stress in proximity of spall edge for 52100 steel.....	147
7-18	Plastic zone size and maximum principal plastic strain magnitude within spall edge of 52100 steel.....	147
7-19	Residual hoop (22 direction) stress in proximity of spall edge of M50 NiL.	148
7-20	Residual hydrostatic stress and residual maximum principal stress in proximity of spall edge for M50 NiL steel.	149
7-21	Plastic zone size and maximum principal plastic strain within spall edge of M50 NiL.	149

LIST OF ABBREVIATIONS

PGM	Plastically Graded Material
FOD	Foreign Object Debris
P675	Pyrowear 675 Stainless Steel
RCF	Rolling Contact Fatigue
FE	Finite Element
FEA	Finite Element Analysis
ODM	Oil Debris Monitor
AFRL	Air Force Research Laboratory
XRD	X-Ray Diffraction
ISE	Indentation Size Effect
AMS	Aerospace Material Specification
ECM	Expanding Cavity Model

Abstract of Dissertation Presented to the Graduate School
of the University of Florida in Partial Fulfillment of the
Requirements for the Degree of Doctor of Philosophy

ANALYSIS OF SPALL PROPAGATION IN CASE HARDENED HYBRID BALL
BEARINGS

By

Nathan Branch

August 2010

Chair: Nagaraj Arakere
Major: Mechanical Engineering

Bearings are critical to the overall performance and reliability of jet aircraft engines. Despite their optimized design, they cannot escape the damage induced by foreign object debris, improper handling, overloading, or rolling contact fatigue which can cause surface fatigue failures to occur in the form of small pits or spalls. Spalls will grow and propagate with continued engine operation and allow the main engine shaft to misalign leading to engine failure and possible loss of a multi-million dollar aircraft. Thus reducing the amount of time between initial spall formation and catastrophic engine failure is of great importance to pilot safety and mission success for military applications.

Spall propagation experiments carried out by the Air Force Research Labs show that M50, M50NiL, and 52100 bearing steels have different spall propagation characteristics. It is uncertain how certain aspects of bearing design such as initial residual stress, surface hardness, gradient in flow curve, and ball mass affect spall propagation rate. Both static and dynamic analyses will be performed here to simulate

these contributions and the bearing operating conditions during spall widening and propagation.

The variation in plastic response of plastically graded, case hardened M50 NiL bearing steel was initially unknown and it was uncertain how the plastic response will affect the spall propagation that occurs within this case hardened region. A new method will be shown here that uses indentation experiments and finite element modeling to determine the plastic response of plastically graded, P675 and M50 NiL case hardened bearing steels. The method will use a material-dependent representative plastic strain that will relate indentation hardness measurements to flow stress, which will vary with depth for a graded material. The material dependent representative plastic strain will be validated for two nongraded materials: 303 stainless steel and the core region of P675.

An analysis of the critical stresses and plastic strains that develop within a spall edge due to multiple ball impacts will be performed using finite element modeling. The results of which will predict large amounts of plastic strain and tensile residual stresses to occur where cracks appear in the actual spalled bearings. It will be shown that the contribution from ball mass has the greatest affect on the magnitude and distribution of plastic strain within an impacted spall edge which would cause 52100 bearings have faster spall propagation characteristics than M50 and M50 NiL bearings. This behavior is observed in the spall propagation experiments performed by AFRL. The effects of initial residual compressive stress and gradient in flow curve will have secondary effects on spall propagation due to the geometry of the spall edge and the nonlinear subsurface trend in hardness for case hardened M50 NiL.

CHAPTER 1 INTRODUCTION AND MOTIVATION

Jet Engine Performance

The United States military is always in need of faster and more reliable aircraft. High-performance fighter jets such as the F-16 (Figure 1-1) require the most advanced technology in the world to be undetectable by the enemy, fly faster than sound, while at the same time be fuel efficient and protective of the pilot. The power and agility of these aircraft are of utmost important to mission success and national security. Fighter jets have to withstand the most severe conditions such as corrosive salt spray on naval aircraft carriers or the brutal heat and sand of desert environments.



Figure 1-1. USAF F-16 Fighter Jet (Picture taken by Staff Sgt. Cherie A. Thurlby)

Jet engines provide thrust for the aircraft. The main sections of a jet engine are identified here. The compressor increases the pressure of incoming air before it enters the combustor and mixes with jet fuel. The combustor ignites the high pressure air-fuel mixture and sends the exhaust to the turbine section. The flowing high-temperature and high-pressure exhaust gases forces the turbine rotors to spin and power the compressor. The overall acceleration of the airflow through the engine provides a reaction force in the form of thrust. The performance and endurance of jet engines play

a key role in the effectiveness of jet aircraft. Engine failure during a mission can lead to the loss of a multi-million dollar aircraft and compromise the safety of the pilot and success of the mission. Many research dollars are spent each year to make jet engines more reliable and powerful. One of the most critical machine components that limit reliability and power are the thrust-loaded ball bearings along the main engine shaft.

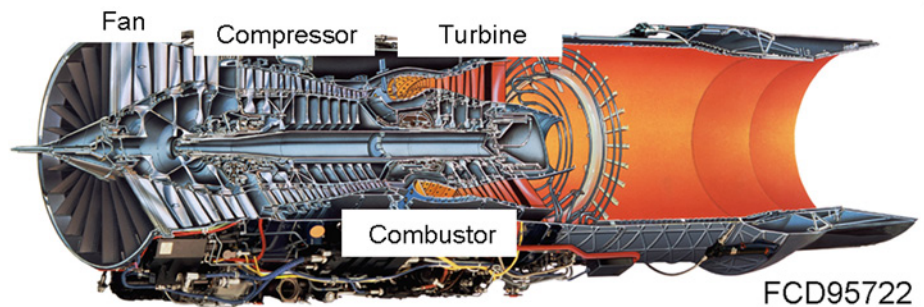


Figure 1-2. F-100 Pratt & Whitney Jet Engine. (United Technologies Company)

Bearing Design and Performance

Bearings provide rotational freedom between concentric shafts or the engine housing and are the main subject of this work. Typical thrust-loaded bearings in jet engines consist of inner and outer metal raceways that provide a path for the balls to travel and a cage that separate the balls (Figure 1-3). Bearings perform the best under pure rolling conditions and when the relative sliding between the rolling elements and raceways is minimized. This ensures that less work is lost due to friction and heat, thus making lubrication very critical to bearing performance. The locations of the ball and roller bearings along the main engine shaft of a typical twin-spool jet engine are shown schematically in Figure 1-4.

The shape and size of the bearing have a direct effect on the magnitude and distribution of the contact stresses that occur between the balls and raceways (frequently called “contact patches”). A contact patch in a ball bearing is typically in the

shape of an ellipse due to the non-conformal geometry of the ball and raceways (Figure 1-5). Calculations to determine the contact patch size based on loading and bearing geometry can be found in Boresi and Schmidt (2003) and Harris (1991).

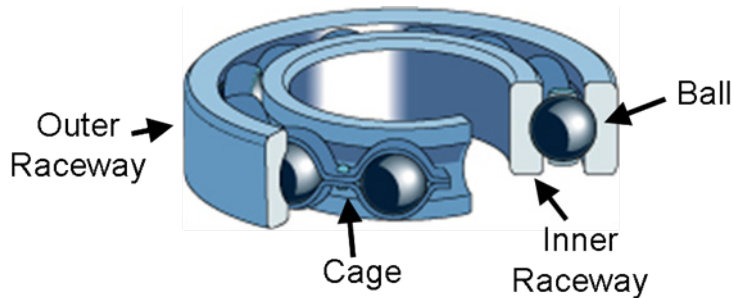


Figure 1-3. Single row deep groove SKF ball bearings.

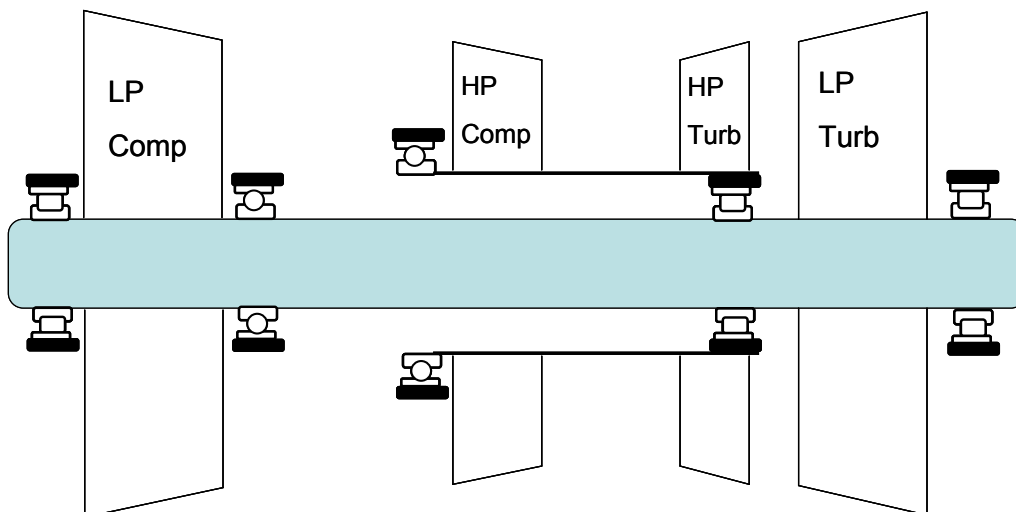


Figure 1-4. Locations of ball and roller bearings of a twin-spool jet aircraft engine.

Large contact patches generate excessive amounts of friction and heat which can reduce the speed of the bearing and decrease performance while smaller contact patches induce large stresses into the raceway which can lead to local plastic deformation. The contact stress is more severe on the inner raceway because it has a more non-conformal geometry than the outer raceway and explains why surface fatigue failures are more likely to occur on inner raceways. In either case, the engineer wants to transmit the greatest allowable thrust load through the bearing while making it last as long as possible. Longevity has been increased in some high performance bearings by

using case hardened, stainless steel raceways and ceramic balls. The stainless steel raceways and ceramic balls resist corrosion. Ceramic balls also have lower densities, exert lower centrifugal forces, have higher hardness which prevents wear, and perform better in “oil-out” conditions than steel balls.

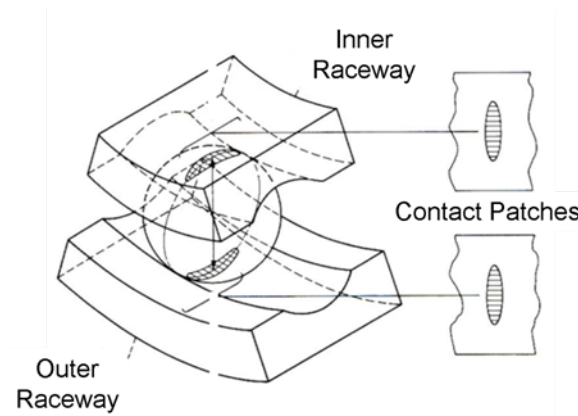


Figure 1-5. Deformation due to contact forces between ball and raceways occurs in the form of elliptical contact patches. (Hamrock, 1981).

Bearing Fatigue Failure

Regardless of these benefits, bearings cannot escape the deleterious effects caused by Foreign Object Debris (FOD), material fatigue, improper handling and installation, or excessive loading. FOD can cause scratches or dents on the surfaces of the balls or raceways which act as stress risers and lead to crack formation and crack growth with continued operation. These cracks eventually liberate surface material and create a small pit or spall (Figure 1-6.B). Spalls can also be initiated by rolling contact fatigue that occurs within the ball track of the bearing raceway. Here, local cyclic plasticity can occur around stress risers in the material microstructure such as imperfections or carbides in the bearing steel. Similarly, local cracks can form and grow at these locations with continued operation and lead to surface spalls. This

process of spall initiation is well researched in the review paper by Sadeghi et al., (2010).

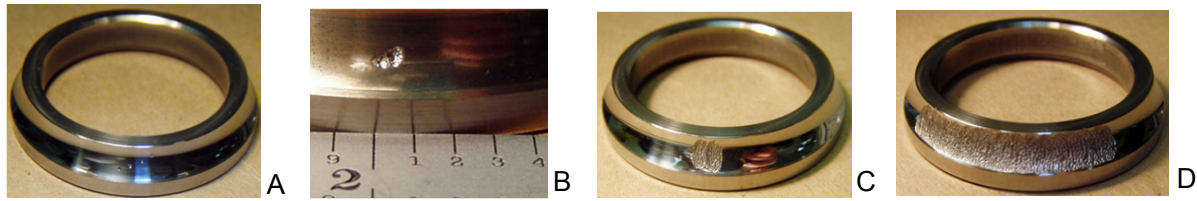


Figure 1-6. Stages of spall propagation: A.) Virgin split inner raceway (no spall). B.) Small initial spall. C.) Small initial spall widens. D.) Propagated spall

Continued engine operation cause the spalls enlarge and propagate along the surface of the raceway (Figures 1-6.C.D). The clearance created from this loss of surface material is sufficient to cause the main engine shaft to misalign and create severe vibrations, heat, noise, excessive loading, and further spall propagation.

Typically the first component to fail is the bearing cage which allows the balls to collide and disperse and leads to extreme shaft misalignment and catastrophic engine failure (Figure 1-7).

Spall propagation studies have been carried out by the Air Force Research Labs by Rosado et al. (2010) and Forster et al. (2010) where they have identified three stages of spallation. The first stage is spall initiation that is well investigated in the review paper by Sadeghi et al. (2010). The second stage is when a small spall widens and eventually allows the ball to unload and descend into the spall entirely (Figure 1-6.C). This leads to the third stage when the unloaded ball can impact the trailing edge of the spall and force the spall to propagate along the raceway's surface (Figure 1-6.D). The amount of time between initial spall formation and catastrophic engine failure is of great interest to bearing designers because this limits the amount of time a pilot can to

return to safety once an engine bearing begins to spall. Engineers would like to design bearings with slower spall propagation rates or bearings that don't spall-propagate at all.

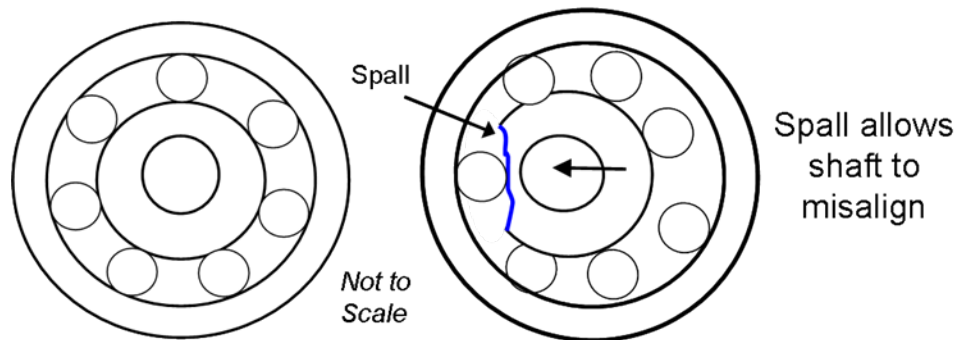


Figure 1-7. Clearance created by spall allows engine shaft to misalign.

As expected, different bearing materials will not have the same spall propagation characteristics. This was observed in Rosado et al. (2010) where scaled down versions of the bearings used in the actual aircraft engines were all spall-propagated in controlled experiments. The bearings were 208 size (40 mm) bore split inner ring raceways with 12.7 mm (0.5 in) diameter balls.

The bearings were thrust loaded in a custom rig by a hydraulic loading cylinder and attached to an external motor shaft that rotated at a constant 10,000 rpm (Figure 1-8). Band heaters maintained a constant bearing temperature of 131°C. Their study investigated 52100, M50 through-hardened, and M50 NiL case hardened bearing steels. Their material compositions are shown in Table 1-1. M50 NiL is a low carbon, high nickel steel that is case hardened.

The M50 and M50 NiL bearings are paired with ceramic silicon nitride balls whereas the 52100 bearing used 52100 steel balls. Brand new bearings and bearings that had been subjected to millions of loading cycles were both used in their study to see if initial rolling contact fatigue affected spall propagation rate.

Table 1-1. Material composition of primary alloying elements for the bearing steels in this study. (Rosado et al., 2010), (AMS-Aerospace Material Specification)

Material	Wt% Primary Alloying Elements					Reference*
	C	Cr	Ni	V	Mo	
AISI 52100	1.04	1.45	—	—	—	AMS 6440L
AISI VIM-VAR M50	0.80	4.00	0.10	1.00	4.25	AMS 6491A
VIM-VAR M50NiL	0.13	4.00	3.40	1.23	4.25	AMS 6278

*Aero Material Specification.

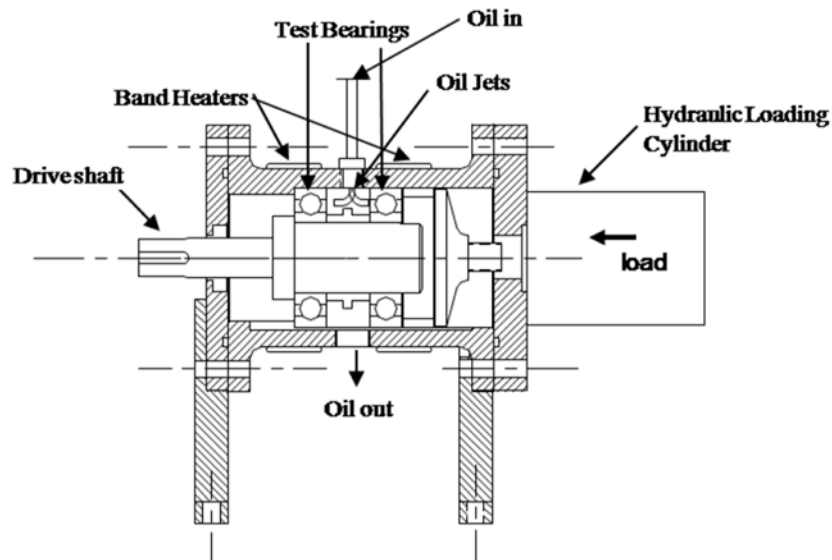


Figure 1-8. Bearing test rig for life-endurance and spall propagation bearings at AFRL. (Rosado et al., 2010).

Figure 1-9 taken from Rosado et al. (2010) shows the rate of mass loss from the raceway surface of all three types of bearings as a function of stress cycles during spall propagation. The surfaces of these new bearing raceways were indented with Rockwell C indents to act as stress risers, initiate fatigue cracks during bearing operation, and reduce the amount of time to spall initiation. The bearings were inserted into the test rig and operated at a maximum contact pressure of 2.41 GPa (as seen on the virgin raceway surface). The mass loss from the spalled bearing was detected by an oil debris monitor (ODM) and the average sizes of the spalled particles were on the order of 100 μm (Rosado et al., 2010). The 52100 bearing steel had the shortest amount of

time to spall initiation and the fastest spall propagation rate. Both the M50 and M50NiL steels showed the longest amount of time to spall initiation and a slightly slower spall propagation rate. Note these spall propagation experiments are conducted on the order of tens of millions of stress cycles.

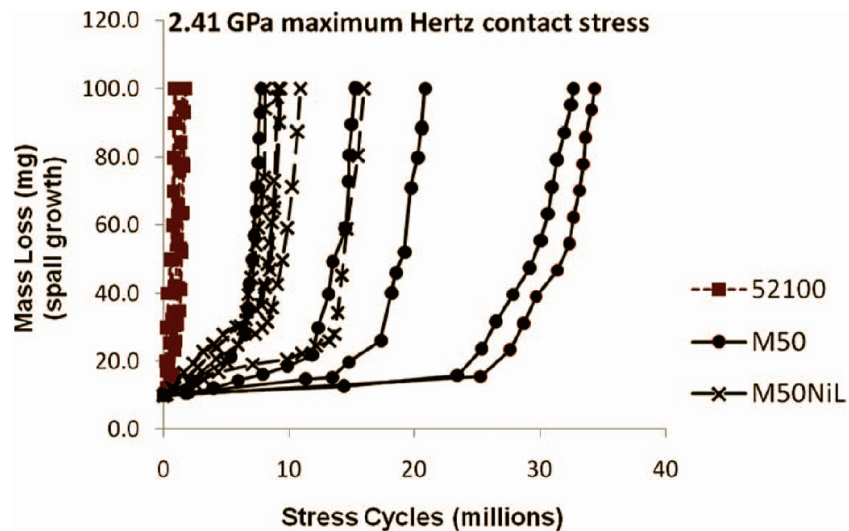


Figure 1-9. Spall propagation characteristics for 52100, M50, and M50 NiL. Spalls initiated by Rockwell C indents on virgin raceways at maximum contact pressure of 2.41 GPa. (Rosado et al., 2010).

A similar experiment was done on new indented virgin bearings but with a lower contact pressure (2.10 GPa virgin raceway) and as expected the amount of time to spall propagation was considerably longer due to the lower contact stresses, but the trends were similar (Figure 1-10). Note the longest propagation experiments required as much as 500 million stress cycles at this lower contact pressure. In both cases M50 NiL and M50 steels significantly outperform 52100 whereas the differences between M50 and M50 NiL are not so obvious. Similar tests were done on life-endurance tested bearings that were run continuously at 10,000 rpm for 5 months prior to natural spall initiation or test suspension. The suspended bearings were indented with Rockwell C indents to initiate a spall and propagated at 2.41 GPa maximum contact pressure. The

consequent mass loss from the surface as a function of stress cycles is shown in Figure 1-11.

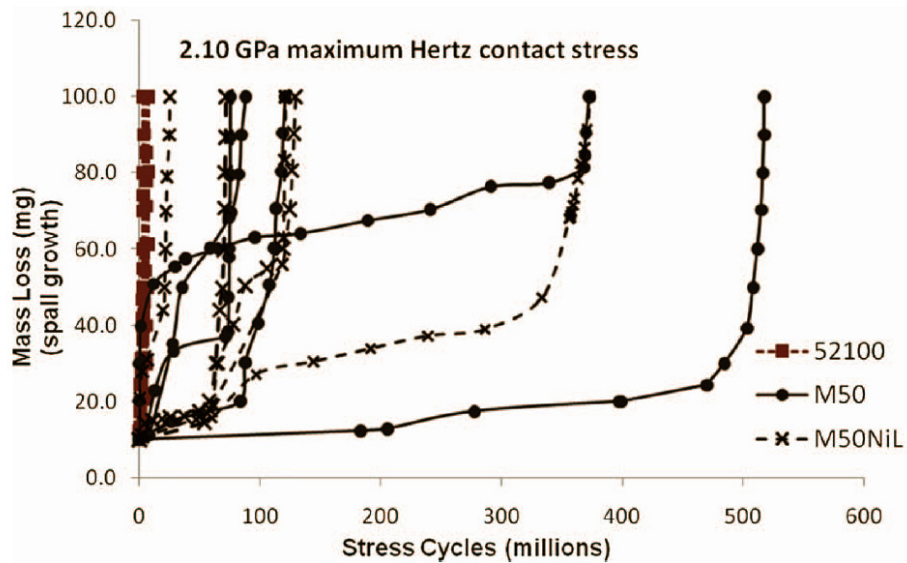


Figure 1-10. Spall propagation trends for new (indented) bearings at 2.10 GPa maximum contact pressure. (Rosado et al., 2010)

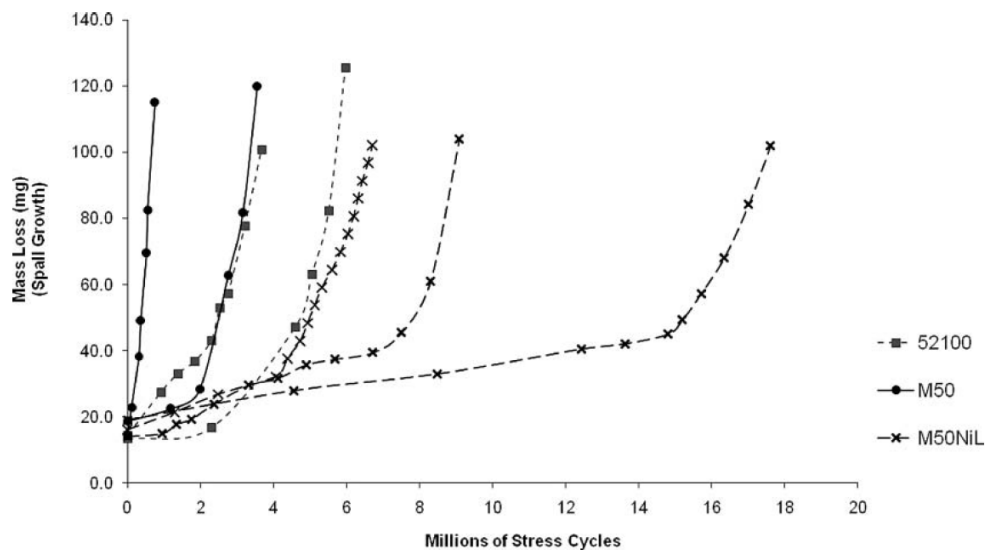


Figure 1-11. Spall propagation trends for 52100, M50, and M50 NiL at 2.41 GPa maximum contact pressure for previously life-endurance tested bearings. (Rosado et al., 2010).

Note due to the cost and amount of time required to perform these tests there are only 7 bearings available to compare in this graph. But it can be inferred here that M50

NiL out performed the other bearing materials in this study as seen by its longer time to spall growth and slower spall propagation rate. Interestingly, the spall propagation rate for M50 increased for the life-endurance tested bearings. This suggests that spalls propagate faster and sooner for M50 bearings that have been in service for a considerable time.

The fracture toughness of the case hardened layer of M50 NiL is lower than its core region and M50 through-hardened steel, but close to that of 52100 (Table 1-2). However, the spall propagation characteristics of M50 NiL are similar to M50 and superior to 52100 when compared for the virgin indented bearings.

Table 1-2. Mode I fracture toughness of bearing steels in this study. (Rosado et al., 2010).

Material	K_{Ic} (MPa \sqrt{m})	Reference
Hardened AISI 52100	~ 17.5	Beswick (1989)
AISI M50	23.0	Averbach, et al. (1985)
M50NiL case	16.0	Averbach, et al. (1985)
M50NiL core	50.0	Averbach, et al. (1985)

This may be a result of the initial residual compressive stresses that exist within the case hardened layer of M50 NiL (and not in M50 or 52100) which retard crack formation and growth and leads to slower spall propagation trends. The initial residual stresses as a function of depth for these steels are shown in Figure 1-12 and were obtained by X-Ray Diffraction techniques described in more detail in Forster et al. (2010). Note the large residual compressive stresses at the surface are due to the final finishing of the bearing prior to installation and operation, but decrease to zero below a depth of only 10 μ m. The actual dynamics of the interactions between a ball and raceway spall are very complicated, but it is clear that severe damage is occurring

within the spall edge due to these interactions. As an illustration, for a clockwise-rotating inner raceway, a ball will unload as it departs the leading spall edge and then impacts the trailing edge (Figure 1-13A). In these experiments, cracks were observed to occur on the trailing spall edge (Figure 1-13B) and not on the leading edge. It was previously unknown how or why these cracks are forming, but it is well understood that these cracks grow and liberate material with continued ball impacts and bearing operation.

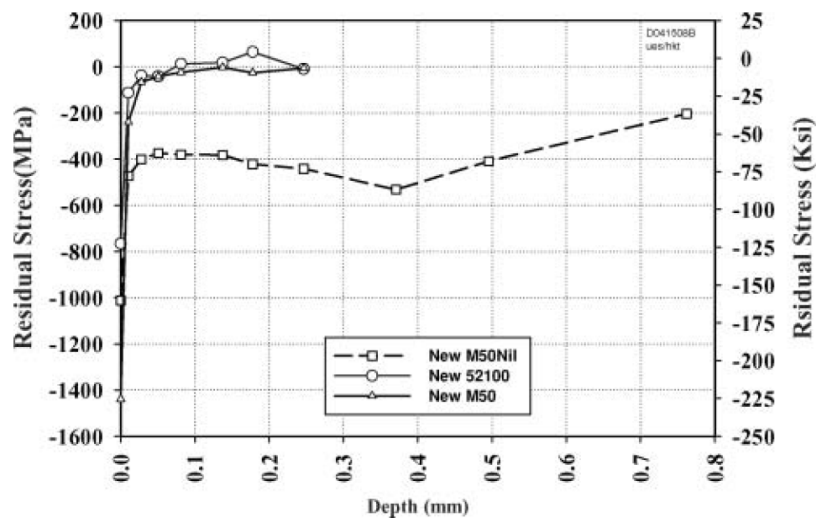


Figure 1-12. Initial residual stress profiles obtained by X-Ray Diffraction (XRD) in hoop direction of the bearings in this study prior to installation and operation (Forster et al., 2010).

The work presented in Chapters 3 and 7 will provide an explanation for this crack formation within the spall edge as well as the influence of material plastic response, initial compressive residual stress, ball mass, and gradient in flow curve for case hardened bearing steels. Since the interactions between the ball and spall edge are driving spall growth and propagation, it is important for an engineer to quantify the amount of damage that is induced when a ball passes over or impacts a spall edge. In the work presented here, both static and dynamic analyses will be used to estimate the

amount of damage imparted to an impacted spall edge during the spall propagation experiments performed by Rosado et al. (2010) and Forster et al. (2010).

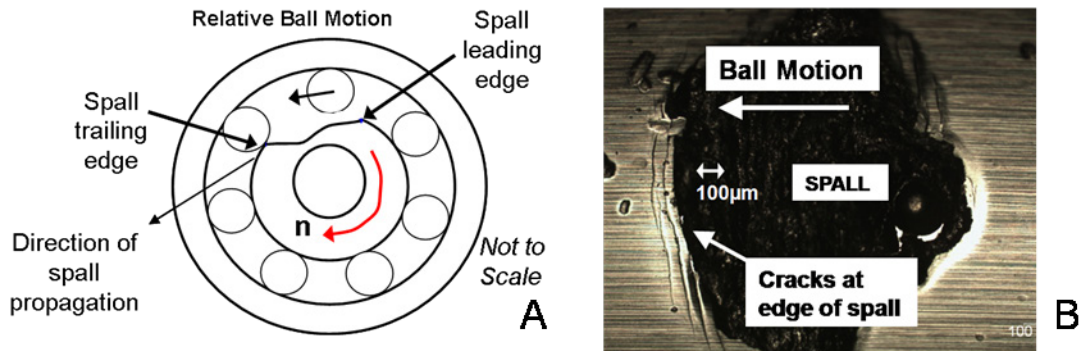


Figure 1-13. (A) Schematic showing relative ball motion between leading and trailing spall edge for clockwise-rotating inner raceway. (B) Cracks form on the trailing spall edge that is subjected to ball impacts. This spall edge is deteriorating with continued bearing operation as these cracks grow and liberate surface material.

Past research that identifies the governing mechanisms of spall propagation is scarce because previous bearing life methodologies define useful bearing life as the formation of an initial spall and not a progressed spall. Probabilistic bearing life prediction models that are based on the equations developed by Lundberg and Palmgren (1947) are often used to estimate the life of a spalled bearing but neglect important effects such as plasticity. A comprehensive review of these bearing life methodologies is covered by Zaretsky et al. (1996) and Sadeghi et al. (2010).

Kotzalas and Harris (2001) studied spall propagation on 52100 steel balls that were driven by M50 steel V-Ring raceways and extended the bearing life prediction methods of Ioannides and Harris (1985) to predict the remaining useful life of spalled bearings. Xu and Sadeghi (1996) implemented damage accumulation laws within representative volume elements undergoing rolling contact fatigue (RCF) to model the transformation of a dent into a progressed spall. The spall propagation experiments on

tapered roller bearings by Hoeprich (1992) highlighted the randomness inherent to spall propagation and its unknown governing mechanisms. A further investigation is needed to better understand these governing mechanisms and will be presented in this dissertation.

An outline of the following chapters and objectives are presented here:

- The governing mechanisms of spall propagation will be investigated here through a series of static and dynamic analyses of contact interactions between ball and spall edge. The bearing geometry and operating conditions of (Rosado et al.) will be simulated in finite element models to determine the critical stresses and strains that develop from these interactions in Chapters 2, 3, and 7.
- The plastic response of the case hardened region is unknown for most bearing steels. The material properties of graded materials such as case hardened P675 and M50NiL steels will be determined from a new indentation method presented in Chapters 5 and 6, which relies on the concept of a material-dependent representative plastic strain and indentation forward analysis presented in Chapter 4.
- A new reverse analysis that determines the flow curve of a material based on its measured increase in hardness within a zone of plastic deformation is presented in Chapter 6 and applied to finding the material properties of graded materials when the core properties are unknown initially.
- The material properties of plastically graded M50 NiL are used in a similar dynamic spall model of Chapter 3 to determine if its gradation in plastic response and initial residual stress affect the amount of damage induced by a ball impact on a spall edge in Chapter 7. The effects of surface hardness and ball mass will also be considered.

CHAPTER 2 STATIC ANALYSIS OF INITIAL SPALL WIDENING

Motivation and Validation of Finite Element Model

As a first attempt to better understand the governing mechanisms of spall propagation, a static analysis will investigate stage 2 initial spall widening (Figure 1-5.B and 1-5.C) since stage 1 spall initiation is well described by Sadeghi et al. (2010). The magnitude and distribution of the stresses within a spall edge when a ball passes over a spall are unknown but will be determined here through finite element modeling. Spall size, ball load, and the location of a ball over a spall are expected to affect the magnitude and distribution of the stresses within the spall edge. It is also unknown initially whether linear elastic deformation takes place or if the spall edge plastically deforms during operation.

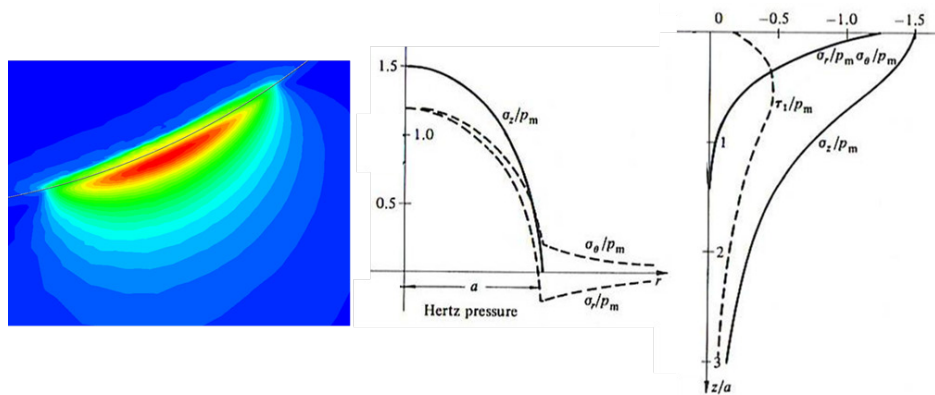


Figure 2-1. Hertzian contact solutions are verified by FE model for bearing geometry used in Rosado et al. (2010) and Hertzian contact equations taken from Johnson (1987).

The calculations needed to find these stresses associated with ball and spall interactions are extremely difficult to do by hand. Finite element analysis provides a means to estimate the stresses within the spall edge by simulating the ball and spall contact interaction for realistic boundary conditions. The commercial FEA software package ABAQUS is used here because of its ability to model three dimensional

geometries and include plasticity effects. This analysis does not attempt to optimize a specific numerical solver or create its own finite element code, but will rather apply the tools that already exist to solve a complex problem.

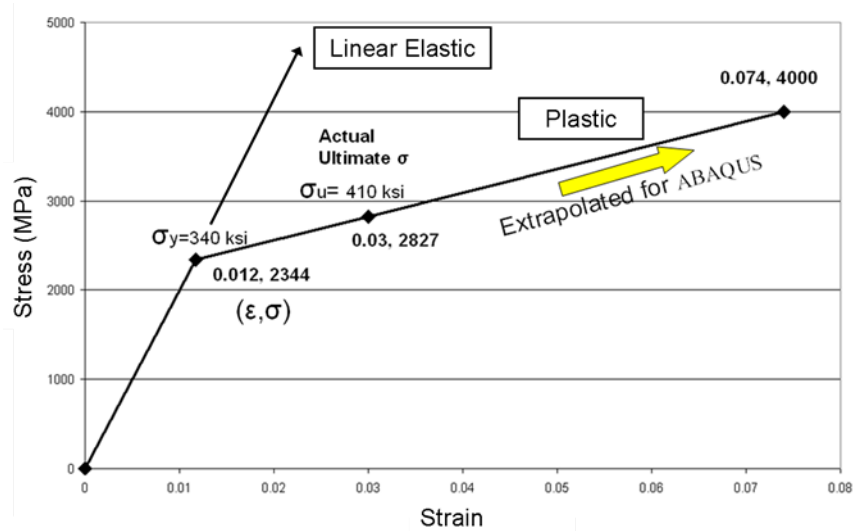


Figure 2-2. Both pure-linear elastic and linear-plastic properties are used in this analysis for comparison.

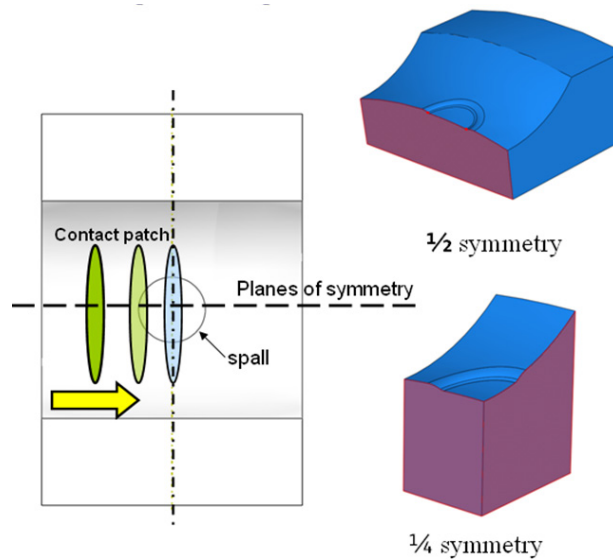


Figure 2-3. Symmetry exists as ball goes over circular spall

The contact patch and subsurface von Mises stresses are calculated by the model of the 208 size bearing used in Rosado et al. (2010) and compared to analytical Hertzian contact equations taken from Boresi and Harris (2003) for a virgin (no spall)

raceway to ensure the model uses the correct boundary and loading conditions, finite element mesh density, and bearing geometry. The ball is analytically rigid and does not require a mesh. A load of 1630N is applied at the center of the ball which yields a maximum contact pressure of 2.65 GPa (385 ksi). The FE model results provide a good match to the stresses calculated by Hertzian contact solutions (Figure 2-1).

Static Analysis of Ball over Circular Spall

The same ball load will be simulated again but now the ball will contact a circular spall instead of a virgin raceway. Material properties taken from Carpenter (2009) for M50 steel are shown in Figure 2-2.

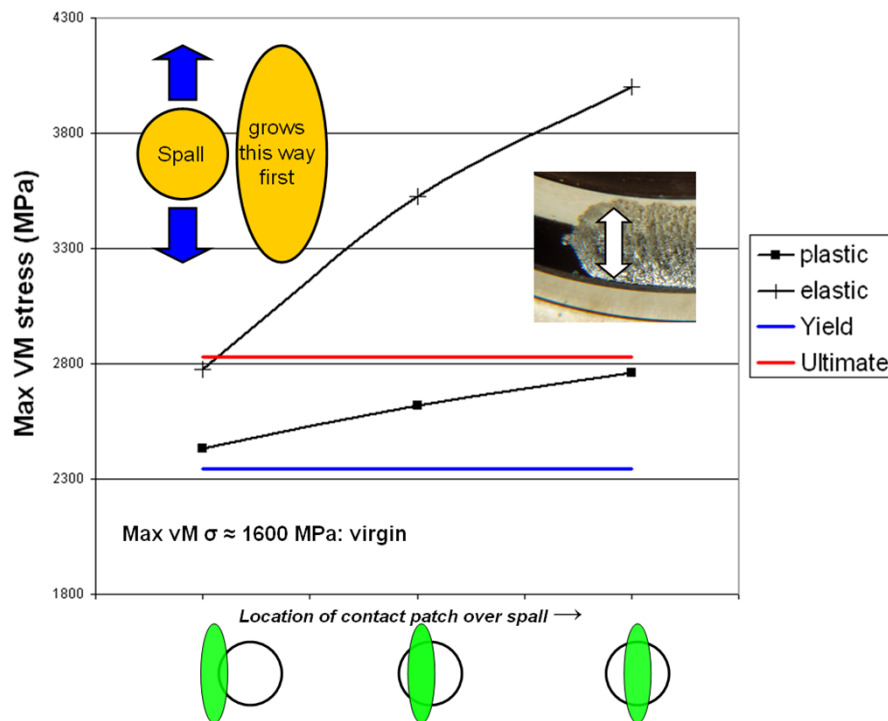


Figure 2-4. Maximum von Mises stresses within spall edge increase as ball approaches center of spall. Linear elastic material properties severely over-predict von Mises stresses. Spall widens before it propagates.

The plastic response is extrapolated past the ultimate strength incase this stress is exceeded within the spall edge and will give an idea of the extent the ultimate strength is exceeded. In a separate test case, purely linear-elastic material properties will be

assigned to the spall's edge to see by how much they over-predict the von Mises stresses. Symmetry is taken into account in the model geometry in all cases as seen in Figure 2-3. The maximum von Mises stresses within the edge of the spall are calculated as a ball goes over the spall at three locations in Figure 2-4.

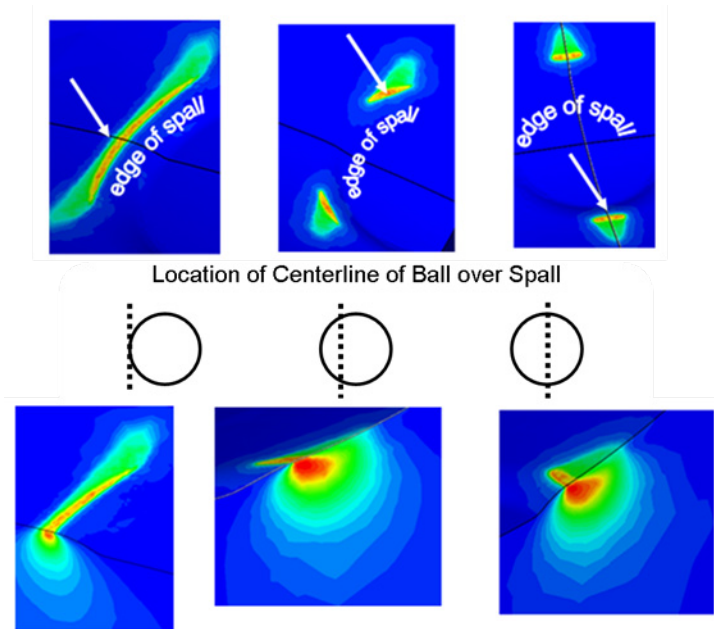


Figure 2-5. Cross-sections of von Mises stresses within spall edge as ball approaches spall center.

Linear elastic material properties give unrealistic results as the stresses are severely over-predicted, whereas when the plastic response is defined, results show that the stresses are high enough to yield the spall edge. Intuitively, the stresses increase as the ball approaches the spall center as there is less material available to support the ball. Subsurface contours of these stresses are shown in Figure 2-5. The stresses are highest when the ball is over the center of a circular spall, thus more damage is induced at this location and causes the spall to widen before it propagates as seen in experiments. Since the stresses are the highest when ball is directly over the center of a circular spall, this will be treated as the worst case scenario in the next two

test cases. The load on the ball increases the von Mises stresses within the edge of the spall as seen in Figure 2-6.

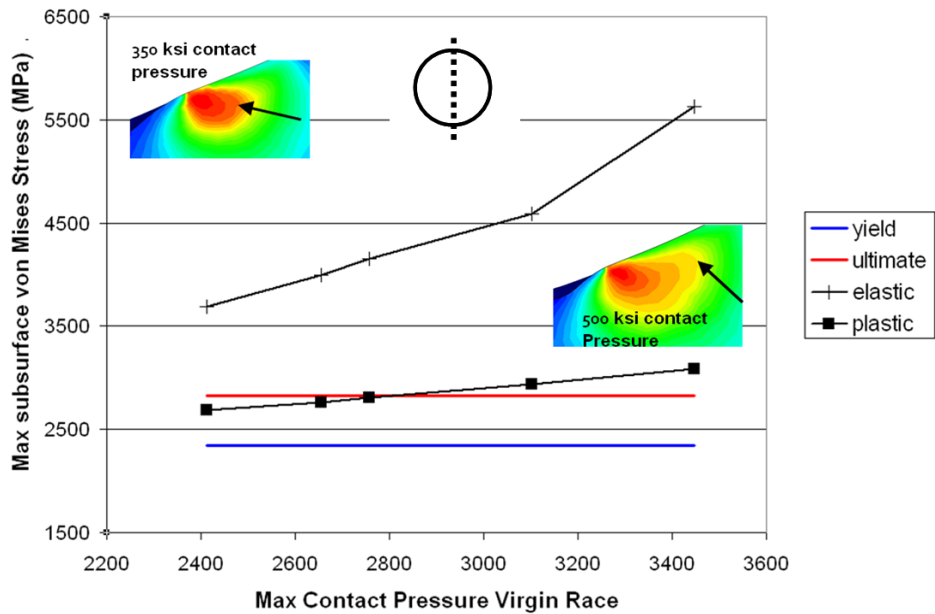


Figure 2-6. Maximum subsurface von Mises stresses increase as load on ball increases. Load on ball determined from maximum contact pressure exerted on virgin raceway. Linear elastic material properties severely over-predict von Mises stresses.

Once again purely linear elastic material properties report unrealistic von Mises stresses. When the material's plastic response is defined, the model predicts the ultimate strength is exceeded when the maximum contact pressure as seen on the virgin race is greater than 2.9 GPa. This supports the experimental evidence that increasing the ball load increases the damage within the spall edge and thus leads to faster propagation rates. The zone of plastically deformed material also increases with increasing ball load as indicated by the stress contour identified by the black arrow in Figure 6-2.

The reported von Mises stresses that exceeded the material's ultimate strength are possible because the plastic response was extrapolated past the ultimate strength

in the model. In reality, the strength of most materials is increased when subjected to high strain rates which are possible in the small region of a spall edge along with the high velocity of the moving balls.

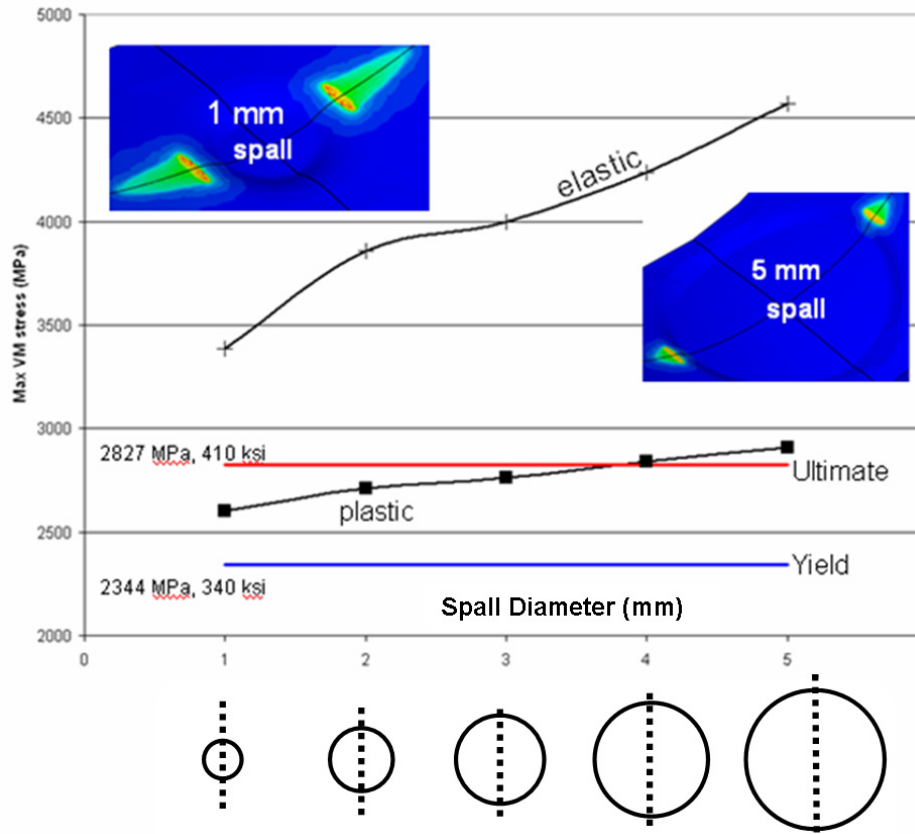


Figure 2-7. Maximum subsurface von Mises stresses within spall edge increase as spall diameter increases. Elastic material properties over-predict von Mises stresses.

As the spall widens there is less material to support the loaded ball which would lead to higher stresses within the spall edge. This was modeled and the results are shown in Figure 2-7. Linear elastic material properties give unrealistic stress results within the edge of the spall. When plasticity is defined, the spall edge is allowed to plastically deform and the ultimate strength is exceeded for a 4 mm diameter circular spall for this material and bearing geometry. Thus more damage is induced in the form of plastic deformation in larger spalls because there is less material to support the ball.

This agrees with experimental data which shows the spall propagation rate increases as the spall becomes larger.

Summary

The results of this analysis were rather intuitive, but this was a first effort to model the damage induced by ball and spall interactions. These results have been published in Arakere et al. (2010) and a few key points are summarized here:

- Linear elastic material properties severely over predict the stress state within a spall edge. The plastic responses of these bearing steels are needed to better understand the damage suffered by a spall edge during bearing operation.
- As expected, higher ball loads and larger spall sizes increased the extent of plastic deformation as evidenced by the increased von Mises stresses within the spall edge. Larger spalls have less material to support the ball and cause higher stresses to develop in the contacted region. Increasing the ball load increased the stresses for a given spall size.
- This analysis also supports what is seen in experiments where spalls tend to widen before they propagate along a raceway. The highest extent of yielding and damage was seen when the ball is over the center of the spall where there is the least amount of material to support it.
- As the spall widens, the ball is allowed to descend into the spall, impact the spall's trailing edge, and further drive spall propagation. The next analysis in Chapter 3 will investigate the spall propagation stage and the extent of damage that is induced by a ball impact on a spall edge.

CHAPTER 3
DYNAMIC ANALYSIS OF BALL IMPACT WITH SPALL EDGE

Ball Impact with Spall Edge Drives Propagation

With continued bearing operation, the spall widens to such an extent to allow the ball to descend into the spall and impact the trailing edge. For a clockwise-spinning inner raceway and a relatively fixed outer raceway (Figure 3-1), the relative motion of the balls and inner raceway cause the balls to impact the trailing edge of the spall as it reestablishes contact between the inner and outer raceways. As a result, spall propagation is in the same direction as the ball motion relative to the spall edge.

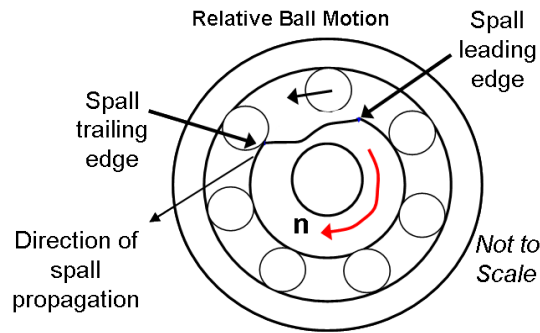


Figure 3-1. Relative ball motion causes ball impact with trailing spall edge

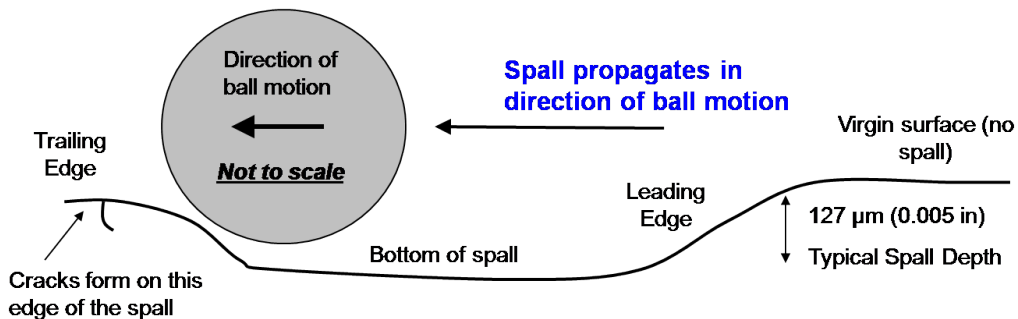


Figure 3-2. Cracks form on spall trailing edge. Typical spall depth is 127μm.

The spall's trailing edge is defined as the edge that deteriorates with bearing operation, whereas the spall's leading edge is a portion of the initial spall and remains throughout propagation (Figure 3-1). The numerous impacts that occur between the

ball and trailing spall edge are thought to be the main driving forces of spall propagation. Both the leading and trailing edges experience the pinch caused by the ball's contact with the inner and outer raceways; however, only the trailing edge is subjected to ball impacts and deterioration.

Also, significant cracks form only on the spall's trailing edge (Figures 3-2 and 3-3) as the spall is propagating. This is another indication that more damage is occurring on the impacted edge in the form of cracks and not on the leading edge. Continuous ball impacts encourage these cracks to grow and cause fragments of material to liberate from the raceway's surface. The fragments collected by the Oil Debris Monitor (ODM) in Rosado et al. (2010) were typically the same size as the edge of the spall (100 μm). The mechanisms that cause these cracks to form were previously unknown, but an explanation will be given later in this chapter and in Chapter 7.

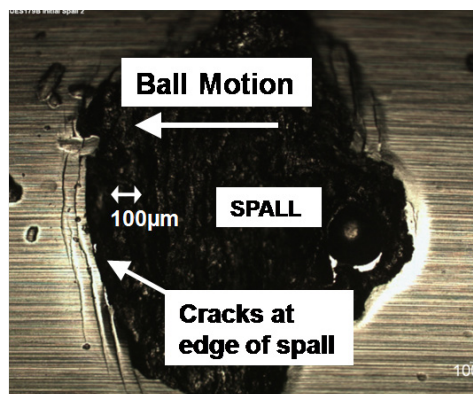


Figure 3-3. Cracks appear on the spall's trailing edge

Finite Element Model

The dynamic analysis presented here is unique because it uses finite element models that include the effects of plasticity to calculate the critical stresses and strains that develop within a spall edge during and after successive ball impacts. The modeling results are supported by the locations of cracks along a spall edge. This information will

support a plausible scenario of why fatigue spalls propagate. This new finite element model is similar to the one from the static analysis except now the spall is sufficiently large enough to allow the ball to completely unload and impact the trailing edge. Actual bearing dynamics are very complex with interactions between the balls, cage, and raceways, but are not considered here in interest of time and simplicity. Only a segment of the inner raceway is modeled and the ball is given a mass and velocity and allowed to impact the spall edge (Figures 3-4 and 3-6).

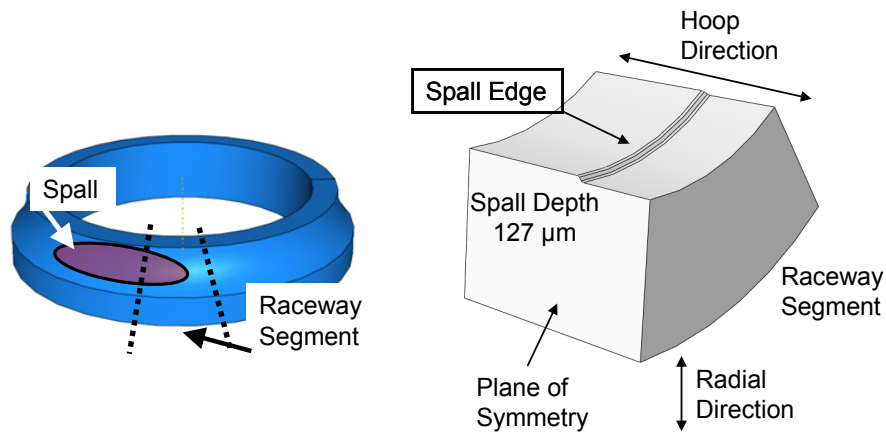


Figure 3-4. Only segment of inner raceway is modeled.

To capture the geometry of the spall edge, profilometer tracings were taken on propagated spall edges from case hardened Pyrowear 675 (P675) and M50 through hardened bearing steels (Figure 3-5.A). An average spall slope of 45 degrees was measured from the four profiles and used in the finite element model geometry (Figure 3-5.B). This edge geometry is consistent during spall propagation regardless of spall length (Figure 3-5.B).

The finite element model will simulate three successive rigid ball impacts on the same spall edge at a ball velocity of 15.24 m/s (50 ft/s) (Figure 3-6). The ball velocity is determined from the kinematics of the known rotational speeds of the cage and

raceways of the 40 mm bore bearing used in Rosado et al. (2010). Three impacts were chosen because there was no significant difference in the stresses and strains within the spall edge after the second and third impacts. This is due to the fact that isotropic hardening was used here and the cyclic hardening laws for these steels are unknown.

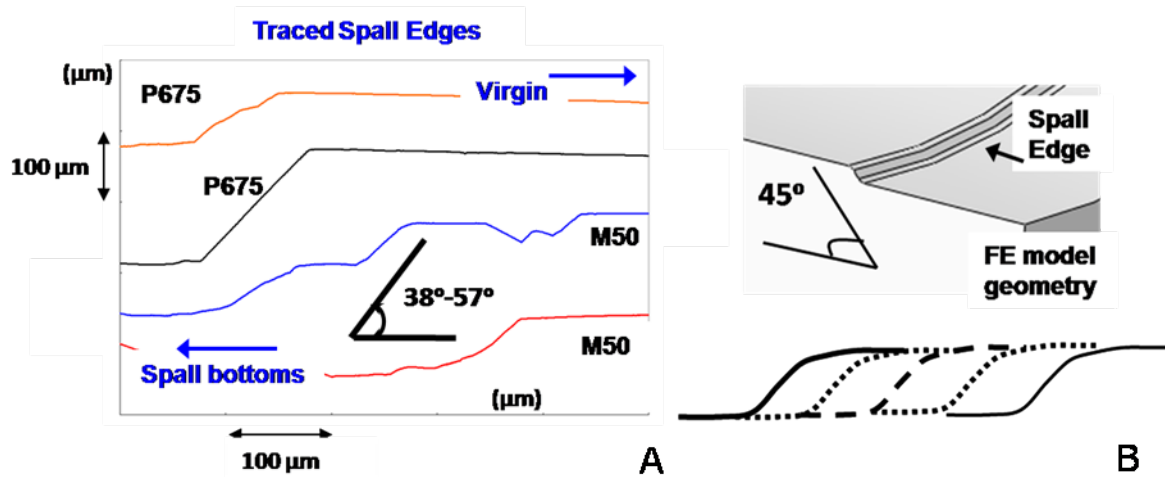


Figure 3-5. (A) Profilometer tracings of various spall edges. (B) Spall edge slope is consistent throughout spall propagation.

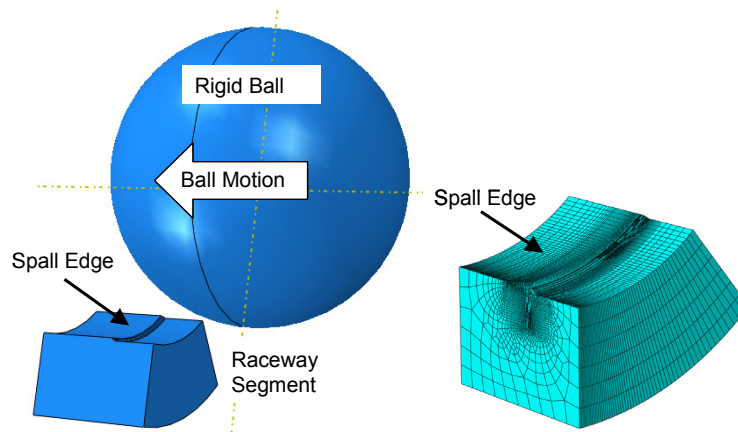


Figure 3-6. Finite element model geometry and mesh.

All three balls have the density of ceramic silicon nitride (3.2 g/cm^3). The ball is not allowed to spin and can only translate within the plane of symmetry. In-house compression tests were performed on M50 bearing steel specimens to obtain its flow curve up to 0.013 plastic strain and compared well with data from Carpenter (2009) (Figure 3-7). The material is assumed to behave in a perfectly plastic manner after this

strain is reached as observed by the decreasing strain hardening trend obtained from the compression test. Very hard materials such as bearing steels do not have a large capacity to strain harden like copper or 303 stainless steel (Lai and Lim, 1991), so a perfectly plastic assumption is valid here. Also the cyclic hardening properties are unknown for most bearing steels thus only the monotonic stress strain curve will be utilized here.

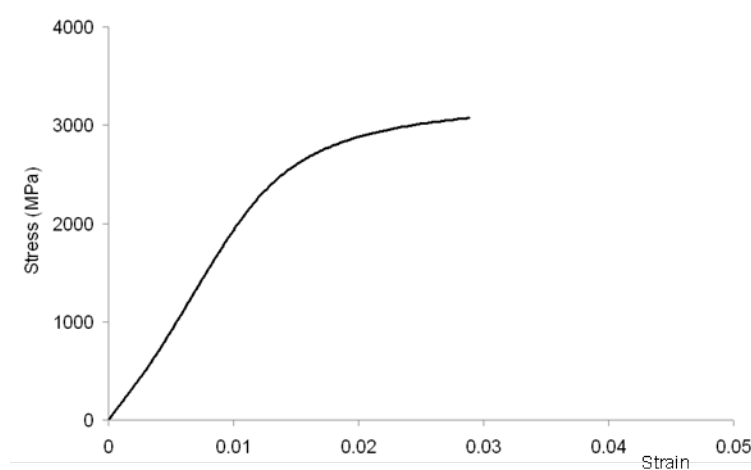


Figure 3-7. Flow curve of M50 steel from in-house compression test

A very fine linear hexahedral mesh is designed around the spall's edge because the most critical stresses and strains are forming in this small region (Figure 3-6). The explicit solver within ABAQUS v6.8-2 was used since this is a transient analysis and has time-dependent properties (the velocity of the ball). The von Mises (J2) failure criterion, associative flow rule, and isotropic hardening are appropriate for bearing steels and implemented here.

Finite Element Model Results

All plots of the finite element model results are close-up images of a spall edge's cross-section. The radial stresses during impact were calculated and mostly compressive as expected (Figure 3-8). The maximum contact pressure between the

ball and spall edge can reach 8 GPa which is sufficient to cause subsurface yielding. Classical Hertzian contact solutions do not apply here since the spall edge is very sharp and is undergoing considerable deformation during impact.

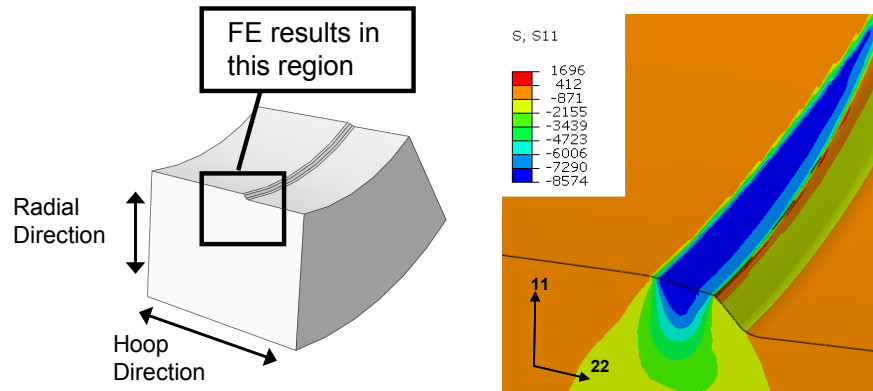


Figure 3-8. Radial stresses (11 direction) are highly compressive during ball impact.

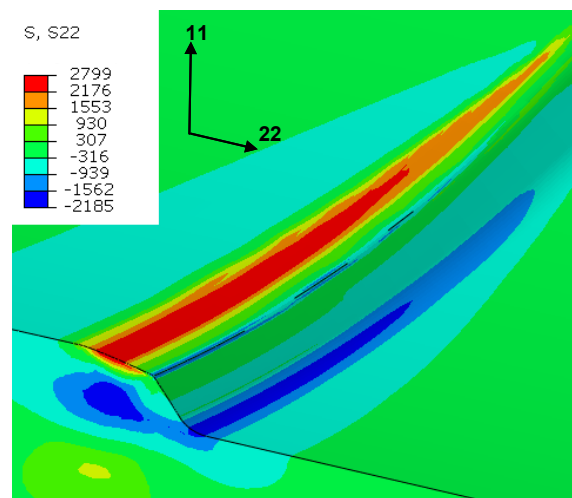


Figure 3-9. Residual hoop (22 direction) stresses of cross section of impacted spall edge. Note location of tensile residual hoop stress agrees with locations of cracks along spall edge in Figure 3-3.

Of greater interest are the locations and distributions of residual tensile stresses around the edge of the spall. It is well understood that residual tensile stresses are detrimental to the fatigue strength of a material because they encourage fatigue crack initiation and growth. The finite element model calculates residual tensile hoop stresses to occur on the surface of the spall's edge after successive ball impacts (Figure 3-9). This is significant because this location of residual tensile stress agrees with the

locations of cracks around the spall's edge (Figure 3-3) in the bearings from Rosado et al. (2010).

The location of residual tensile maximum principal and hydrostatic stress also agrees with where cracks appear in spalled bearings (Figures 3-10A and 3-10B). Howell et al. (2010) studied rolling contact over a surface indent and showed that cracks are likely to initiate in regions of tensile hydrostatic stress. The finite element results in Figures 3-9 and 3-10 show compressive residual stresses located just below the spall's edge. Compressive residual stresses below the spall's edge retard crack growth and consequently keep material loss localized to the immediate surface as this was observed in the propagation experiments of Rosado et al. (2010).

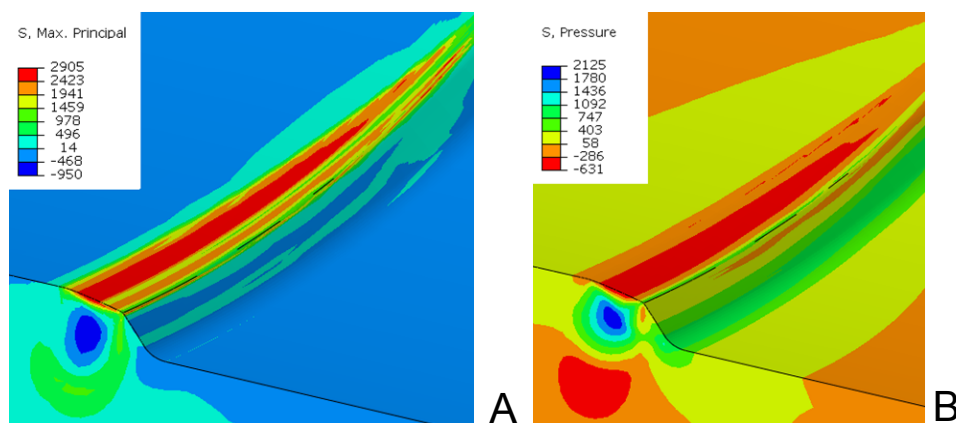


Figure 3-10. (A) Residual maximum principal stress and (B) residual hydrostatic pressure after successive ball impacts. Note tensile hydrostatic stresses occur in same location as cracks in Figure 3-3. (Tensile hydrostatic stress is negative)

The strain-life approaches summarized in Suresh (2004), such as Coffin-Manson, have shown that fatigue cracks are likely to initiate sooner in regions of high plastic strain over many load cycles. A detailed quantitative fatigue life analysis cannot be made here since the cyclic strain-life data for bearing steels is scarce, the plastic strains calculated by the FE model are for a spall that only suffered three impacts, and the

cyclic plastic strain amplitudes from the FE model are highly dependent on its cyclic strain hardening law which is also limited for bearing steels. However, as a qualitative investigation it is worth comparing the distribution of plastic strain within the spall edge with the location of cracks in the actual bearings to determine if cracks form in the most damaged region as predicted by the FE model.

The distribution of maximum principal plastic strain is shown in Figure 3-11. Cracks are likely to follow this path of highly damaged material and aided by the tensile and compressive residual stresses within the spall. The distribution of maximum principal plastic strain is also similar to the profilometer tracings of the spall edges (Figure 3-5). After a fragment of material is liberated from a spall edge, the new spall edge profile left behind is a close match to the profilometer tracings and the distribution of maximum principal plastic strain. This process repeats itself and explains why the spall edge profile does not vary throughout spall propagation.

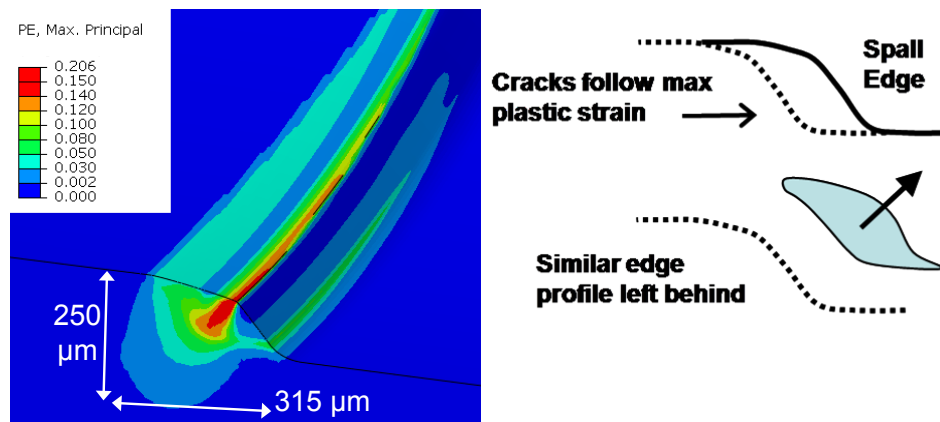


Figure 3-11. Plastic zone size and maximum principal plastic strain contour at spall edge cross section after successive ball impacts. Cracks likely to follow path of most heavily damaged material and leave behind similar spall edge.

Spall edge geometry is expected to influence the calculation of stresses and strains in the finite element model; however it is shown here that similar residual stress

gradients will develop regardless of spall edge sharpness (Figure 3-12). A sharp spall edge is considered to have a slope of approximately 45 degrees and close to what was measured by the profilometer tracings of Figure 3-5. As a test case, a blunt spall edge will have a lower slope of approximately 30 degrees.

These two degrees of spall sharpness were modeled with the same ball velocity and material properties as before. Stress contours of the residual hoop stresses within the spall's edge are shown along in Figure 3-12.

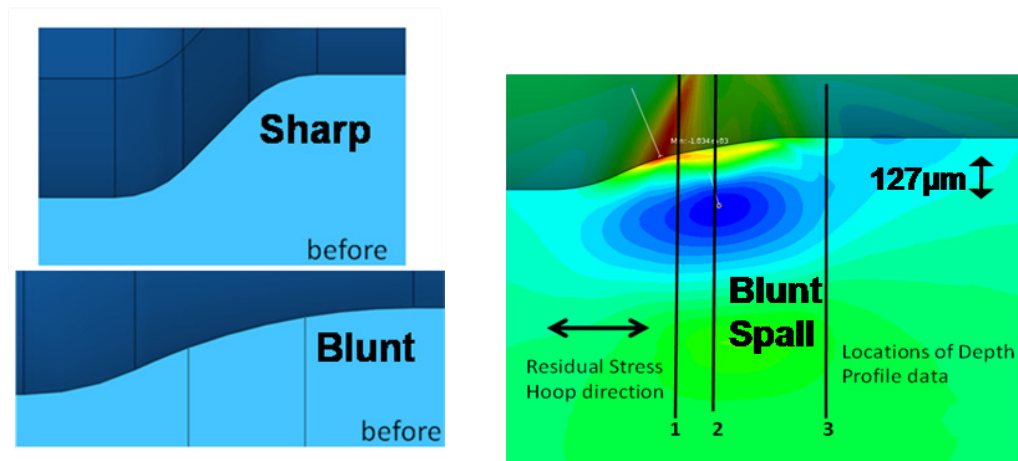


Figure 3-12. Residual hoop stress profiles for blunt spall are similar to sharp spall.

As expected, the stresses around a blunt spall are not as severe as the sharper spall edge, but the fact that the stress gradients are similar helps show the dependency of spall sharpness in the finite element results. In both cases, the location of residual tensile hoop stresses coincided with the location of cracks in the actual bearing spall edge.

Summary

This analysis is a first attempt to capture the critical stresses and strains that develop in a propagated spall edge during and after successive ball impacts. The

results of this analysis have been published in Branch et al. (2010) and the key points are outlined here:

- It is well understood that residual tensile stresses decrease the fatigue life of a material and correspond to regions of crack initiation Sadeghi et al. (2010). The finite element model determines residual hoop, radial, and hydrostatic tensile stresses to occur within an impacted spall edge at the same locations where cracks are observed in the actual bearings.
- The residual compressive stresses below the trailing edge of the spall retard crack growth and keep material loss localized to the immediate surface as seen in actual bearing surface failures.
- The distribution of maximum principal plastic strain within the spall edge provides a likely path of crack growth which leads to the liberation of material fragments during spall propagation. This is supported by observations that the spall edge shape is consistent throughout propagation and closely matches the distribution of maximum principal plastic strain that is calculated by the model. Qualitative strain-life methodologies predict cracks to initiate in regions of high plastic strain, and cracks appear on spall edges where the finite element model predicts large plastic strain.
- This analysis will be repeated for case hardened M50 NiL, but the plastic response of the plastically-graded, case hardened layer is unknown initially. A new indentation method presented in Chapters 5 and 6 will determine the plastic response of graded materials and will be based on the concept of representative plastic strain and indentation of nongraded materials discussed in more detail in Chapter 4.

CHAPTER 4 INDENTATION OF NON-GRADED MATERIALS

Relationship between Hardness and Yield Strength

The plastic response of case hardened bearings steels are needed to better understand spall propagation that occurs within their case layers. The method of using indentation hardness measurements and finite element modeling to determine the plastic response of graded materials such as case-hardened bearing steels must be validated for non-graded materials first. Parameters such as the representative plastic strain induced by a Vickers indent must be clarified for simple materials before applying them to graded materials.

Indentation hardness is often used to estimate the yield strength of a material. Pavlina and Van Tyne (2008) have shown an approximately linear relationship between Vickers hardness (H_v , a.k.a. Diamond Pyramid Hardness) and yield strength (σ_Y) for over 150 steels (Figure 4-1). Note in these graphs the units of Vickers hardness are

$H_v = \frac{\text{kgf}}{\text{mm}^2}$ whereas the units for yield strength are $\text{MPa} = \frac{\text{N}}{\text{mm}^2} = \frac{\text{kgf}}{\text{mm}^2} \frac{9.8\text{N}}{\text{kgf}}$, thus

Vickers hardness must be multiplied by 9.8 to convert to mega-Pascal units.

Indentation hardness is approximately three times a material's yield strength when they are both in the same units (Figure 4-1) and this was also predicted by Tabor (1970).

Vickers indentation induces a zone of plastically deformed material below the indent (Figure 4-2) with plastic strains highest at the tip and decrease to zero at the elastic-plastic boundary. For the indentation of a perfectly-plastic material, the stress at every point within the plastic zone is equal to its yield strength because its flow stress (yield strength) is constant for any given amount of plastic strain. The average contact

pressure (Vickers hardness) needed to plastically deform the material is typically three times the material's yield strength as predicted by Tabor (1970). This ratio is called the constraint factor (C) where for most materials:

$$C = \frac{H}{\sigma_Y} \approx 3 \quad (4.1)$$

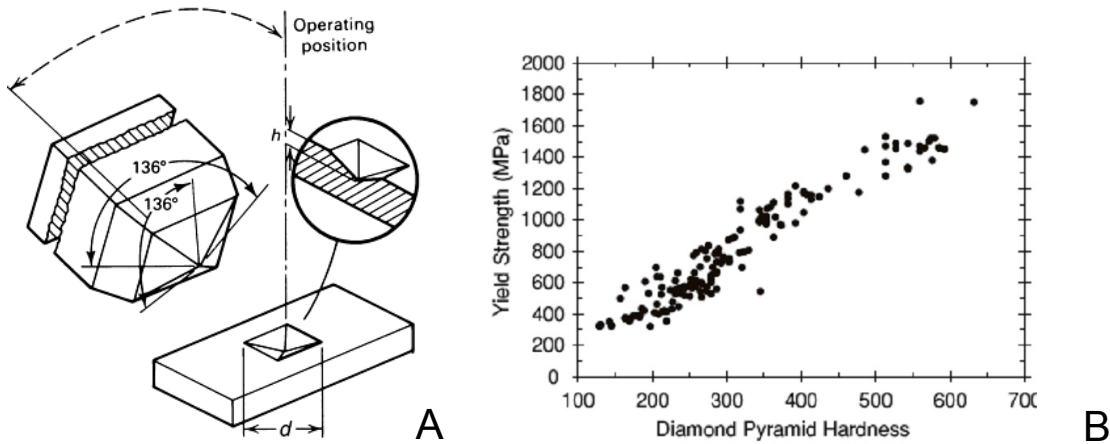


Figure 4-1. (A) Vickers indenter geometry and (B) the linear relationship between Vickers indentation hardness and Yield strength. (Figures (A) ASM handbook, 2009; (B) Pavlina and Van Tyne, 2008).

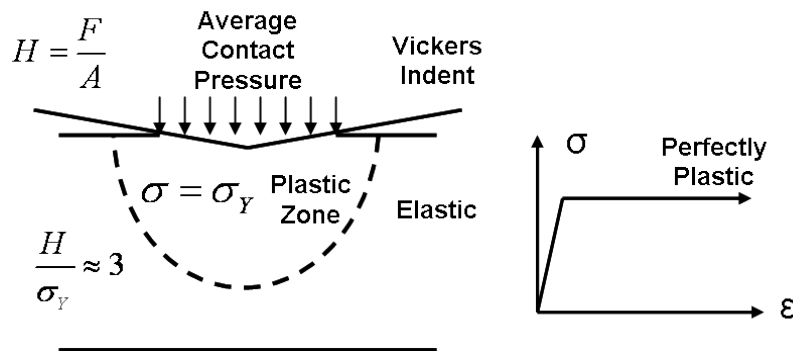


Figure 4-2. Vickers hardness is essentially the contact pressure needed to yield the indented material for this specific indenter geometry. Average flow stress within plastic zone is its yield strength for a perfectly plastic material.

For a strain hardening material, relating indentation hardness to yield strength becomes a bit more complicated. When a strain hardening material undergoes any type of permanent deformation, its yield strength (flow stress) will increase according to

how much plastic strain (ϵ_p) the material experienced. This phenomenon is governed by that specific material's stress-strain (flow) curve which can be obtained from a tension or compression test and includes many assumptions on the chosen yield criteria (Figure 4-3). As the material strain hardens, its indentation hardness also increases, thus hardness measurements can also be related to plastic strain.

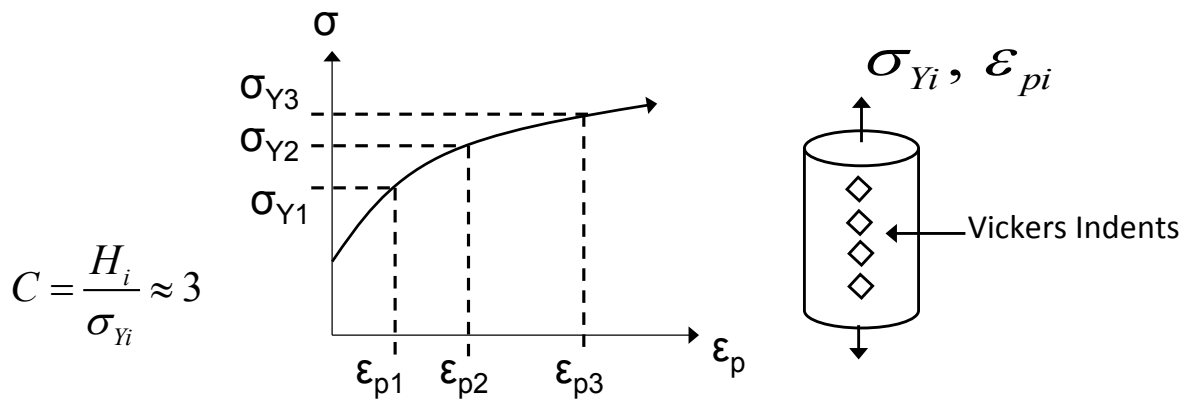


Figure 4-3. Plastic deformation increases the yield strength and hardness of a strain hardening material

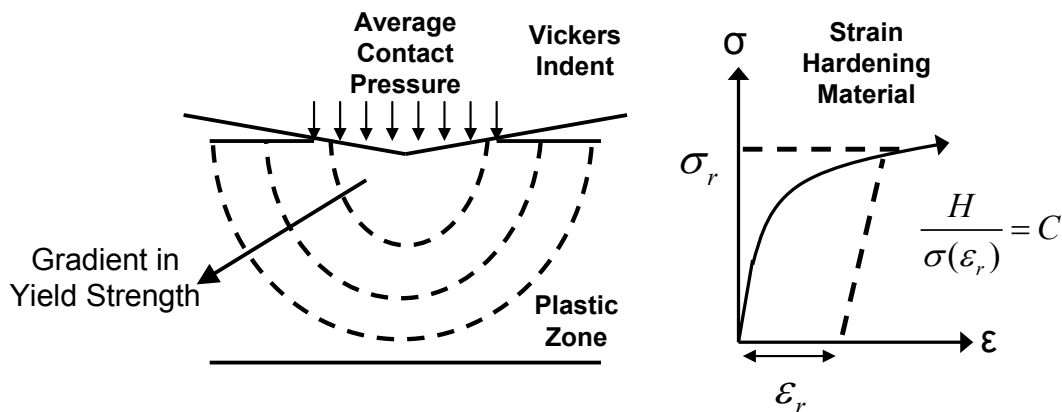


Figure 4-4. Representative flow stress and plastic strain must be used in hardness measurements for strain hardening materials.

The plastic zone induced by a Vickers indent on a strain hardening material contains a gradient in yield strength due to the gradient in plastic strain (Figure 4-4). The average contact pressure (Vickers hardness) must now be related to an average or

“representative” flow stress within the plastic zone since the stresses closest to the indent are significantly higher than its yield strength. This representative flow stress σ_r corresponds to a representative plastic strain ϵ_r on a material’s flow curve such that

$$\sigma_r = \sigma(\epsilon_r) \quad (4.2)$$

The ratio of hardness to representative flow stress is still close to three for strain hardening materials:

$$H = C\sigma(\epsilon_r), C \approx 3 \quad (4.3)$$

Predicting Increase in Hardness of Strain Hardening Material

A method that predicts the indentation hardness of a plastically-deformed strain-hardening material was first introduced by Tabor (1970) where he recorded the increase in Vickers hardness (Hv) of strain hardening materials with known amounts of initial plastic deformation (ϵ_o) (also written as ϵ_p^i throughout this document). Tabor (1970) discovered that a Vickers indent plastically deforms (and strain hardens) a region that has an initial state of plastic deformation. Thus the average or representative flow stress within the plastic zone will always be greater than the initial yield strength prior to indentation. An example of this is shown next.

Tabor (1970) utilized five specimens of mild steel and annealed copper deformed to various amounts of plastic strain ϵ_o (Table 4-1). The measured Vickers hardness of these deformed specimens is shown in the “Observed Vickers Hardness Number” column as a function of initial plastic strain (initial deformation column). The

representative plastic strain ϵ_r induced by the indent (0.08) was added to the initial plastic deformation ϵ_o of every specimen ($\epsilon_o + 8\%$ column). The flow stress corresponding to this total strain was found on the known flow curve (“Y” column). This flow stress was then multiplied by 2.9 or 3 and compared well to the measured hardness values (“cY” column).

Table 4-1. Tabor (1970) measured the increase in hardness of plastically deformed strain hardened materials. A representative strain of 8% was used to account for strain hardening induced by a Vickers indent.

Metal	Initial deformation ϵ_o (%)	($\epsilon_o + 8$) (%)	Y (kg mm ⁻²) at strain of ($\epsilon_o + 8$)%	cY (kg mm ⁻²) c = 2.9	Observed Vickers hardness number (kg mm ⁻²)
Mild steel	0	8	55	159	156
	6	14	62	176	177
	10	18	66	190	187
	13	21	67	194	193
	25	33	73	211	209
Annealed copper	0	8	15	45	39
	6	14	20	60	58
	12.5	20.5	23.3	70	69
	17.5	25.5	25	75	76
	25	33	26.6	80	81

Note that the eight % representative plastic strain is somewhat of a statistical fit and not based on the actual plastic strain gradient within the plastic zone of a Vickers indent. His method shown in Table 4-1 can be best summarized by the equation

$$H = C\sigma(\epsilon_p^i + \epsilon_r) \quad (4.4)$$

and this also predicts the hardness of materials with no initial plastic deformation (virgin materials) when $\epsilon_p^i \rightarrow 0$ and yields $H = C\sigma(\epsilon_r)$ as shown in equation 4.3. This method to predict hardness is frequently used for both metals and ceramics.

When a Vickers indent plastically deforms a strain hardening material with no initial amount of plastic deformation, the flow stresses within the plastic zone increase above the initial yield strength (Figure 4-5A). Thus the average or representative flow stress (σ_r) below the indent is greater than the yield strength (σ_y) of the material. But the measured hardness must be related to its yield strength (σ_y) as this is frequently an important design parameter in many engineering applications.

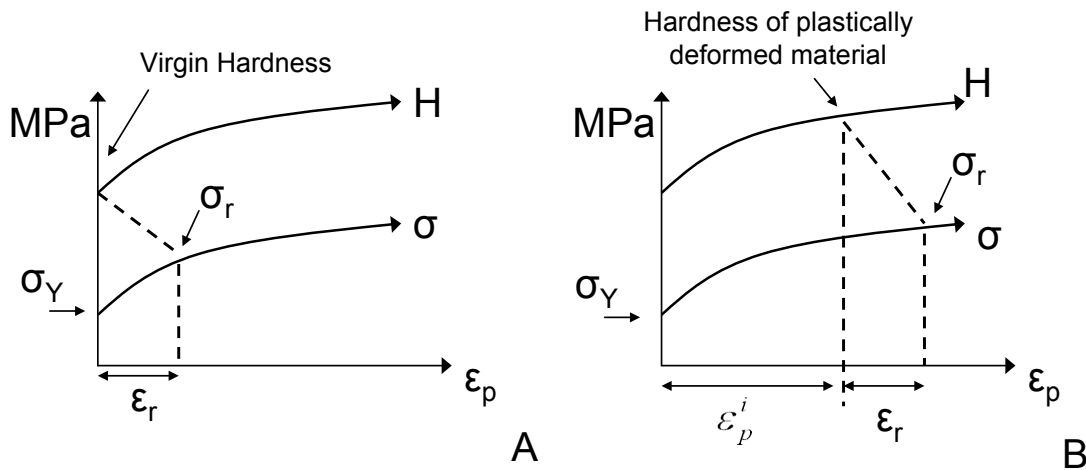


Figure 4-5. Vickers indentation strain-hardens the indented region, thus over-predicting yield strength of the material prior to indentation. The representative strain accounts for increase in flow stress due to the Vickers indent for both (A) virgin and (B) predeformed materials.

The representative plastic strain of a Vickers indent describes an average amount of plastic strain induced by the indentation process itself and by how much the representative flow stress over-predicts the yield strength of a material. Similar behavior is observed when indenting materials with an initial amount of plastic deformation, ϵ_p^i where the representative plastic strain is also used to predict the extent the representative stress exceeds the yield strength of pre-strained materials (Figure 4-5B). The process of estimating the increase in hardness of a plastically

deformed material when its flow curve is known is called a forward analysis. The opposite case when one wishes to predict a flow curve based on known measured indentation hardness values is called a reverse analysis and more difficult to perform. A new reverse analysis will be shown in Chapter 6 and will be applied to determining the plastic response of graded materials. Many different forward and reverse analyses have been proposed since Tabor, and one of the most controversial topics in these methods is how the representative plastic strain induced by an indent is defined and calculated.

Representative Plastic Strain Background

Representative plastic strain is also frequently called offset strain, average strain, and characteristic strain in the literature. Previous indentation methods that determine the plastic response of materials cannot agree on a single value for representative strain, but all agree that it is essentially a plastic strain induced by an indent that is used to relate indentation hardness to yield strength (Tabor, 1970; Chollacoop and Ramamurty, 2005; Sonmez and Demir, 2007). With advances in technology came the advent of instrumented indentation devices that could relate indentation response to a material's plastic response. Instrumented indentation devices essentially measure the indent load (P) as a function of indent depth (δ) continuously throughout the indentation process (Figure 4-6). This relationship is parabolic for most materials and the resulting loading curvature (C_v) can be unique to specific material properties.

The much referenced paper by Dao et al. (2001) predicted a material's elastic and plastic response based on its instrumented indentation loading curvature, C_v . Dao et al. (2001) created a set of dimensionless functions to characterize the indentation

response of a given range of material properties. This was done by simulating Vickers indentation of these materials and recording the loading curvatures C_v from

$$P=C_v\delta^2 \tag{4.5}$$

during indentation. The loading curvatures were plotted against the reduced modulus and both parameters were normalized with respect to a representative stress (a function of representative strain). By minimizing the error of this relationship using a least squares algorithm, a value of the representative strain of 0.033 was determined to make this relationship independent of the strain hardening exponent, n , of the power law plastic response

$$\sigma = K\varepsilon^n \tag{4.6}$$

where K is the strength coefficient.

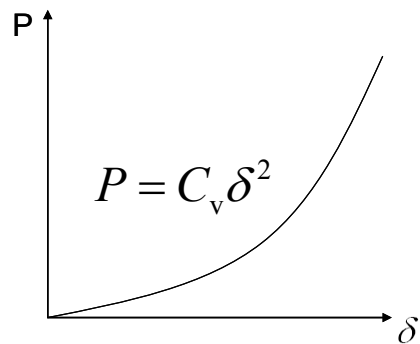


Figure 4-6. Schematic of typical instrumented indentation loading curve. P -indent load, δ -indent depth, and C_v -loading curvature.

Note this 0.033 representative plastic strain is quite different from Tabor’s 0.08, and based on the statistical fits of a chosen range of material properties. Many methods similar to Dao et al. (2001) soon followed, most of which used different values for representative plastic strain. Bucaille et al. (2003) extended the method of Dao et al. (2001) to conical indenters with different included angles and used two indenters to characterize the flow curve of a material based on its instrumented-indentation

response. Friction effects were shown to be negligible for included angles greater than 60 degrees and that the representative strain is dependent only on choice of indenter.

Ogasawara et al. (2005) extended the method of Dao et al. (2001) to three conical indenters of different included angles, determined that the range of material properties used by Dao et al. (2001) were too narrow, and that the representative strain of Dao et al. (2001) was not associated with elastic or plastic deformation. Ogasawara et al. (2005) proposed a new definition of representative strain that accounts for the biaxial nature of plastic strain common in Vickers indentation plastic zones and that its value is 0.0115 for the 70.3 degree included cone angle that is used to represent Berkovich and Vickers indenters. Ogasawara et al., (2006) created new fitting functions derived from the elastic and plastic work of the indentation response for a single indenter method while maintaining the same ϵ_r as Ogasawara et al. (2005). Chollacoop et al. (2005) showed how initial plastic deformation affects the indentation loading curvature and that the method of Dao et al. (2001) can be used to predict flow curves using two different indenters on strain hardening materials. Cao and Huber (2006) showed that the representative strain is dependent on material properties and reported ϵ_r values in the range 0.023 to 0.095.

Methods that did not use instrumented indentation also utilized different values for representative plastic strain. Johnson (1987) reported a representative strain of 0.07 based on the boundary of the large hydrostatic stress “core” directly beneath the tip of a sharp indent. Chaudhri (1998) suggested that the representative strain should be the maximum plastic strain in the plastic zone of a Vickers indent and reported values between 0.25 and 0.36. However much higher plastic strains have been observed to

occur (Dao et al., 2001; Bucaille and Felder, 2002; Bucaille et al., 2003). Tekkaya (2000) proposed a value of $\varepsilon_r = 0.112$ based on their experiments that predicted the plastic strain and increase in hardness associated with extrusion processes. Antunes et al. (2007) also expressed a need to have a material dependent representative strain and reported ε_r values to range between 0.034 and 0.042.

Most of the previous definitions of representative plastic strain were not based on a physical and measurable quantity. Rather, these parameters were calculated from curve fitting and statistical fits of the indentation responses of a certain range of material properties. The “representative strain” is really a misnomer in that it is not “representing” the actual plastic deformation within the plastic zone of a Vickers indent. Chaudhri (1998) has dubbed Tabor’s 8% strain an “undefined global value” whereas the 0.033 representative strain proposed by Dao et al. (2001) has been called a “mathematical trick” and has “no physical basis” (Ogasawara et al., 2005).

These methods are trying to find a universal value for representative strain that works for all materials. However the plastic strain induced by a Vickers indent is highly dependent on the indented material’s inherent resistance to plastic deformation which is typically characterized by the strain hardening exponent. A universal value for representative plastic strain is not expected to work for a wide range of materials.

These methods also rely heavily on the use of instrumented indentation devices in their characterization of material properties. These machines can be expensive, hard to calibrate (VanLandingham, 2003), and may not be available at certain research labs or universities. The unloading curve can estimate the strain hardening exponent and elastic modulus, but uncertainties have been identified in determining the unloading

slope (VanLandingham, 2003). The previous methods also require the running of many finite element models along with numerous dimensionless functions to characterize a given range of material properties which may not be all-encompassing. In fact some research has shown that two different materials can produce the same indentation loading curvature in single indenter methodologies (Chollacoop et al., 2003).

Average Volumetric Plastic Strain as Representative Plastic Strain

There has been a recent call to simplify indentation methodologies that are used to predict the plastic response of materials (Baxevani and Giannakopoulos, 2009). New methods are desired that do not require many FE models, instrumented indentation equipment, or multiple indenters. The method presented here is a forward analysis that meets these criteria and uses a representative plastic strain that is a calculable quantity of the plastic strain induced by an indent. The representative plastic strain used in this analysis will be the average volumetric equivalent plastic strain of a Vickers indent's plastic zone. This average plastic strain is independent of material yield strength and elastic modulus (Jayaraman et al., 1998).

The average equivalent plastic strain is defined as

$$\varepsilon_r = \frac{\sum \varepsilon_i V_i}{\sum V_i} \quad (4.7)$$

where ε_i is the equivalent plastic strain:

$$\varepsilon_i = \frac{\sqrt{2}}{3} \sqrt{(\varepsilon_{1p} - \varepsilon_{2p})^2 + (\varepsilon_{2p} - \varepsilon_{3p})^2 + (\varepsilon_{1p} - \varepsilon_{3p})^2} \quad (4.8)$$

at the centroid of an elemental volume, V_i . It has been suggested that this average strain is not a valid representative strain because it is dependent on the strain hardening

exponent and not a universal to all materials (Jayaraman et al., 1998) (Figure 4-7). But it is argued here that the representative plastic strain should be dependent on the material's capacity to strain harden because the plastic response to deformation (which is being characterized) is not the same for different strain hardening materials. One cannot assume that one representative plastic strain value will be valid for all types of materials. Jayaraman et al. (1998) has shown that this definition of ε_r is independent of elastic modulus and yield strength (Figure 4-7) and dependent only on strain hardening exponent (n). It will be shown here that it is also independent initial plastic strain for both linear and power law strain hardening materials.

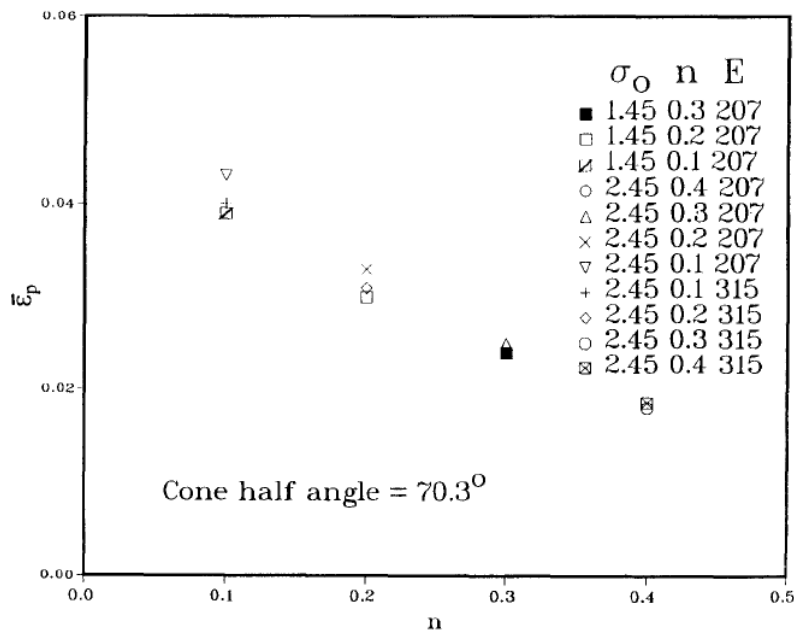


Figure 4-7. Average volumetric plastic strain induced by Vickers indent is independent of yield strength (σ_0 or σ_y) and elastic modulus (E). (Jayaraman et al., 1998).

Only equivalent plastic strains above 0.002 ($\varepsilon_i \geq 0.002$) will be included in the calculation of equation 4.7. This is due to the definition on the 0.2% offset yield strength and the $\sum V_i$ term has an increased effect on the calculation of ε_r when virtually-zero

plastic strains are included. Bucaille and Felder (2002) used a similar definition of ε_r in their simulations of indentation and scratch tests of perfectly plastic materials. They limited their definition of ε_i to fall within the range of $0.1\varepsilon_{eq}^c \leq \varepsilon_i \leq \varepsilon_{eq}^c$ where ε_{eq}^c is an arbitrarily chosen “critical plastic strain” ranging from 0.1 to 2.5. They admit their definition of ε_r is highly dependent on the choice of critical plastic strain and consequently focuses only on the ratio of ε_r when comparing scratch and indentation plastic zones.

Forward Analysis

To show the validity and application of a material dependent representative plastic strain, the relationship between indentation hardness and a material’s plastic response will be demonstrated for two commercially available materials, Pyrowear 675 Stainless Steel (P675) with a power-law strain-hardening response and 303 Stainless Steel which follows a linear strain-hardening response. P675 is typically case-hardened, but in the current analysis only the core (non-carburized and nongraded) region is investigated.

To induce a large magnitude and gradient in plastic strain macro-Vickers indents are performed on these two virgin materials. These specimens are sectioned slightly away from the indent center and gradually polished to the cross-section corresponding to the maximum plastic zone depth. The plastic strain magnitude beneath a macro-indent varies spatially over the plastic zone with highest plastic strains at the indenter tip and decrease gradually with distance away from the tip.

The increase in indentation hardness across this plastic strain gradient is determined by conducting micro-Vickers indents (at 200 grams load) along the centerline of the macro-indent's plastic zone. A finite element model of the macro-indentation process will use the stress-strain response obtained from in-house compression-tests to determine the resulting plastic strain gradient ε_p^i within the macro-indent's plastic zone. By utilizing the definition of a material-dependent representative plastic strain induced by the micro-Vickers indent, the increase in micro-Vickers hardness values will then be predicted and compared to those measured experimentally. Micro-Vickers indentations within this plastic zone will be simulated to verify the representative plastic strain for pre-plastically deformed regions. This study will utilize both Vickers and Rockwell-C macro indenters to illustrate that the current procedure of predicting the increase in hardness within a plastic zone works regardless of the method by which the plastic deformation is produced.

Experimental Procedure

To induce a large plastic zone on the core region of the P675 specimen, a standard LECO Vickers indenter tip (Model # 860-539, 1.5 mm maximum diagonal) was fixed in a custom fabricated housing and mounted to a universal testing machine (MTS® Alliance™ RT/30, Figure 4-8b). A load of 204Kg was used to create the desired macro-Vickers indent. The measured Vickers hardness was 433 Hv. A standard Rockwell-C macro-indent was produced on the 303 SS specimen using the standard 150Kg Rockwell C indent load which resulted in a measured hardness of 26 HRC (275 Hv).

After indentation, these macro-indented specimens were sectioned close to the indent and progressively polished to reveal the indent cross-section at the maximum

indent depth. Standard metallographic polishing procedures which use progressively smaller polishing media were utilized to minimize damage and residual stresses induced by grinding and polishing (ASM handbook, 2009).

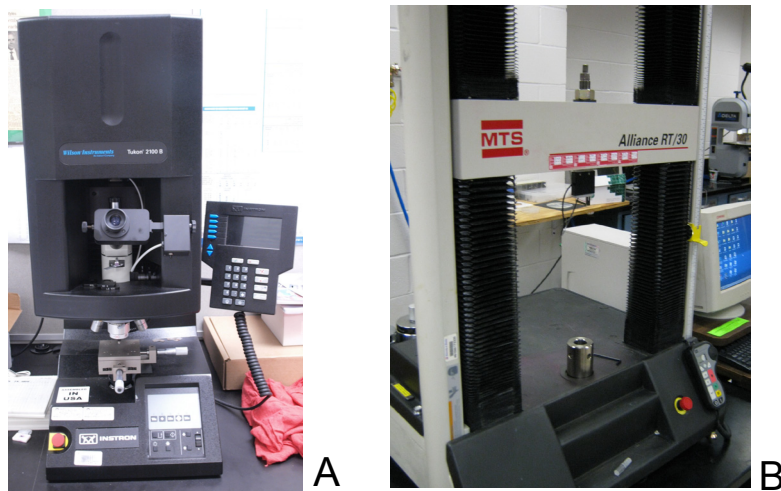


Figure 4-8. (A) Wilson® Instruments Tukon™ 2100 B Vickers indenter and (B) MTS® Alliance™ RT/30 machine.

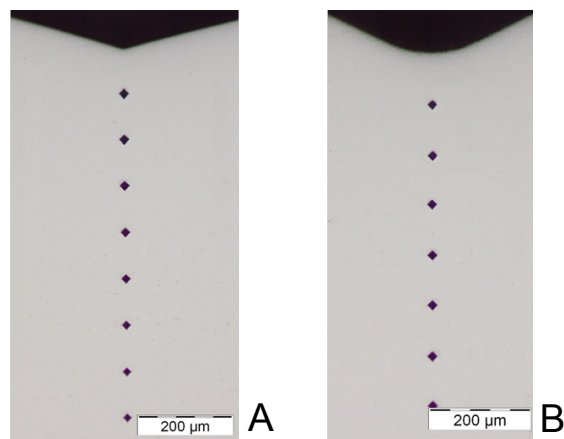


Figure 4-9. Micro Vickers indentations within plastic zones of (A) macro Vickers indent on P675 Core, and (B) Rockwell C indent on 303 Stainless Steel. Macro and micro indents performed by M. A. Klecka.

To measure the increase in hardness within these plastic zones, micro-Vickers indents were conducted using a Wilson® Instruments (Tukon™ 2100 B) Vickers indenter at 200 grams indent load and 15 seconds loading duration (Figure 4-8). As per ASTM standard, ASTM E384, the micro-Vickers indents along the centerline of the

plastic zone were spaced 100 micrometers apart, as shown in Figure 4-9, to prevent interaction with neighboring indents.

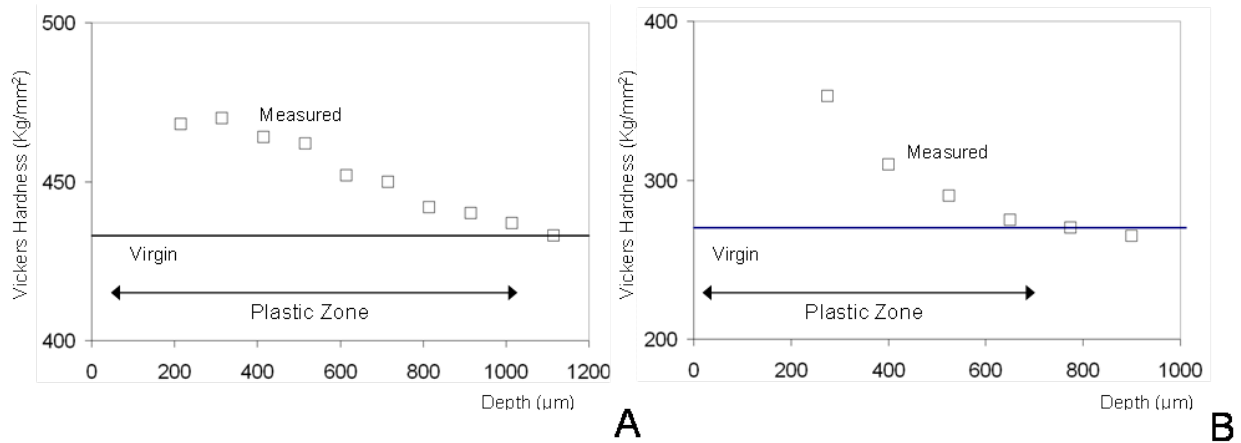


Figure 4-10. Plot of measured increase in Vickers hardness within plastic zone of (A) Vickers macro indent of P675 and (B) Rockwell C indent of 303 stainless steel.

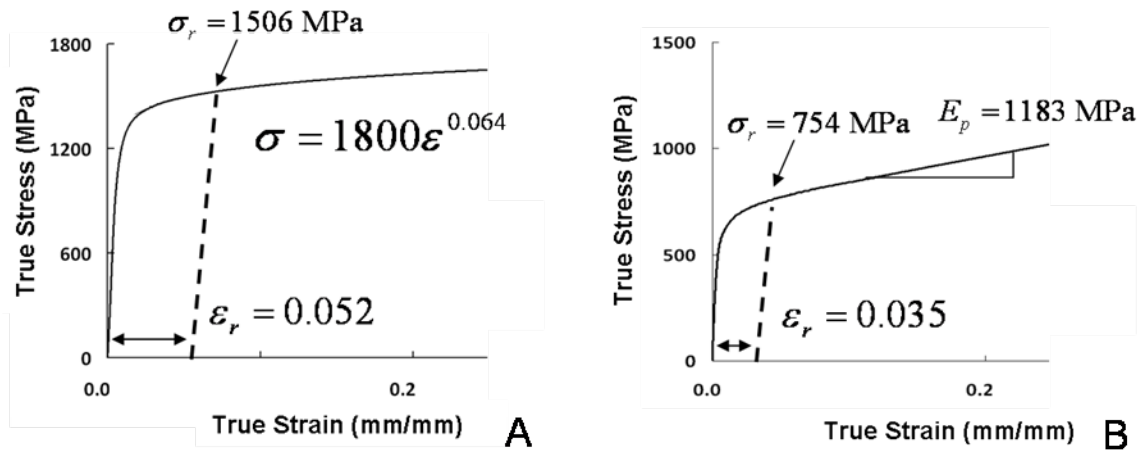


Figure 4-11. Flow curves taken from compression tests of (A) P675 and (B) 303 stainless steels. In-house compression tests performed by M. A. Klecka.

The resulting increase in hardness is shown in Figure 4-10 with respect to its virgin state. Similar procedures of the micro-indentation of the plastic zone beneath a macro-indent were also implemented by (Chaudhri, 1998; Srikant et al., 2006). Micro indentations were performed along the plastic zone’s centerline because this

corresponds to the deepest plastic zone depth, and consequently, the most amount of usable increased-hardness data.

The stress-strain curves obtained from in-house compression tests on P675 steel and 303 steel specimens are shown in Figure 4-11. Note that P675 follows a power-law model with strength coefficient $K=1800$ MPa and strain hardening exponent $n=0.064$ and the 303 steel can be modeled as a linearly hardening material with tangent modulus of 1183 MPa. The values for ϵ_r shown in Figure 4-11 were calculated by importing these constitutive responses to the finite element models of the micro-Vickers indentation of these two materials and calculating the average plastic strain within the plastic zone which will be described later.

Finite Element Model

The purpose of the two macro-indenters was to create two different plastic strain gradients on two materials, thus two separate FE models were created to simulate the macro-Vickers indent on P675 (Figure 4-12A) and Rockwell C macro-indent on 303 steel (Figure 4-12B). Both indenters were displacement controlled to the same macro-indent depths as in the experiment and then retracted to their original positions.

The indenters were given fixed rotational boundary conditions and only translated normal to the indented surface. A rigid indenter with an equivalent half cone angle of 70.3 degrees produces the same projected indent area as a Vickers indent for any given indent depth and was used to simulate the macro-Vickers indent on P675. For the Rockwell C indent, a similar analysis was performed on the 303 model using the standard Rockwell C indent geometry. Five thousand four-node bilinear quadrilateral axisymmetric elements make up the FE models with the finest mesh in the region of the

indented material. There are at least 20 elements in contact with the indenter during maximum indent depth which provides sufficient resolution.

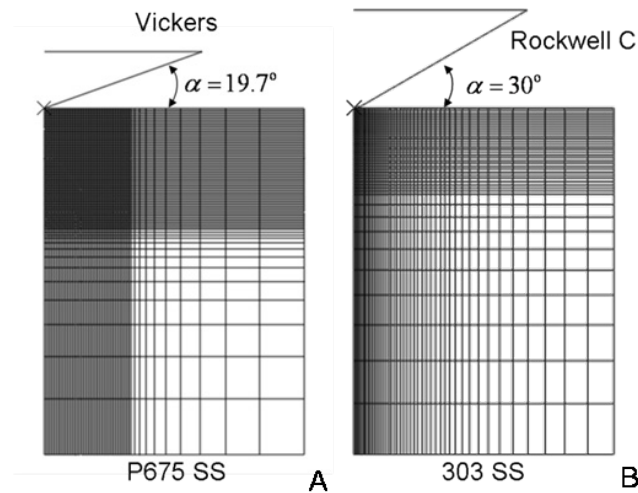


Figure 4-12. Finite element models of the (A) Vickers macro indentation of P675 core and (B) Rockwell C macro indentation of 303 stainless steel.

The FE model is implemented in ABAQUS 6.7-1 and the material's plastic response is governed by the von Mises (J2) yield criterion, associated flow rule, isotropic hardening, and the constitutive responses obtained from the compression tests shown in Figure 4-11. The micro-Vickers indentations for both materials were also simulated in the plastically deformed and undeformed regions along the centerline of the macro-indent's plastic zones previously mentioned (Figure 4-9), using the same FE mesh and indent geometry as Figure 4-12A. These results will be used to verify the same representative plastic strain for both plastically deformed and virgin materials which is discussed later.

Results and Discussion

The plastic strain contours below the macro-Vickers indent of P675 and Rockwell C macro-indent of 303 steel as calculated from the FE models are shown in Figure 4-13A and Figure 4-13B, respectively. Note that the plastic strain gradients are not the

same due to the differences in plastic response of both materials and indenter geometries. Because the indent depth is the same in both the experiments and FE simulations, a direct comparison of the measured increase in micro-indentation hardness within these plastic zones of Figure 4-9 can now be made to those predicted by the FE model, but the representative plastic strain induced by the micro-Vickers indents must be determined beforehand.

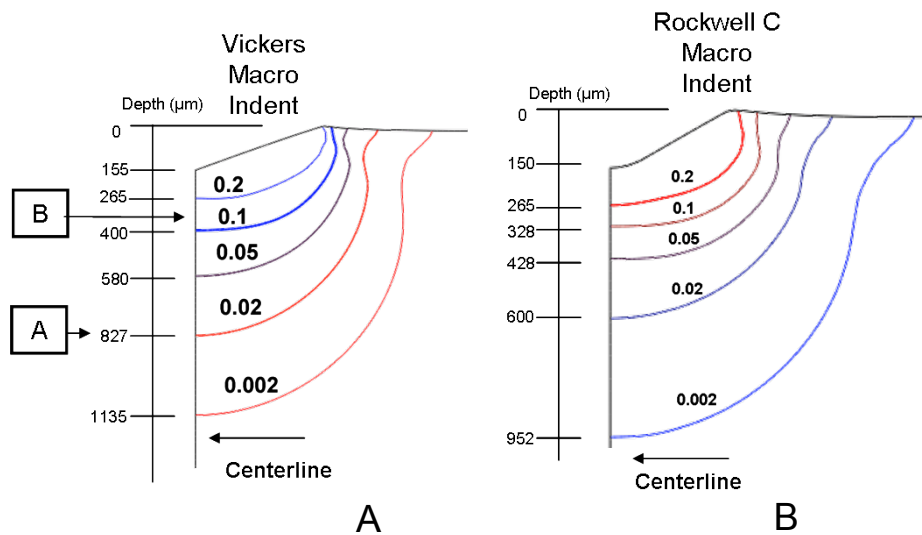


Figure 4-13. Plastic strain contours for (A) Vickers macro-indent of P675 stainless steel and (B) Rockwell C macro-indent of 303 stainless steel. Plastic strains along centerline are used to predict indentation hardness and later compared to measured micro-indents along same centerline of actual deformed specimen (Figure 4-9).

The plastic strain contours around a micro-Vickers indent for these two materials are calculated by the FE model shown in Figure 4-12A using the plastic responses shown in Figure 4-11. The representative plastic strain is the same for both micro and macro Vickers indents since the deformation of Vickers indentation is self-similar with respect to indent depth (excluding indentation size effects which were not observed for these two materials at the chosen indent loads). As such, the depths of the plastic strain contours are non-dimensional with respect to indent depth in Figure 4-14 where

the plastic strain contours around the micro-Vickers indents of both virgin P675 and 303 steels are shown.

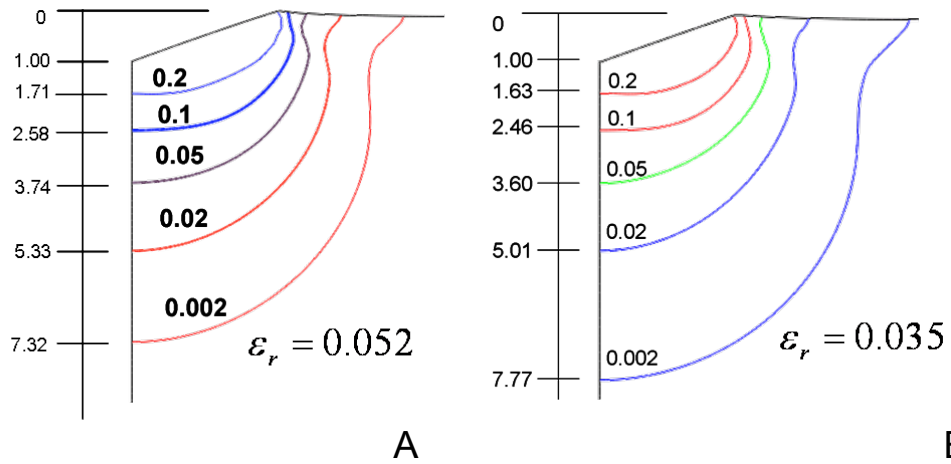


Figure 4-14. Plastic strain contours beneath micro Vickers indents for (A) P675 and (B) 303 stainless steels.

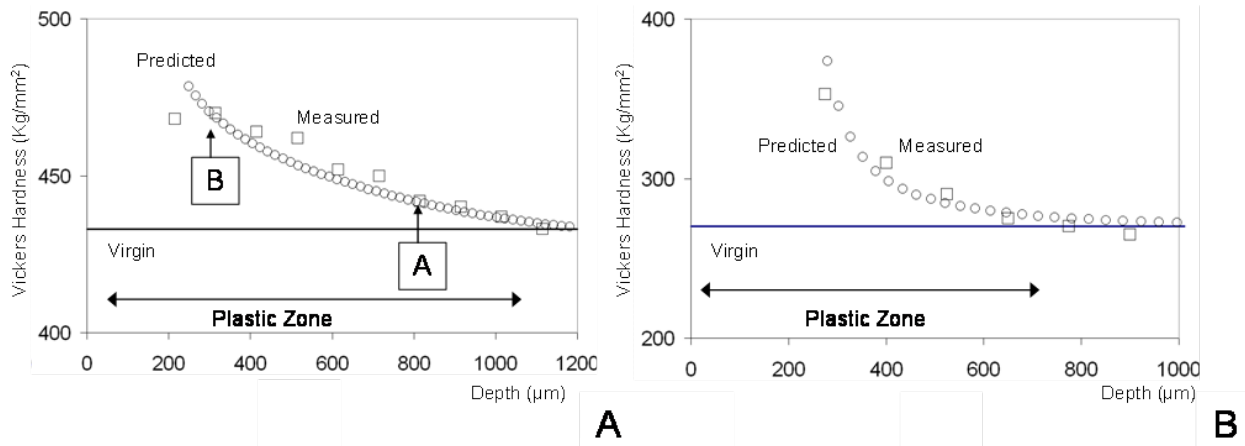


Figure 4-15. Predicted versus measured hardness values beneath (A) macro Vickers indent of P675 and (B) Rockwell C indent of 303 stainless steel.

The plastic strain values of Figure 4-14, along with equation 4.7, were used to determine values for ϵ_r as 0.052 and 0.035 for P675 and 303 steel, respectively. Here, ϵ_i is taken from the results of Figure 4-14 and V_i is the volume of a plastically deformed finite element. These results compared well to the average plastic strain induced by Vickers indents calculated by Jayaraman et al. (1998). It will be shown later that this

representative plastic strain is independent of the initial plastic strain of the indented material as well.

The corresponding representative flow stress σ_r and constraint factor $C = \frac{H}{\sigma_r}$ can now be calculated as 2.8 and 3.5 for P675 and 303 steel, respectively. While the magnitudes of plastic strain contours are the same in Figure 4-14, the differences in spatial variation are due to the difference in plastic response of P675 and 303 steel. P675 has a higher yield strength (1300 MPa) than that of 303 SS (600 MPa), but has a lower strain-hardening rate ($n=0.064$) than that of 303 SS ($E_p=1183$ MPa). This causes the strain gradient to be slightly more severe below the Vickers-indent's tip in 303 SS (due to higher strain-hardening), but more spread out (lower yield strength) when compared to P675 (Figure 4-14).

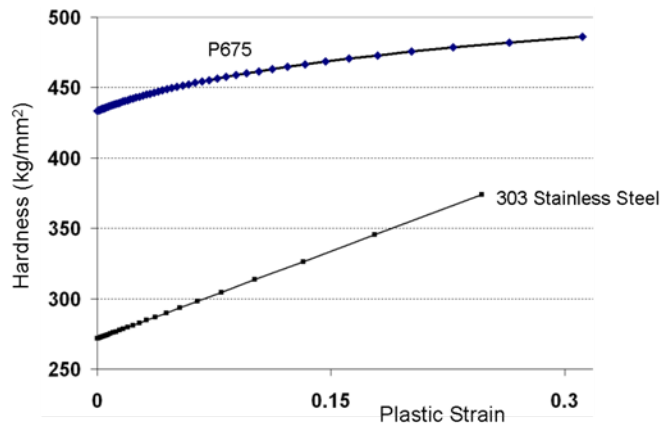


Figure 4-16. Vickers hardness as a function of plastic strain for P675 and 303 stainless steels.

The plastic strain gradient along the centerline of each macro-indent's plastic zone is now used to predict the increase in micro-Vickers hardness using the

equation, $H = C\sigma(\varepsilon_p^i + \varepsilon_r)$ where ε_p^i is the initial equivalent plastic strain along the centerline of the plastic zone (Figure 4-13) and ε_r is the material-specific representative

plastic strain induced by the individual micro-Vickers indents (Figure 4-14) at each micro-indent location. The predicted micro-indentation hardness values are now compared to the experimentally measured hardness values along the centerline of the plastic zone as shown in Figure 4-15. There is a good agreement between these values for both Vickers and Rockwell C macro-indents which validates the use of a material-dependent representative plastic strain in the prediction of Vickers indentation hardness.

The increase in Vickers hardness as a function of plastic strain can now be calculated using these results. This information is useful in metal forming processes where local hardness measurements can be used to estimate the magnitude of equivalent plastic strain on a cold formed part (Sonmez and Demir, 2007). The calculated Vickers hardness as a function of plastic strain for P675 and 303 steel are shown in Figure 4-16.

Representative Plastic Strain of an Initially Plastically Deformed Material

Previously, the representative plastic strain ϵ_r was added to the initial local plastic strain ϵ_p^i to calculate the increase in micro-Vickers hardness because the micro-indentation process plastically deforms and further strain-hardens the initially plastically deformed region (Tabor, 1970). A key assumption of this analysis is the representative plastic strain induced by the micro-Vickers indent is independent of the magnitude of the initial plastic strain of the indented material.

To illustrate this point, the micro-Vickers indents at points along the centerline of the plastic zone of the P675 steel specimen's macro-indent were simulated. At each location, a uniform distribution of initial equivalent plastic strain magnitude over the

small area of the micro-indent is assumed. The calculated equivalent plastic strain magnitudes at locations A and B were 0.02 and 0.146 as illustrated in Figure 4-13A, and the experimentally measured Vickers hardness values were 442 Hv and 470 Hv, respectively (Figure 4-15A). The same FE mesh of Vickers indentation from Figure 4-12A is used again for the simulations of the micro-Vickers indents of the pre-strained points (A and B), except radial plastic strain magnitudes of 0.01 and 0.073 are now applied to plastically strain-harden the material to the equivalent plastic strain states of 0.02 and 0.146, respectively, prior to indentation (Figure 4-17) as predicted by the Cauchy's strain-displacement equations for a cylindrical coordinate system.

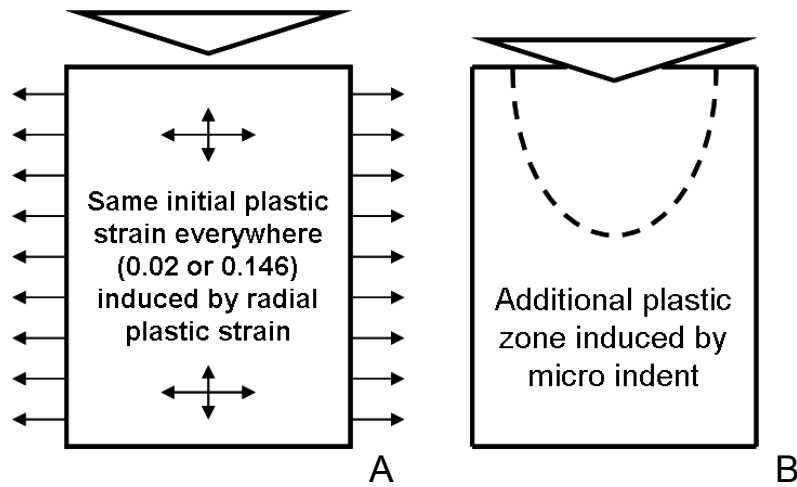


Figure 4-17. Schematic of the micro-Vickers indent of a pre-strained material: (A) region with same initial equivalent plastic strain throughout material prior to indentation and (B) illustration of additional plastic strain induced by the micro-indent.

The modified equation 4-7 is then written as $\varepsilon_r = \frac{\sum (\varepsilon_j - \varepsilon_p^i) V_j}{\sum V_j}$ where ε_p^i is the

initial equivalent plastic strain magnitude (0.02 or 0.146) of the indented material which must be subtracted from the total equivalent plastic strain at every point within the new plastic zone to determine the contribution of the additional plastic strain induced by the

Vickers micro-indent at locations A and B. This is the same ε_p^i that was used in Figure 4-13A, but is expected to be constant over the micro-indented area.

The representative plastic strain induced by the Vickers micro-indent is calculated and found to be the same as the virgin material, i.e. $\varepsilon_p = 0.052$ for both points A and B of the pre-deformed P675 steel. Figure 4-18 shows the additional plastic zone induced by the Vickers micro-indent at point B with initial equivalent plastic strain of 0.146. Note the plastic strain gradient is similar to that of the virgin material (Figure 4-14A), in the sense that the plastic strain contours shown have an increased plastic strain magnitude of 0.146 at relatively the same locations within its plastic zone. However, the plastic zone in Figure 4-18 is shallower with respect to indent depth due the strain hardening and increased yield strength of point B prior to indentation. Interestingly, the representative plastic strain (average-additional plastic strain) remains the same.

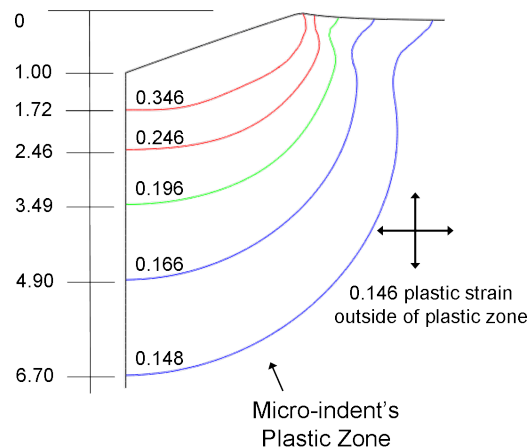


Figure 4-18. Plastic strain contours of Vickers micro-indent on pre-plastically strained P675 steel at point B in Figures 4-13a and 4-15a. Depth is non-dimensionalized with respect to residual indent depth.

Key Points

The results of this analysis are currently under peer review for publication in Acta Materialia and a few key points are outlined here:

- This exercise demonstrates that the material-dependent volumetric average plastic strain induced by a Vickers indent is a valid representative plastic strain in the conversion of hardness to flow stress and independent of the initial plastic strain of an indented material.
- Vickers and Rockwell C macro-indentations were chosen in these experiments because they are relatively simple and inexpensive to produce and can create a controlled and convenient plastic strain gradients with plastic strains as high as 0.4. Such large plastic strains may otherwise be unobtainable in tension or compression tests or other modes of deformation. The large hydrostatic stresses and confinement associated with indentation prevent premature failure and make these high plastic strains possible. These plastic zones are relatively small in size which allows for multiple tests on a single specimen.
- Previous indentation methods do not examine the plastic zone to this detail nor has anyone verified the assumption that the representative strain is not a function of pre-plastic strain using finite element models of Vickers indentation with comparisons to experimental hardness data.
- This method predicts the increase in indentation hardness within the plastic zone of both Vickers and Rockwell C macro-indents and compared well to the experimentally measured micro-indent mapping for the plastic zones of 303 stainless steel and Pyrowear 675.

This method of relating indentation hardness to the plastic response for non-graded materials using a material-dependent representative plastic strain will be used in Chapters 5 and 6 to determine the plastic response of graded materials such as P675 and M50 NiL case-hardened bearing steels. These graded material properties are needed to better understand spall propagation that occurs within the case layer of M50 NiL. If a material's plastic response is proven to affect spall propagation, this information can be used to design bearings with slower spall-propagation rates.

CHAPTER 5 INDENTATION OF GRADED MATERIALS

History of Graded Materials

The previous method in Chapter 4 was successful in determining relationships between indentation hardness and material plastic response using a material-dependent representative plastic strain; however methods to determine the plastic response of graded materials are much more complicated. A plastically graded material (PGM) is simply a substance that has a variation in plastic material response with depth from its surface. It is possible that the plastic response of plastically-graded, case-hardened M50 NiL bearing steel is affecting the spall propagation rate as shown in Chapter 1. Graded materials are not unique to bearings and can be found throughout the history of engineering as well as in nature.



Figure 5-1. Graded materials seen in nature (Grand Canyon) and in human-history (Japanese Katana)

Graded materials designed for a specific task have been around since the 1400's. The sharp cutting surface of the katana Japanese sword was made out of hard high-carbon steel while the core of the sword consisted of a softer low-carbon steel to absorb most of the impact and deformation. Special quenching techniques forced martensite to form predominately on the cutting edge making it very hard and allowing it to retain its sharpness with continued use (Figure 5-1).

Graded materials are also frequently seen in biology and nature. Tooth enamel is the hardest substance of the human body which reduces teeth wear from a lifetime of chewing food and protects the softer dentine inner region of a tooth. Other bones in the body have similar hard surfaces that protect the softer bone marrow within. The earth's surface is also graded and evidence can be seen in such places as the Grand Canyon. The gradation from topsoil to bedrock influences the design of foundations for large buildings. Graded materials that have soft surfaces and a progressively harder subsurface are often used in impact-energy absorption applications. The soft surface absorbs the energy from impact while the harder subsurface region maintains structural shape and integrity. This is frequently seen in packaging by wrapping objects in bubble wrap.

Graded materials with hard surfaces are desirable in mechanical components such as gears and bearings where a hard and strong surface can withstand the large contact stresses at the interface of contacting components while the ductile core transmits the bulk of the shaft or thrust loads. Very hard surfaces are resistant to wear and this greatly increases the rolling or sliding contact fatigue life of these components which affects the overall health and performance of an engine.

Hardening the surfaces of these components is done in many different ways. The most popular are carburizing, nitriding, or boriding, where carbon, nitrogen, or boron is diffused into the surface of a part at relatively high temperature. These diffused atoms are located at interstitial locations within the atomic lattice. This, along with special quenching techniques, hinders plastic deformation and effectively makes the material harder and stronger. The resulting variation in plastic response within a graded material

is difficult to determine by traditional methods such as compression or tension tests due to the interactions of the stronger and weaker regions and complications in fabricating a test specimen with the same composition as a given point within the graded region. Despite these difficulties, the variation in material properties are needed to design stronger and longer lasting mechanical parts. Understanding how diffusion and heat treatment affect the plastic response is crucial. There are many different ways to estimate material properties; one of the simpler and easier methods is through indentation analysis.

Previous Methods to Determine Plastic Response of PGMs

Instrumented indentation of graded materials is a relatively new area of research. Nakamura et al. (2000) used instrumented ball indentation and Kalman filtering techniques to estimate the variation in plastic response of PGMs. They used a standard rule of mixtures to determine the stress and strain contributions from the metal and ceramic portions of the PGM. The variation in ceramic phase fraction resulted in a change in plastic response with depth. The plastic responses of both ceramic and metal phases must be known a priori. A set of PGM indentation reference behavior was created by many FE model simulations and experimental verification of this method was done by Gu et al. (2003).

Giannakopoulos (2002) used analytical and numerical methods to analyze the deformation induced by sharp indentation of PGMs, but this was limited to nonlinear elastic and perfectly plastic materials. Nayebi et al. (2002) predicted the decreasing hardness profile of nitrided steels using instrumented ball indentation and finite element analysis.

Cao and Lu (2004) used finite element analysis to simulate conical indentation of PGMs and the resulting load displacement curves were used in a reverse analysis to predict its plastic response. Their analysis used the method of Dao et al. (2001) to determine a set of dimensionless functions that describe the indentation behavior of PGMs for various gradients in yield strength only. The resulting indentation loading curvature (C_v) can vary with indentation depth (d) for a PGM and reflects the degree of gradation in subsurface yield strength.

Choi et al. (2008) showed how the yield strength gradient of a PGM affects indentation loading curvature, distribution of maximum principal and von Mises stresses, and equivalent plastic strain gradient within the plastic zone of a conical indent. They used dimensionless functions that describe the indentation loading curvatures taken from homogeneous elastic materials (Johnson, 1987) and non-graded elasto-plastic materials (Dao et al., 2001) to create a new dimensionless function that describes the indentation loading curvature of PGMs. Experimental validation was done by Choi et al. (2008) on graded materials created by electro-deposition techniques which created a variation in grain size and consequently yield strength.

The above mentioned PGM indentation methods relied heavily upon instrumented sharp or ball indentation. These devices are expensive, hard to calibrate (VanLandingham, 2003), and may not be available at some research labs or universities. Also, two different strain hardening materials can produce the same indentation loading curvature in single indenter methodologies (Chollacoop et al., 2003).

Most of the previous methods assumed only a variation in yield strength with no change in parameters such as strain hardening exponent. Some of these methods

analyzed materials that were created in labs by electro-deposition or thermal-spraying by plasma guns. However, these are not good examples of engineering materials that are needed to survive the harsh environments frequently experienced in jet engine bearings. These methods investigated how the variations in plastic response affected the indentation loading curvature of PGMs. Very few of these methods investigated the actual plastic deformation induced by the indentation of PGMs. In just about all of the methods the material properties of the surface or substrate were required to estimate the material properties of neighboring graded material. These methods needed many FE model simulations and used complex algorithms such as Kalman filtering techniques or curve fitting dimensionless functions to encompass the indentation behavior of a given range of material properties. Ogasawara et al. (2007) has shown that some of these ranges of material properties may not be broad enough to encompass all engineering materials.

Proposed Method

The method presented here will use macro and micro Vickers indentation and elastic-plastic finite element analysis (FEA) to determine the variation in constitutive response of the plastically graded, case hardened region of Pyrowear 675 (P675) stainless steel which is frequently used in current high-performance aerospace bearings and gears. The PGM utilized here has a variation in plastic response with depth, but constant elastic modulus. The fact that a strain hardening material exhibits an increase in hardness due to plastic deformation compared to its virgin hardness is utilized here in both the measurement and prediction of Vickers hardness for a relatively large magnitude and range of plastic strain within this PGM.

A convenient and controlled way to induce large magnitudes of plastic strain within a PGM is via macro-Vickers indentation which induces a plastic strain gradient throughout its plastic zone (Figure 5-1) that is symmetric about its centerline. Within this region of plastic deformation, the material will strain harden according to its plastic response and consequently display an increase in indentation hardness with respect to its virgin state.

The principal concept of this analysis is that the increase in hardness (converted to flow stress using the analysis of Chapter 4) at a given depth with respect to its virgin state must fall on the flow curve defined at that depth as depicted in Figure 5-1. The increase in hardness within the plastic zone is experimentally measured by micro-Vickers indentations which are then compared to those predicted by finite element models described later. The micro-indent ($\approx 200\text{g}$ indent load) essentially probe the increased yield strength within the plastic zone of the macro-indent ($>150\text{Kg}$). The increase in yield strength can be predicted by finite element modeling provided the appropriate flow curves are used at every point throughout the PGM. The increased yield strength will correspond to a certain amount of plastic strain which is dependent on the strain hardening characteristics of the flow curves which vary with depth.

As an example, for a PGM with decreasing hardness with depth (Figure 5-1) the yield strength is also expected to decrease since hardness is indicative of yield strength (Tabor, 1970). Thus the micro-hardness values at a specific depth from the surface and within the plastic zone will provide the increased flow stresses that must fall on the flow curve at that depth. Outside of the plastic zone, any hardness measurements will reflect the virgin (undeformed) initial yield strength at that depth.

For instance, the hardness measurement at location n in Figure 5-1 will probe the yield strength of a virgin region because it is outside of the plastic zone caused by the macro-indent. The hardness measurements along Row a are expected to be greater than the hardness at n due to the strain-hardening within the plastic zone, while keeping in mind that the flow stresses for any material point along Row a must fall on the same flow curve as point n .

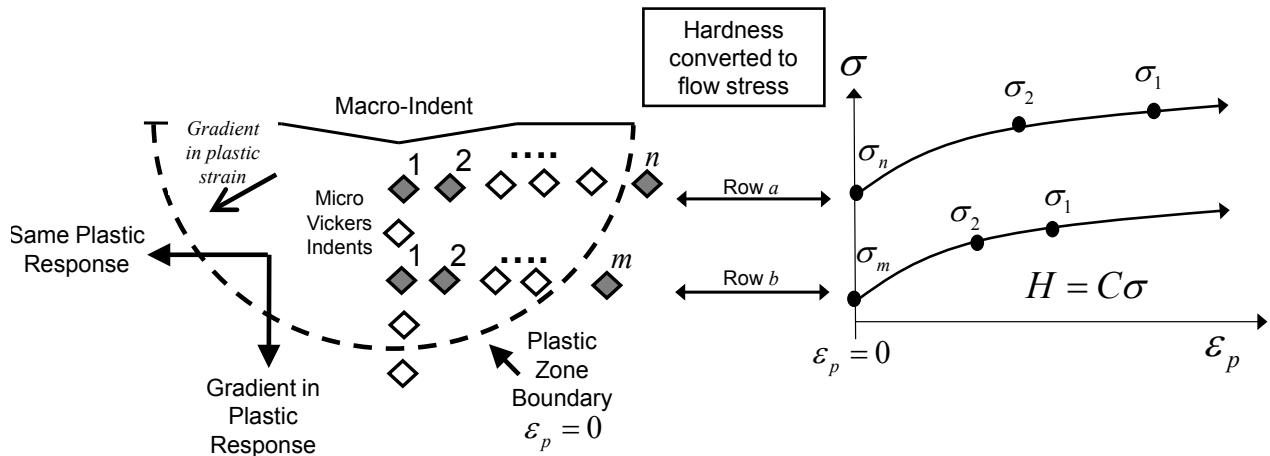


Figure 5-1. Schematic of the relationship between indentation hardness and plastic response at any given depth within the plastic zone of a PGM.

The same holds true for Row b and point m , but the magnitudes would be lower due to the decreasing-hardness trend in this PGM example. This information, along with the corresponding plastic strain obtained from FE models, will be utilized to determine the variation in plastic response with depth for this commercially available, case hardened P675 stainless steel by using the relationship between Vickers hardness and yield strength described in Chapter 4, namely $H = C\sigma(\epsilon_r + \epsilon_p)$ where ϵ_p is the initial plastic strain within the macro indent's plastic zone, ϵ_r is the representative plastic strain induced by the micro-indentation process, and C is the constraint factor. All of these terms will vary with depth for a plastically deformed, graded material.

Material

Prior to carburization and heat treatment, the P675 steel contains only 0.07% carbon. After carburization, the surface of the case-hardened layer can contain up to 1% carbon which decreases with depth due to the carbon diffusion process. Additional heat treatment involving double-tempering is used to lock in the final microstructure of 2 μm in size which consists of tempered martensite and dispersed carbide particles. The variation of carbide particle volume fraction with depth results in a variation in hardness and plastic response over the case hardened region. Note the high Chromium content for this stainless steel in Table 5-1.

Table 5-1. Material composition of P675 Stainless Steel (Carpenter, 2009).

Element	wt%	Element	wt %
Carbon	0.07	Manganese	0.65
Silicon	0.40	Chromium	13.00
Nickel	2.60	Molybdenum	1.80
Cobalt	5.40	Vanadium	0.60

To determine the variation in virgin hardness with depth within this specific PGM, the samples were sectioned, ground, and polished on surfaces parallel to the carbon gradient. Standard metallographic polishing procedures which use progressively finer polishing media were used to minimize damage and residual stresses induced by polishing (ASM Handbook, 2009). Micro Vickers-indentations were conducted on this cross-section using a Wilson® Instruments (Tukon™ 2100B) Vickers indenter (Figure 5-4A) at 200g, 500g, and 1Kg indent loads for 15 seconds loading duration. The indents were spaced 2.5 times the indent diagonal to prevent interactions with neighboring indents as per ASTM E384 standard.

The Vickers hardness versus depth profile shown in Figure 5-2 for the virgin P675 steel depicts negligible indentation size effect (ISE) for this chosen indent load range.

The plot reveals that hardness varies linearly from 930 Hv at the surface to 433 Hv over a depth of 2mm, after which the hardness remains constant in the core region.

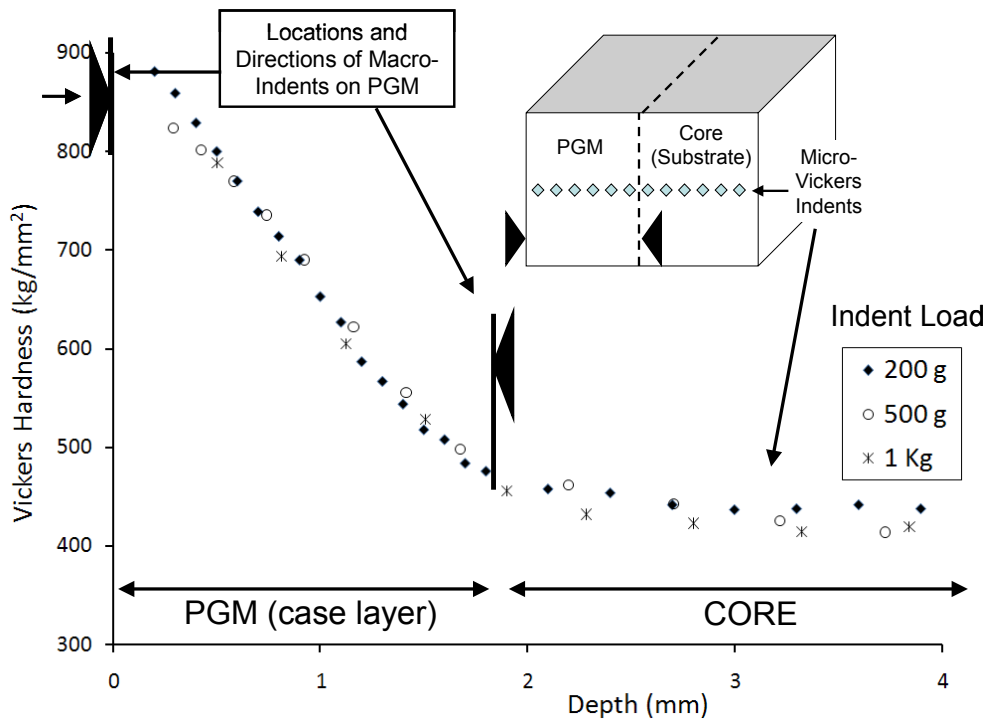


Figure 5-2. Variation in micro-Vickers hardness with depth within a virgin P675 graded material. Three different indent loads show very little indentation size effect (ISE). Micro Vickers indents performed by M.A. Klecka.

The graded case hardened region will be the PGM of interest for this investigation. The plastic response of the core, non-graded region will be obtained by a traditional compression test. The resulting plastic response is considered to be representative of the PGM's softest region and provides a lower bound of possible plastic behavior for the entire PGM (Figure 5-3).

Experimental Procedure

To induce a large magnitude and gradient in plastic strain within the graded material, macro-Vickers indents were produced at large loads (up to 330 Kg) using a standard Vickers indenter. The indenter was fixed in a custom housing and mounted in

a Universal Testing Machine load frame (MTS Alliance™ RT/30) (Figure 5-4B) and driven in load control for 15 seconds. A macro-Vickers indent was conducted on the hardest surface (930 Hv Figure 5-2) of the PGM in the direction of decreasing hardness, (i.e. hard to soft).

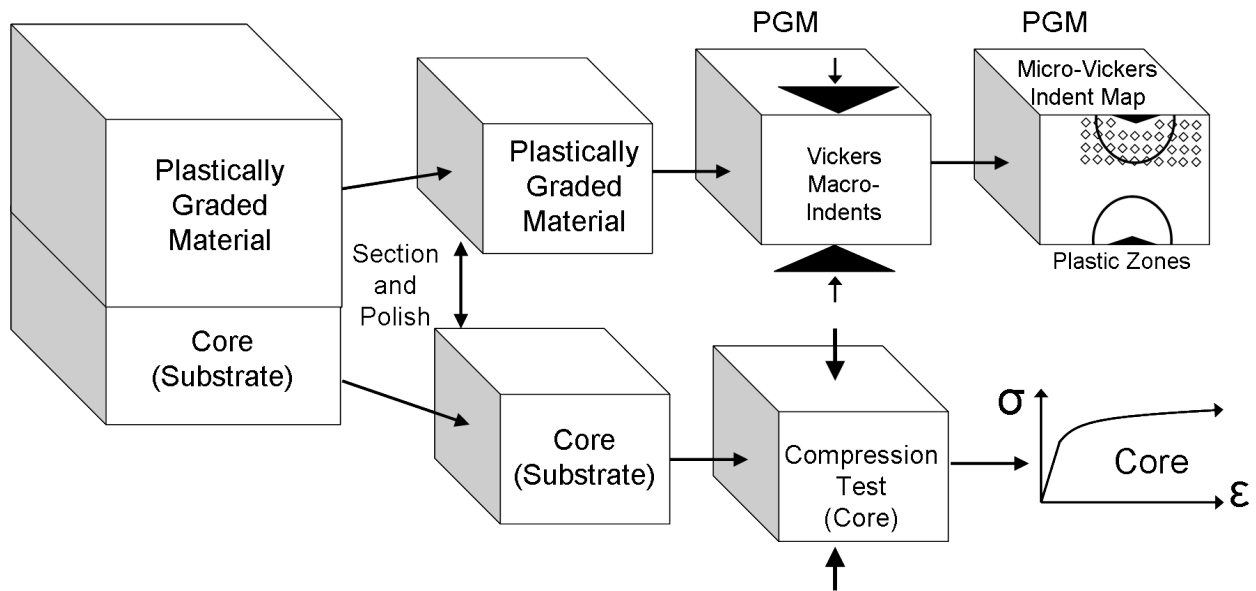


Figure 5-3. Core region provides lower bound of possible plastic material behavior. PGM is plastically deformed by macro-Vickers indentations. The resulting increase in hardness (and yield strength) is measured by micro-Vickers indentations.

It will be shown that the resulting plastic zone from this macro-indent was not deep enough to plastically deform the entire graded material and therefore an essentially new PGM was created by removing the soft core region and polishing up to the graded region with new surface hardness of 500 Hv (Figures 5-2 and 5-3) in the direction of increasing hardness, (i.e. soft to hard). These two PGMs will be used to demonstrate the validity of the proposed method for determining the plastic response of a PGM with both increasing and decreasing gradients in hardness and allow for most of the case hardened region to be plastically deformed.

The macro-Vickers indents (Figure 5-2) were sectioned and polished up to the indent diagonals (Figure 5-5) which correspond to the maximum indent and plastic zone depths. Standard metallographic polishing procedures were used to prevent residual stress accumulation and additional plastic deformation induced by polishing (ASM Handbook, 2009). Micro-Vickers indents were then conducted on these cross-sections at 200 grams indent load and 100 μm spacing to measure the increase in hardness within the plastic zone of the macro-Vickers indent. The micro-Vickers indents of the cross sections of the hardest and softest macro-indents are shown in Figure 5-5A and 5-5B, respectively.

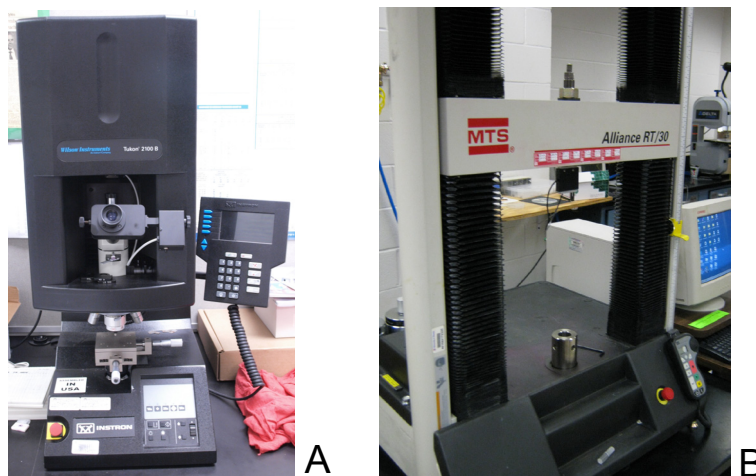


Figure 5-4. (A) Wilson® Instruments Tukon™ 2100 B Vickers indenter and (B) MTS® Alliance™ RT/30 machine.

The variation in hardness can be seen visually in Figure 5-5 where the micro-indent sizes change along the cross-section. Because the indent load is the same for all micro-indents, the hardest regions have smaller indent sizes when compared to the softest regions. This method of micro-indent mapping below a macro indent is similar to the approaches adopted by (Koeppel et al., 1999; Srikant et al., 2006; Chaudhri, 1998), but will be extended here to predict the variation in flow curves of a PGM.

The macro-Vickers indentation on the hardest PGM surface (Figure 5-5A) was created by an indent load of 330 Kg which resulted in an average diagonal length of 800 μm . The increase in micro-Vickers hardness along the centerline of the plastic zone is depicted in Figure 5-6A. The maximum increase in hardness is approximately 50 Hv in the region of highest plastic strain and it decreases to the virgin hardness value at the plastic zone boundary.

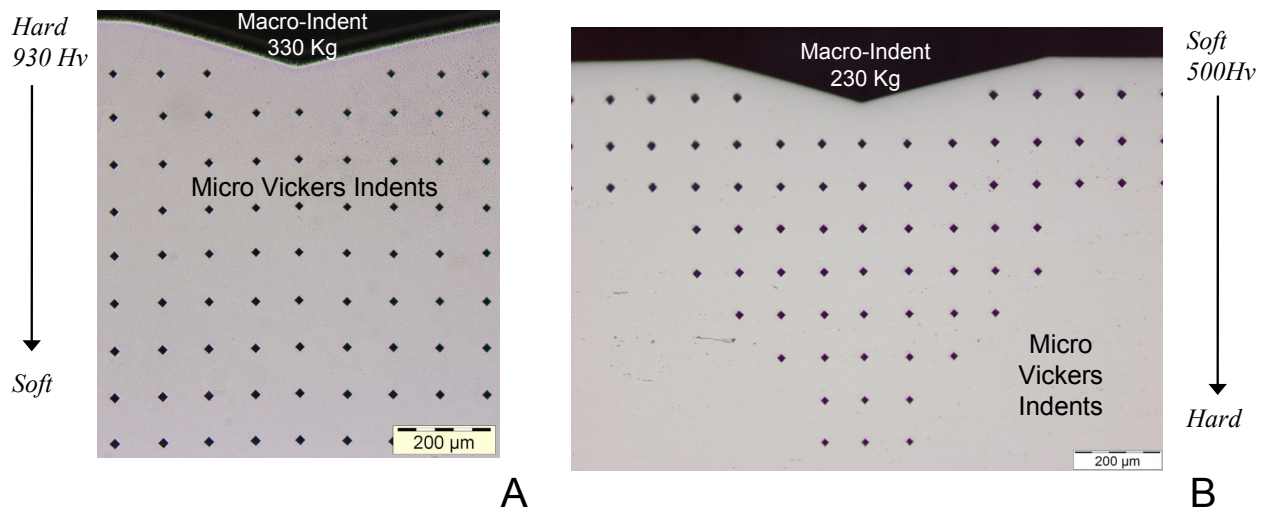


Figure 5-5. Micro-Vickers indent (200 g) map within plastic zone induced by the macro-Vickers indentation on (A) the hardest and (B) softest surfaces of the PGMs. Notice smaller micro-indent sizes within the hardest region. Macro and micro Vickers indents performed by M.A. Klecka.

If this region had a perfectly plastic response with depth, there would have been no strain hardening, no increase in flow stress, and consequently no increase in hardness within the plastic zone of the macro-indent. Thus the increase in hardness within the plastic zone is dependent on material strain hardening properties and the magnitude of plastic strain. The increase in hardness along the centerlines of the macro-indent's plastic zones is shown because this region has the deepest plastic zone depth which includes the gradient in plastic response. Also, the hardness

measurements along the centerline correspond to the highest plastic strain (and flow stress) experienced at any specific depth from the surface.

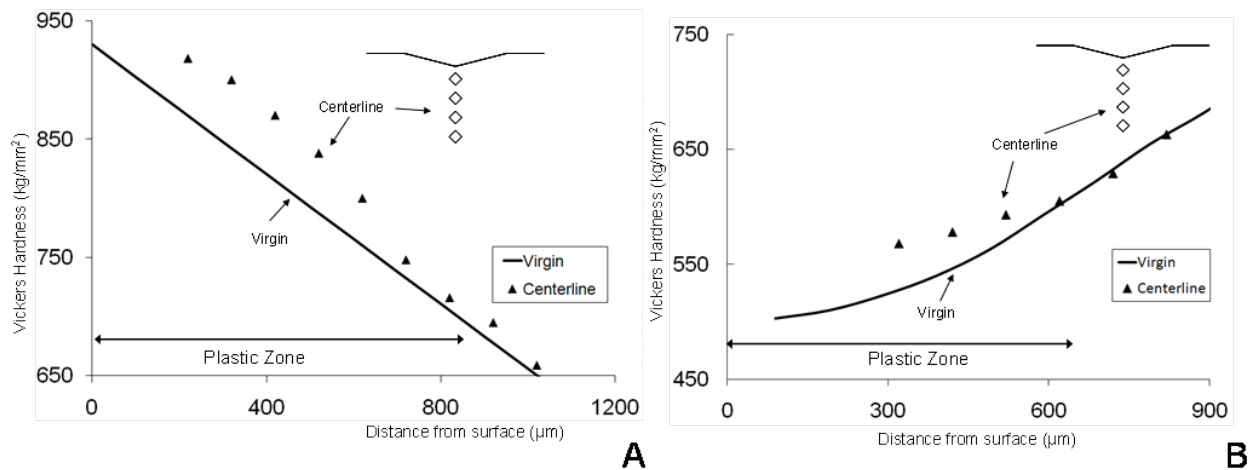


Figure 5-6. Experimentally measured micro-Vickers hardness along the centerline of the macro indent for (A) hardest and (B) softest PGMs. Micro Vickers indents performed by M.A. Klecka.

A similar procedure was conducted on the softest PGM surface that has an increasing subsurface hardness trend with depth (Figure 5-5B). The macro-indent on the softest surface (500 Hv) was conducted at a reduced load of 230 Kg but resulted in a larger indent diagonal of 940µm. Similarly, the increase in hardness along the centerline of the plastic zone is shown in Figure 5-6B. The maximum increase in hardness is again approximately 50 Hv in the region of large plastic strain and decreases to zero at the elastic-plastic boundary.

The increase in hardness within the plastic zones of both PGMs is indicative of the material's ability to strain-harden. The question yet to be answered, however, is what equivalent plastic strain magnitude corresponds to the above measured hardness (flow stress) values? To answer this question, these macro-Vickers indentation experiments of graded materials are simulated in finite element models. The flow curve variation with depth will be estimated from the flow curve of the core region and the variation in

hardness with depth within the PGM. The measured increase in micro hardness within the plastic zone of the macro-indent will be estimated from the equivalent plastic strain calculated by the FE model.

Constitutive Response

Determining the constitutive response of any given point within the PGM using traditional methods such as a tension and compression test is impractical because of the difficulty in preparing a specimen of uniform composition that corresponds to any given point within the PGM. However, the core region has uniform microstructure and hardness (Figure 5-2), and the ample amount of core material available allows for a compression test specimen of 10 mm x 6 mm x 3.175 mm to be extracted.

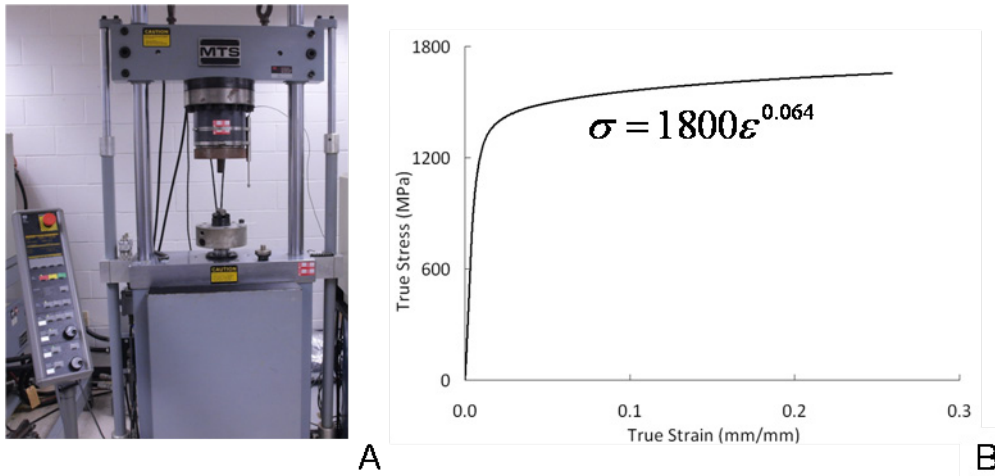


Figure 5-7. (A) MTS load frame is used to determine (B) flow curve obtained from compression test of the homogeneous core. Compression test performed by M.A. Klecka.

The compression test was conducted in a MTS load frame (Figure 5-7A). The power-law curve fit, $\sigma = K\epsilon^n$, applied to the flow curve obtained from this compression test shown in Figure 5-7B resulted in a strength coefficient $K = 1800$ MPa and a strain hardening exponent $n = 0.064$. Because this is the softest region of the PGM, this information provides a lower bound of possible plastic behavior for the entire PGM.

The plastic behavior of the core region is known from the compression test of Figure 5-7B, thus there can be 3 possible trends in strain hardening exponent, n , with depth (Figure 5-8) throughout the rest of the PGM. All trends in n must all converge to the core value. The variable n could be zero at the surface and increase to that of the core region, constant throughout, or have a higher value at the surface and decrease to that of the core. Since an increase in hardness was observed in the hardest PGM, n must be nonzero in this hardest region. Both constant n with depth and a linear decrease in n with depth will be shown here when comparing predicted and measured hardness values. Because the increase in hardness was approximately constant within the plastically deformed PGMs, it is reasonable to assume that the value for n remains constant throughout the PGM. This assumption will be later validated by the mechanistic approach presented here which is based on well established concepts such as representative plastic strain (Jayaraman et al., 1998) and constraint factor (Gao et al., 2006).

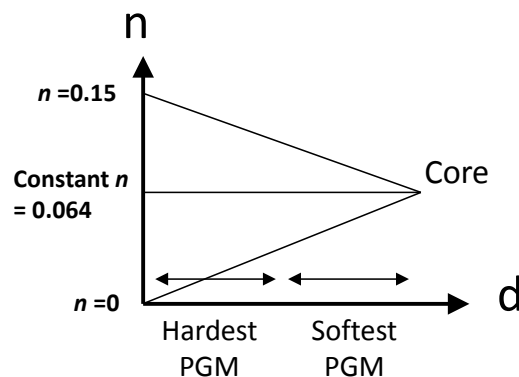


Figure 5-8. Possible trends in strain hardening exponent, n , must converge to core value as this is the lower bound of possible plastic behavior.

In order to convert the micro-hardness measurements of Figure 5-5 and 5-6 to local flow stress values as shown schematically in Figure 5-1, the amount of local strain hardening induced by the micro indent must be taken into account. This is done

through the concept of representative plastic strain, ϵ_r , which is a measure of the average or “representative” plastic strain induced by a Vickers indent and discussed in more detail in Chapter 4. The representative plastic strain describes the extent that the average flow stress within the plastic zone exceeds the initial yield strength of the indented material.

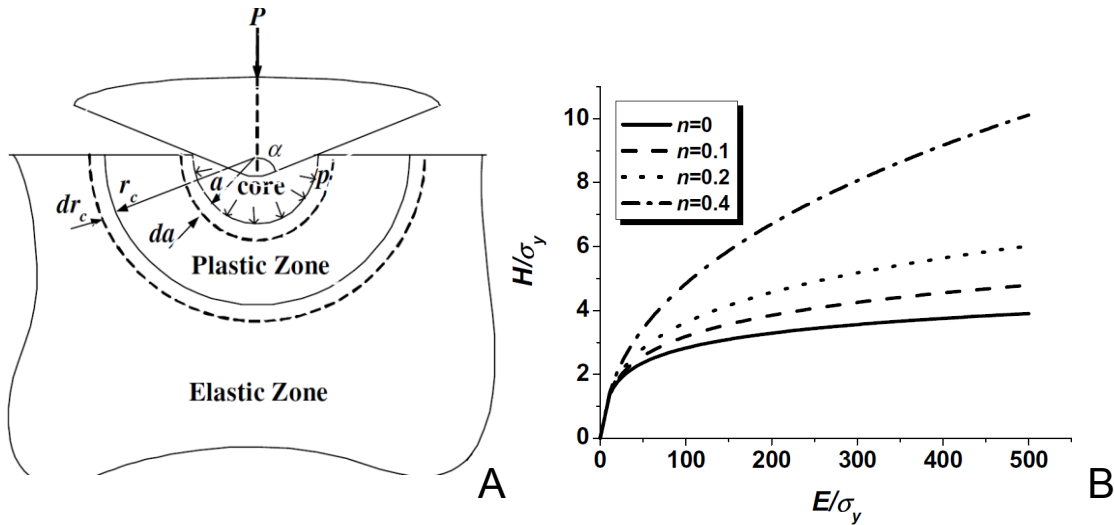


Figure 5-9. (A) Expanding cavity model for strain hardening materials assumes hemispherical deformation below tip of indent. (B) Resulting relationship between H/σ_y and E/σ_y . (Gao et al., 2006).

Calculated values for this average or representative plastic strain as a function of n can be found in (Jayaraman et al., 1998) and will not be repeated here. For $n = 0.064$ of the core region, $\epsilon_r = 0.052$ and its corresponding representative flow stress is 1506 MPa

which has a constraint factor given by $C = \frac{H}{\sigma(\epsilon_r)} = 2.82$. Recall that ϵ_r is a function of n

only (Jayaraman et al., 1998), and therefore the value for representative plastic strain is also constant regardless of the location within the PGM because n is assumed to be constant throughout. The flow stress at the corresponding representative plastic strain

defines one point on the material flow curve, $\sigma(\varepsilon_r) = \frac{H}{C}$ provided the values of C and H (Figure 5-2) are known a priori.

The relationship between hardness, yield strength, elastic modulus, and strain hardening exponent for power-law hardening materials was derived by Gao et al. (2006) using expanding cavity models in the following form:

$$\frac{H}{\sigma_y} = \frac{2}{3} \left\{ \left(1 - \frac{1}{n} \right) + \left(\frac{3}{4} + \frac{1}{n} \right) \left(\frac{1}{3} \frac{E}{\sigma_y} \cot \alpha \right)^n \right\} \quad (5.1)$$

where α is the equivalent half cone angle for Vickers indenters and has a value of 70.3 degrees. A visual representation of the dependence of $\frac{H}{\sigma_y}$ on $\frac{E}{\sigma_y}$ from this expanding

cavity model is shown in Figure 5-9b. Note for low values of n, $\frac{H}{\sigma_y}$ is approximately 3

which agrees with the predictions of Tabor (1970). The expanding cavity models of (Johnson, 1970; Hirst and Howse, 1969; Marsh, 1964) are based on the solution by Hill (1950) for the quasi-static expansion of an internally pressurized spherical shell of perfectly plastic materials (Gao et al., 2006).

The expanding cavity model assumes that the deformation beneath Vickers indentation is hemispherical in nature and the plastic deformation is caused by a small “core” of large hydrostatic stress beneath the tip of the indent as shown in Figure 5-9A. For strain hardening materials, the stress-displacement equations for an internally pressurized spherical shell were derived by Gao and Wei (1991) and extended by Gao et al. (2006) to create the ECM used in this analysis. For indentation, the hardness of the material is taken to be the mean pressure acting on the interface between the

hydrostatic core and the plastic zone and compares well to the hardness predicted by experiments and finite element analysis Gao et al. (2006).

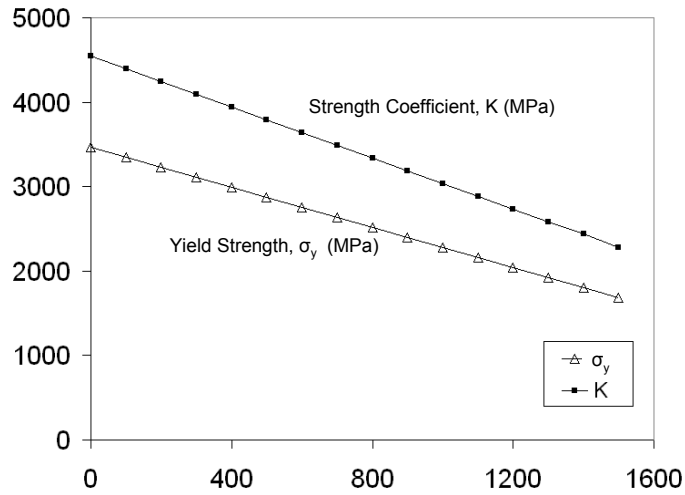


Figure 5-10. Strength coefficient K and Yield strength as function of depth.

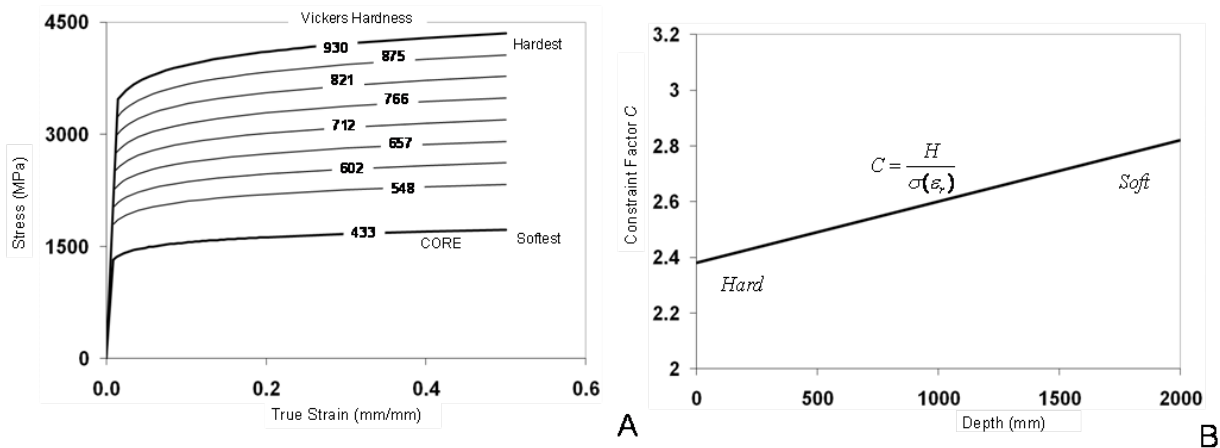


Figure 5-11. (A) Power-law flow curves as function of hardness and (B) ratio of hardness to flow stress at the corresponding representative plastic strain.

Because H and n are known for all depths, and assuming that $E=200$ GPa for steel, the yield strength σ_y can then be determined from the above relationship for the entire PGM from this equation and shown in Figure 5-10. The strength coefficient K as function of hardness (H) taken can now be calculated $K = E^n \sigma_y^{1-n}$ from the intersection of the elastic $\sigma_y = E \epsilon_y$ and plastic $\sigma_y = K \epsilon_y^n$ stress-strain curves which vary with depth

for a PGM. The resulting flow curves as a function of hardness is shown in Figure 5-

11A. The constraint factor $C = \frac{H}{\sigma(\epsilon_r)}$ can now be calculated and shown in Figure 5-

11B. This data will be used to predict the Vickers hardness for a plastically deformed PGM using the equivalent plastic strain calculated by FE models described in the following section.

Finite Element Model

To determine if these flow curves accurately represent the plastic behavior of the PGM, the plastic strain induced by the macro-indent must be determined and then related to the micro-Vickers hardness measurements discussed earlier. The plastic strain is dependent on the material's ability to resist plastic deformation, i.e. its strain hardening characteristics and yield strength. Determination of the plastic strain magnitude and gradient with depth beneath a Vickers indent is difficult, particularly for a PGM, thus finite element modeling provides a convenient way to compute the plastic strain gradient beneath these macro-indentations.

In this axisymmetric model, a rigid conical indenter with a half cone angle of 70.3 degrees produces the same indentation area as a Vickers indent for any given indent depth and does not require a mesh (Figure 5-12). The indenter is displacement controlled to the same depth as in the experiment and then retracted to its original position. The indenter is given fixed rotational boundary conditions and allowed to translate normal to the specimen surface. Four thousand eight hundred four-node bilinear quadrilateral axisymmetric elements make up the Finite Element (FE) model with the finest mesh in the region closest to the indenter tip. The FE model is implemented in ABAQUS 6.7-1. The plastic response is governed by the von Mises

(J2) yield criterion, associated flow rule, and isotropic hardening. The flow curve variation of Figure 5-11A is inserted into the finite element model and the macro-indentations of both hardest (Figure 5-5A) and softest (Figure 5-5B) PGMs are simulated to the same macro-indentation depths as the experiments.

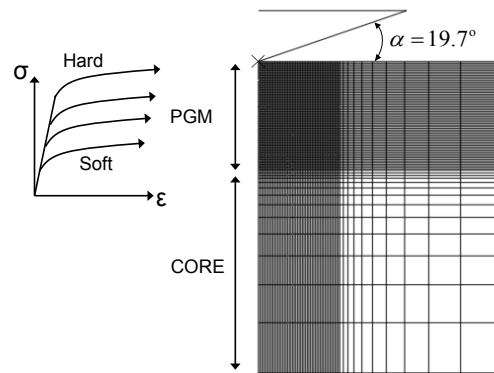


Figure 5-12. FE model of the macro-Vickers indentation of a PGM.

Results

The contours of constant equivalent plastic strain within the plastic zones as calculated by the FE models of both PGMs are shown in Figure 5-13A. Note that the indentation on the hardest PGM surface has a shallower macro-indent depth ($d=118 \mu\text{m}$ at 330Kg indent load) than the deeper macro-indent and lower indent load (230 Kg) on the softest PGM surface ($d=130 \mu\text{m}$). However, the plastic zone for the hardest PGM is deeper and narrower than the plastic zone of the softest PGM. The surface of the hardest PGM is more resistant to plastic deformation and therefore forces plastic deformation to occur within the weaker, subsurface region.

Although the softest PGM surface has a deeper macro-indent, it has a shallower and wider plastic zone because the softest-surface region accommodates most of the plastic deformation while the subsurface regions are harder and more resistant to plastic deformation. These results show that distribution of plastic strain is sensitive to

the gradation in plastic response. The equivalent plastic strains along the centerlines of both PGMs increase asymptotically as shown in Figure 5-13B. This information will be used to predict the micro-Vickers hardness measurements of Figure 5-6.

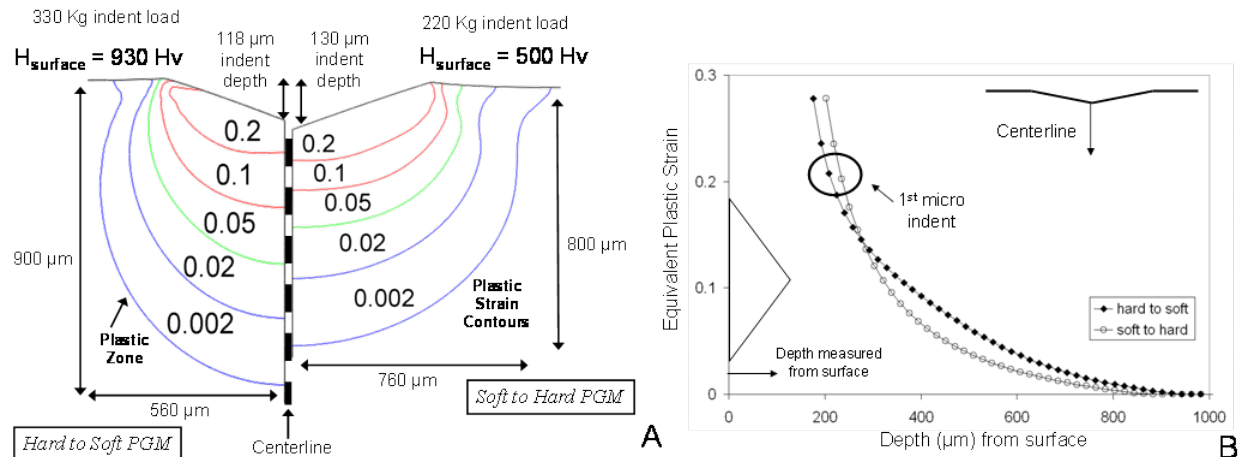


Figure 5-13. (A) Equivalent plastic strain contours within the plastic zones induced by Vickers macro-indents on hardest and softest surfaces of the PGMs. (B) Comparison of the plastic strain magnitudes along centerlines of both PGMs as measured from material surface.

The predicted micro-Vickers hardness at a given location j at any depth within the PGM plastic zone can now be determined by the equation: $H = C\sigma(\varepsilon_r + \varepsilon_p)$ where ε_p^j is the initial plastic strain induced by the macro-Vickers indent (Figures 5-13A and 5-13B) and ε_r^j is the representative plastic strain induced by the micro-Vickers indent at a given location. For the case where n is a constant 0.064 with depth, $\varepsilon_r^j = 0.052$ is constant with depth also. The flow stress that corresponds to the sum total of the representative plastic strain and equivalent plastic strain is calculated for every point within the plastic zone and then multiplied by C to predict the micro-Vickers hardness values. These hardness values are then compared to the experimentally measured hardness in Figure 5-6 and shown again in Figure 5-14. Good agreement is seen between the predicted and measured hardness values along the centerlines of both macro indents. The

predicted versus measured Vickers hardness for the entire plastic zone is shown in Figures 5-15A and 5-15B for both hardest and softest PGMs, and a good agreement is observed there also.

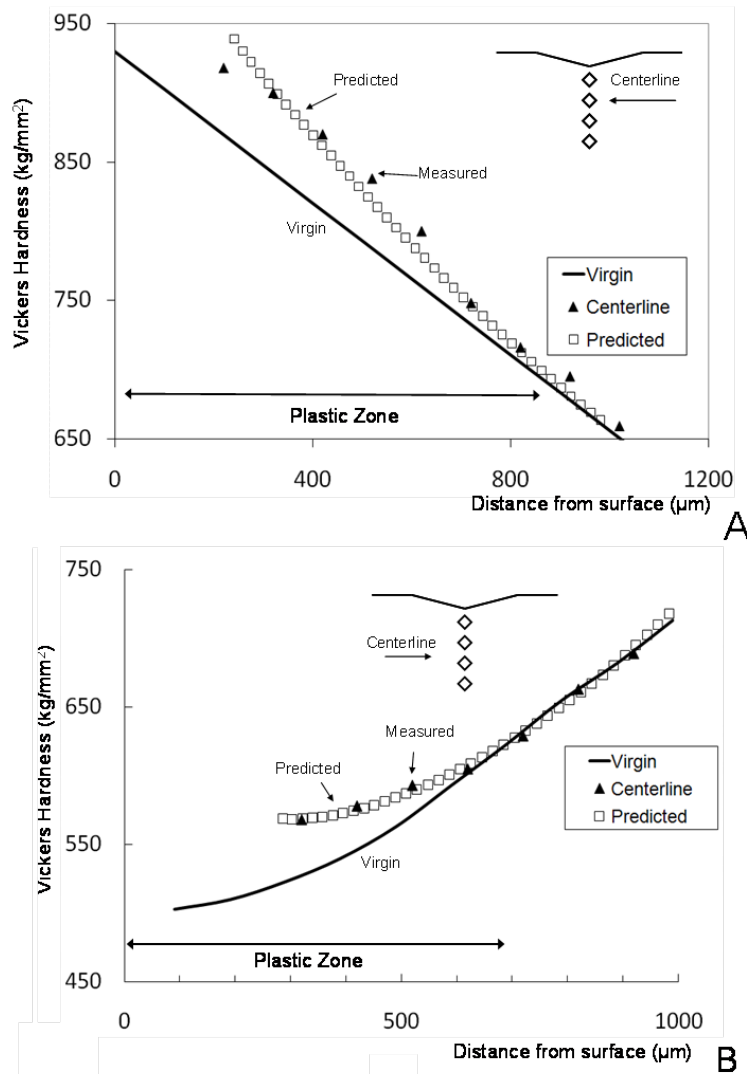


Figure 5-14. Predicted versus measured micro-Vickers hardness values along the plastic zone's centerline for both (A) hardest and (B) softest PGMs.

The plastic zone sizes in these graphs are estimated by where the hardness contours merge with the virgin hardness at a given depth. Any discrepancy in the calculated plastic zone depth by the FE model is due to the sensitivity of the method in

predicting hardness at low plastic strain, experimental scatter in measured hardness, and the fact that the plastic zone boundary is defined at the 0.002 plastic strain contour.

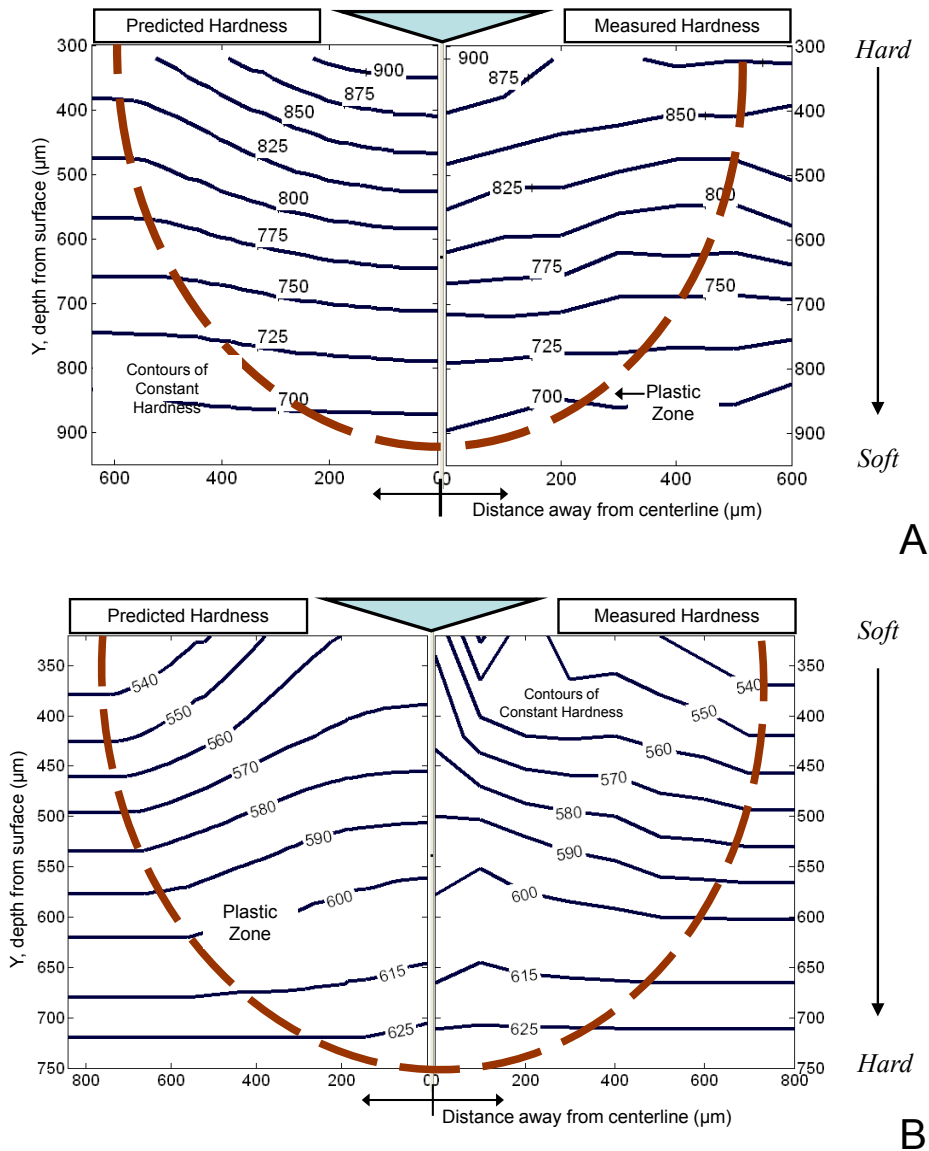


Figure 5-15. Predicted versus measured micro-Vickers hardness values for the (A) hardest and (B) softest PGMs within the entire plastic zone of the macro-Vickers indentations.

The predicted hardness is expected to have an increasing trend as it approaches the indenter tip because the flow stresses of the power-law plastic response increase with increasing plastic strain and the plastic strain asymptotically increases close to the

indenter tip as observed in Figure 5-13B. Note that there is good agreement between the measured and predicted hardness values for both PGMs irrespective of the increasing or decreasing hardness gradients below the surface. This validates the assumption of constant strain hardening exponent with depth for this specific case-hardened stainless steel.

Since the graded layer gradually merges with the core material, the assumption of constant strain hardening exponent for the PGM is logical. It will be shown next that a different set of flow curves predicts different micro-Vickers hardness values within the plastic zone of the macro-Vickers indent for the same macro-indent depths. Although the PGM used in this analysis has a constant strain hardening exponent, this method can be applied to PGMs that have variations in n as well because the expanding cavity model derived by Gao et al. (2006) takes into account the dependence of hardness on n . This will be seen in Chapter 6 where the variation in plastic response is determined for case hardened M50 NiL, where the flow curve of the core region is initially unknown.

Variation in Strain Hardening Exponent

To show an example of how a different variation in plastic response can predict different hardness values, a new trend in strain hardening exponent is created and a new set of material properties will be inserted into the same FE indentation-models as before. The new strain hardening exponent at the hardest surface of the PGM will be assumed as $n = 0.15$ and will decrease linearly to the core where $n = 0.064$ (Figures 5-8 and 5-16). Once again, the strain hardening exponent of the core cannot be changed because it was determined from the compression test of the core region. The representative plastic strain ε_p is dependent only on the strain hardening exponent so

ε_r is now 0.035 at the hardest region where $n = 0.15$ and increases linearly to 0.052 for $n = 0.064$ at the softest region (Figure 5-17). To find $\varepsilon_r(n)$ one may refer to the calculations by Jayaraman et al. (1998) or calculate individually for each n value through FE simulations of the Vickers indentation process shown in Chapter 4.

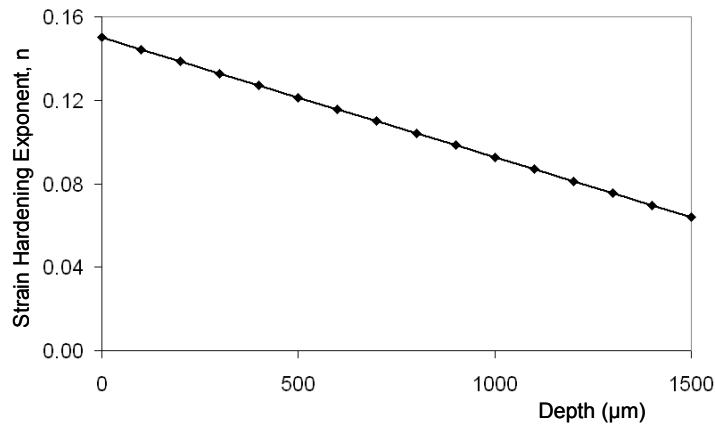


Figure 5-16. New trend in strain hardening exponent (n) is created to determine how material properties affect predicted hardness values.

The yield strength and strength coefficient K are determined as before using the expanding cavity model of Gao et al. (2006) and shown in Figure 5-18A. The new set of flow curves as a function of hardness is shown in Figure 5-18B. Note that the virgin hardness trend is unchanged and this new variation in flow curves still yields the same virgin hardness as the constant- n trend used before. However, for a given amount of plastic deformation the increase in hardness will not be the same for different strain hardening materials.

The core material's strain hardening exponent cannot be changed which means the new set of material properties will not deviate much from the initial set (constant- n) in this softest region. Therefore, the softest PGM FE model does not need to be simulated again. These new flow curves are inserted into the indentation-FE model of

the hardest region of the PGM because this is where the greatest deviation from the initial set of material properties occurs.

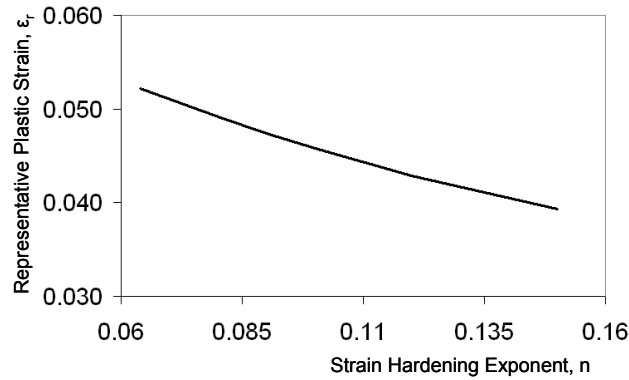


Figure 5-17. Representative plastic strain as function of strain hardening exponent, n . Calculations can be found in (Jayaraman et al., 1998) and Chapter 4.

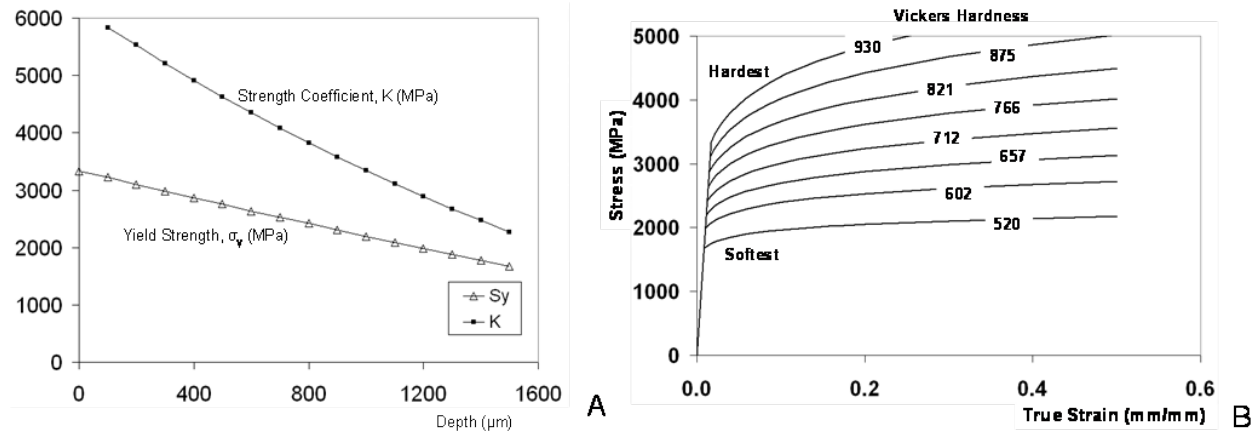


Figure 5-18. (A) New trends in σ_y , K , and n allow for (B) new flow curves to be created as function of hardness (depth of PGM). Note material properties of core material cannot change because K and n of core were determined by compression test and provide lower bound of possible plastic behavior.

The macro-indent of the hardest PGM is simulated again with the new material properties to the same depth as before and the equivalent plastic strain gradient is calculated by the FE model. The depth-dependent representative strain is added to the equivalent plastic strain at every point of interest and then converted to predicted-hardness values while taking into account the variation in both K and n using the same relationship between indentation hardness and flow stress, $H = C\sigma(\epsilon_r + \epsilon_p)$. The new

predicted hardness values are plotted against the measured hardness from Figure 5-14 and shown again in Figure 5-19. As shown, the new predicted hardness values do not match the experimentally measured ones when the strain hardening exponent of the hardest region is effectively doubled as compared to the initial test case. For completeness, the virgin hardness as predicted by the same equation $H = C\sigma(\varepsilon_r + \varepsilon_p)$ when $\varepsilon_p \rightarrow 0$ [i.e. $H = C\sigma(\varepsilon_r)$] also displays a good match to the virgin hardness trend, thus verifying that these flow curves still predict the same virgin hardness.

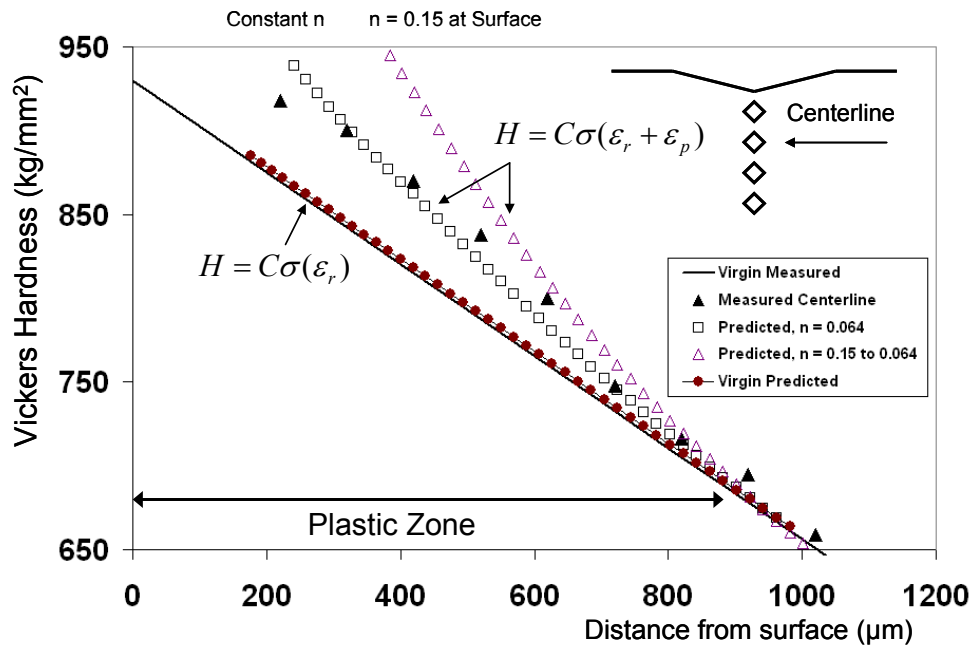


Figure 5-19. Predicted versus measured indentation hardness values for two different sets of material properties. Constant n with depth matches well, but variation in n from 0.15 at the surface to 0.064 at the core over-predicts hardness in plastic zone of hardest PGM.

Key Points

The results of this analysis is currently under peer review for publication at the International Journal of Plasticity and the key points of which are outlined here:

- The proposed method predicts the experimentally measured increase in indentation hardness of a plastically deformed PGM with respect to its virgin

(undeformed) state, and in the process, extracts the stress-strain response of the graded material as a function of depth.

- This method utilizes proven concepts regarding representative plastic strain, constraint factor, and the micro-indentation mapping of a plastically deformed region which are combined to convert the measured Vickers hardness values to flow stresses that must fall on the flow curve at a specified depth within the deformed PGM.
- As shown, this procedure is applicable irrespective of an increasing or decreasing hardness trend and convenient in the sense that it does not require instrumented indentation devices or curve fitting of many complex dimensionless functions.
- The relative depth and width of the plastic zone from macro Vickers indentation is indicative of whether the hardness gradient is increasing or decreasing with depth. The PGM used in this analysis was determined to have a linear variation in yield strength and hardness, but a constant strain hardening exponent.
- The two sets of flow curves used in this analysis have different trends in strain hardening exponent, but still satisfy the virgin hardness criteria of Gao et al. (2006). A unique variation in flow curve is determined when the virgin hardness criterion of Gao et al. (2006) is satisfied, and the increase in measured hardness within a zone of plastic deformation is correctly predicted.

CHAPTER 6 REVERSE ANALYSIS

Nongraded Materials

As discussed in Chapters 4 and 5, the relationship between hardness and yield strength has been given considerable attention since the time of (Tabor, 1970) as seen by the numerous methods and applications for determining material properties.

Hardness measurements are relatively easy to perform, can be used multiple times on a single specimen, and prevent the time-consuming tasks of creating tensile or compression test specimens to obtain the desired yield strength of a material. Chapter 4 discussed concepts regarding the hardness of a material increases with plastic strain and can be related to the increased yield strength (flow stress) of the plastically deformed material. Those concepts were then applied in Chapter 5 to determine the plastic response of graded materials when the plastic response of the core region was known a priori.

Some materials such as plastically graded materials, coatings, and thin films are difficult to procure traditional tensile or compression test specimens to obtain its stress-strain curve to a desired amount of plastic strain. However, the material properties of these materials must be known to contribute to the engineering design process for their specific purpose. Thus new methods that are inexpensive and easy to perform are needed to extract the flow curve of these types of materials. The process of using indentation hardness measurements to determine the stress-strain response of a material is called a reverse analysis. The opposite case, where an increase in hardness with plastic strain can be predicted when the flow curve of the material is known, is called a forward analysis and much easier to perform as shown in Chapter 4.

Quite a few reverse analyses have been proposed since (Tabor, 1970) and many of them depend on instrumented indentation methods. Instrumented indentation essentially relates the load-displacement curve of a sharp or blunt indentation to the material properties of the indented material such as elastic modulus, strain hardening exponent, and yield strength.

The highly referenced paper by Dao et al. (2001) created a new set of dimensionless functions that relate the elastic and plastic material properties to instrumented indentation data; namely the loading curvature and unloading curve and the ratio of the elastic rebound depth to the maximum indentation depth. These three parameters were shown to be indicative of yield strength, elastic modulus, and strain hardening exponent, and their relationships allowed both forward and reverse analyses to be performed based on the experimental and numerical indentation loading curves for a large range of material properties.

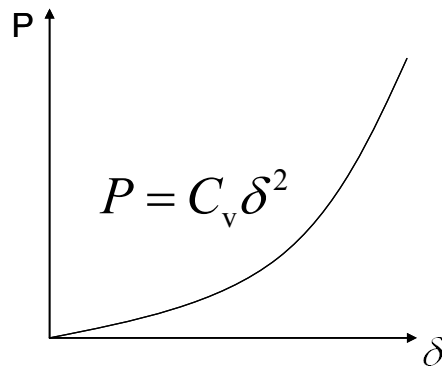


Figure 6-1. Schematic of instrumented indentation loading.

Bucaille et al. (2003) extended the method of Dao et al. (2001) to four different conical indenters to increase the accuracy of the reverse analysis and showed that friction has no significant influence on indentation measurements for cone angles greater than 60°. Chollacoop et al. (2003) showed that a dual-indenter analysis

improves the uniqueness and sensitivity of the forward and reverse analyses for instrumented indentation.

Later, the single-indenter reverse analyses by Tho et al. (2005) and Antunes et al. (2007) determined a unique solution of material properties using instrumented indentation provided the elastic modulus is known a priori. There are some downsides to the instrumented indentation method such as imperfections of the indent tip which can affect measurements at low loads, determining the “zero point” or initial contact of the indenter, taking into account the compliance of the frame, and “pile-up” or “sink-in” which affect indentation depth measurements Fischer-Cripps (2006). It has been shown that different flow curves can produce the same indentation response (Tho et al., 2005; Chollacoop et al., 2003). Also the actual plastic deformation beneath a Vickers indent is not being investigated in these methods.

The method presented here does not require instrumented indentation devices and will forgo the cumbersome process of creating dimensionless functions. It will use the actual hardness measurements of a plastically deformed material to determine its flow curve while knowing only the virgin hardness of the material and its elastic modulus. This method will utilize the expanding cavity model derived by Gao et al. (2006) which determined the relationship between virgin hardness, strain hardening exponent, elastic modulus, and yield strength for strain hardening materials. The plastic strains that correspond to a given flow stress (and hardness) will be determined by finite element modeling described later.

To induce a gradient in plastic strain, macro Vickers indents are chosen due to their availability and ease of use. The plastic deformation that exists within the plastic

zone of a Vickers indent on a ductile material allows large plastic strains to develop without the onset of cracking due to the confinement of the surrounding material and the large compressive hydrostatic stresses that exist in this region. This being so, the material is allowed to strain harden to relatively large flow stresses without failure. The resulting increase in yield strength can be captured by micro-Vickers indentation hardness measurements on this plastically deformed region which is described next.

Experimental

The core region of commercially available Pyrowear 675 (P675) stainless steel was used in this analysis. It has an elastic modulus of approximately 180 GPa and virgin hardness of 433 Hv. In order to obtain a gradient in plastic strain, a macro Vickers indent was performed on the surface of the specimen at 204 Kg indentation load and an average diagonal length of 935 μ m. The resulting hardness is 433 Hv and similar to that of the micro Vickers hardness values performed later, thus there is very little indentation size effect (ISE) for this material and indent load range.

The macro Vickers indent was sectioned and polished to the indent diagonals which correspond to the maximum indent and plastic zone depth. Standard metallographic polishing procedures were used to prevent the residual stress accumulation and additional plastic deformation induced by polishing (ASM Handbook, 2009).

Micro Vickers indentations were then performed along the centerline of this macro indent's plastic zone to measure the increase in hardness as shown in Figure 6-2. The centerline is chosen because this is the deepest region of the plastic zone caused by the macro indent and maximizes the number of data points obtained by the micro

Vickers indents which are limited by their spacing. The locations of these indents are also convenient when comparing to FE models.

Macro Vickers Indent

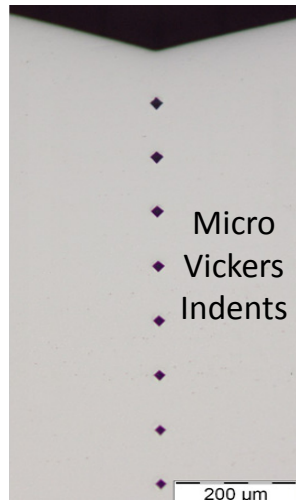


Figure 6-2. Micro-Vickers indents along centerline of cross section of macro-Vickers indent. Macro and micro Vickers indents performed by M.A. Klecka.

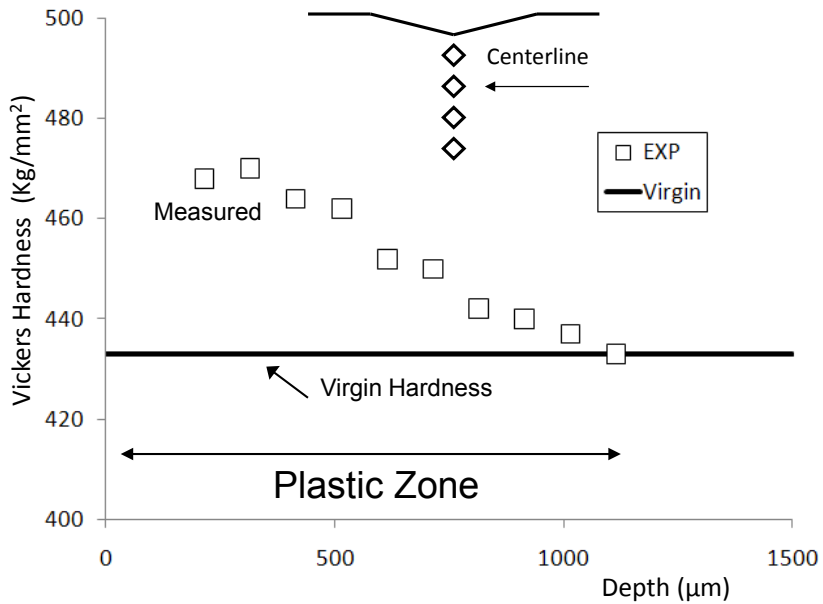


Figure 6-3. Measured Vickers hardness within plastic zone of macro-Vickers indent

The micro Vickers indentations were performed at 200 g indent load and were spaced 100 μm apart to prevent interactions with neighboring indents as per ASTM

E384 standard. Since this is a ductile steel material, the plastic strain is well contained within the plastic zone, thus no cracks emanate from the corners of the indents and affect neighboring indents.

The micro Vickers indentations were simulated in FE models in Chapter 4 and showed that the plastic zones were sufficiently small enough to prevent interactions with neighboring indents. The measured increase in hardness along the centerline is plotted in Figure 6-3 with respect to its virgin hardness of 433 Hv.

The highest hardness value is 215 μm from the surface and has a value of 470 Hv. Note the increase in hardness within the plastic zone is due to the strain hardening of the material that occurs from plastic deformation. The highest increase in hardness is in the same region as the highest plastic strain magnitude, both of which decrease as they approach the elastic-plastic zone boundary.

The centerline of the plastic zone has the largest usable plastic strain gradient and the location of which is easy to identify when comparing to finite element models. It is possible to perform the same micro Vickers indentation process on a different type of plastically deformed region that was induced by compression, tension, torsion, or bending, but Vickers indentation is chosen due to its large gradient in plastic strain in a relatively small and manageable volume.

Analysis

The challenge now is to determine the flow curve of this material from the virgin hardness, elastic modulus, and increase in hardness within a region of plastic deformation. The expanding cavity model for strain hardening materials developed by Gao et al. (2006) determined the relationship between hardness, yield strength, strain

hardening exponent, and elastic modulus for Vickers indentation. Their equation is reproduced here:

$$\frac{H}{\sigma_y} = \frac{2}{3} \left\{ \left(1 - \frac{1}{n} \right) + \left(\frac{3}{4} + \frac{1}{n} \right) \left(\frac{1}{3} \frac{E}{\sigma_y} \cot \alpha \right)^n \right\} \quad (6.1)$$

and a visual representation of the dependence of $\frac{H}{\sigma_y}$ on $\frac{E}{\sigma_y}$ from this expanding cavity

model is shown in Figure 6-4B. For a low value of n , $\frac{H}{\sigma_y}$ is approximately 3 which

agrees with Tabor (1970).

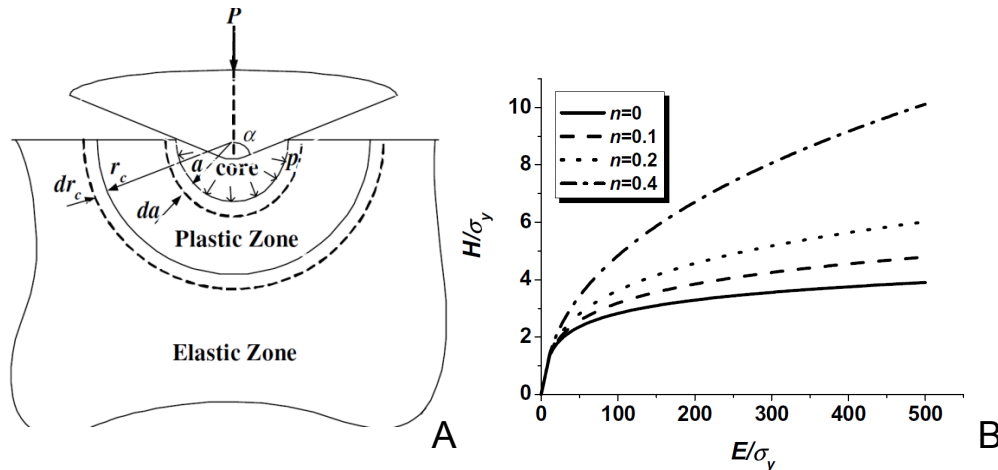


Figure 6-4. (A) Expanding cavity model for strain hardening materials assumes hemispherical deformation below tip of indent. (B) Resulting relationship between H/σ_y and E/σ_y . (Gao et al., 2006).

As discussed in Chapter 5, the expanding cavity models of (Johnson, 1970; Hirst and Howse, 1969; Marsh, 1964) are based on the solution by Hill (1950) for the quasi-static expansion of an internally pressurized spherical shell of perfectly plastic materials. The expanding cavity model assumes that the deformation beneath Vickers indentation is hemispherical in nature and the plastic deformation is caused by a small “core” of large hydrostatic stress beneath the tip of the indent as shown in Figure 6-4A. For

strain hardening materials, the stress-displacement equations for an internally pressurized spherical shell were derived by Gao and Wei (1991) and extended by Gao et al. (2006) to create the ECM used in this analysis. For indentation, the hardness of the material is taken to be the mean pressure acting on the interface between the hydrostatic core and the plastic zone and shows good agreement with experimental and numerical hardness data Gao et al. (2006).

Table 6-1. For $E = 180 \text{ GPa}$ and $H = 433 \text{ kg/mm}^2$, the values for K , σ_y , C , and ϵ_r can be calculated for a variation in n . K and σ_y are in MPa.

n	K	σ_y	$H/\sigma(\epsilon_r)$	ϵ_r
0.00	1423	1423	2.88	0.067
0.03	1566	1352	2.85	0.057
0.07	1778	1256	2.82	0.051
0.13	2154	1112	2.87	0.043
0.20	2691	941	2.94	0.035

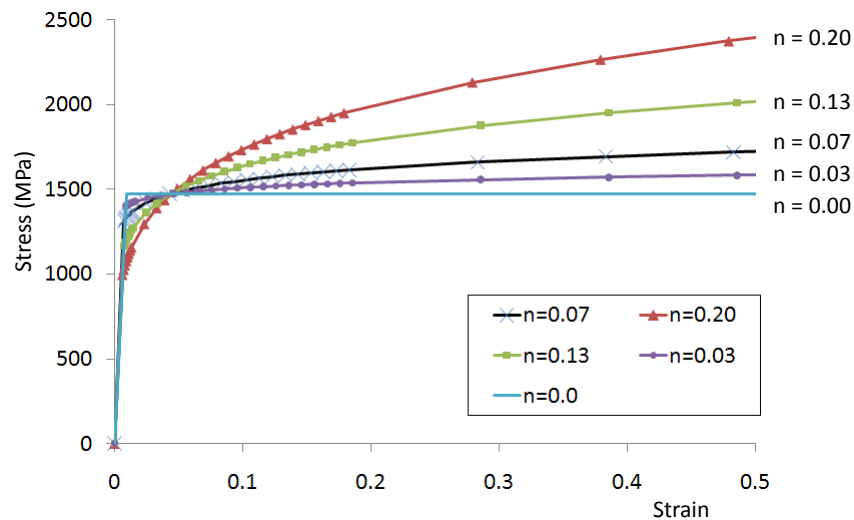


Figure 6-5. Flow curves all have same elastic modulus and virgin hardness. An increase in n must decrease σ_y to preserve same virgin hardness values.

If the elastic modulus and virgin hardness are known for a given material, then various values of n can be iterated, and the resulting yield strength can be calculated from this relationship. This allows one to create a set of stress-strain curves that have

the same virgin hardness and elastic modulus, but different yield strengths and strain hardening exponents. Thus for an unknown material, a given range of values of $n = 0.0, 0.03, 0.07, 0.13, \text{ and } 0.20$ along with a virgin hardness of $H = 433 \text{ Hv}$ and $E = 180 \text{ GPa}$ can be used to determine the corresponding yield strength using Eq. (6.1) and shown in Table 6-1 as a function of n . The strength coefficient K can then be determined from $K = E^n \sigma_y^{1-n}$ and the resulting flow curves are shown in Figure 6-5.

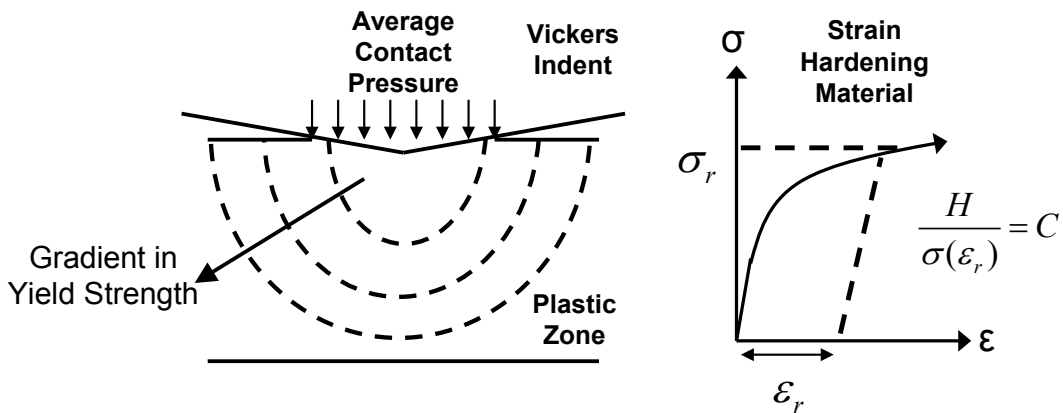


Figure 6-6. Gradient in yield strength within plastic zone affects measured contact pressure and allows the flow curve variation in Figure 6-5 to all have the same virgin hardness.

Note that the elastic modulus and virgin hardness are the same for all flow curves and that only yield strength and strain hardening exponent are changing. A strain hardening material with lower yield strength can have the same virgin hardness as a material with a greater yield strength and comparatively lower strain hardening characteristics. For a strain hardening material, a gradient in plastic strain and yield strength exists within the plastic zone of a Vickers indent which increases the contact pressure of the Vickers indentation to what would also be measured for a relatively perfectly plastic material that has higher yield strength (Figure 6-6).

The macro-Vickers indentations of these different materials are simulated in the same FE model described in Chapter 4 and reproduced here in Figure 6-7. In this axisymmetric model, a rigid conical indenter with a half cone angle of 70.3 degrees produces the same indentation area as a Vickers indent for any given indent depth and does not require a mesh. The indenter is displacement controlled to the same depth as in the experiment and then retracted to an unloaded position. The indenter is given fixed rotational boundary conditions and allowed to translate normal to the specimen surface. Four thousand eight hundred four-node bilinear quadrilateral axisymmetric elements make up the Finite Element (FE) model with the finest mesh in the region closest to the indenter tip. The FE model is implemented in ABAQUS 6.7-1 and the plastic response is governed by the von Mises (J2) yield criterion, associated flow rule, and isotropic hardening.

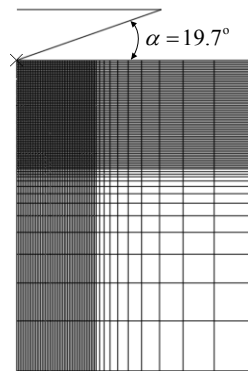


Figure 6-7. FE model of the macro-Vickers indentation.

Results

Each flow curve of Figure 6-5 is inserted into its own finite element model and the macro-indentations are simulated to the same macro-indentation depths as the experiments since this was the known method of plastic deformation. Note the load-displacement curve of the indentation process is the same for all the materials since the

virgin hardness is the same for each and independent of indentation depth as shown in Figure 6-8. Similar load displacement curves as the one shown here were used in the previously mentioned methods to determine the material properties of the indented materials. This information is not necessary for this analysis, but only shown here to demonstrate that different flow curves can produce the same indentation loading curve because the virgin hardness is independent of depth and the same for the material test cases shown here.

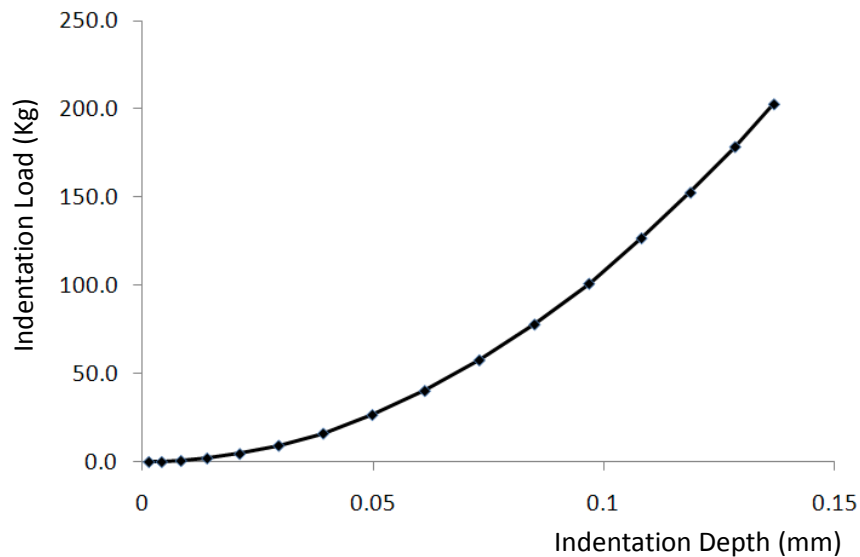


Figure 6-8. Load displacement curve from FE model is the same for all flow curves since virgin hardness is same for all and hardness is independent of indent depth.

The plastic strains below the indent tip and along the centerlines of the plastic zones of all material test cases are calculated by the FE model and shown in Figure 6-9. Note they are all similar in magnitude and distribution with minor variations between them. This is to be expected since the gradient in flow stress within the plastic zone will not be the same for the different strain hardening materials.

The modified Tabor's rule that was introduced in Chapter 4 is then repeated for each flow curve via $H = C\sigma(\varepsilon_r + \varepsilon_p)$ in order to predict the increase in hardness within the plastic zone of each material where ε_r is the representative plastic strain induced by the micro-Vickers indentation process, ε_p is the equivalent plastic strain at a specific point within the gradient (Figure 6-9), and C is the Constraint factor, $C = \frac{H}{\sigma(\varepsilon_r)}$.

The representative strain used in this analysis is the average volumetric plastic strain induced by Vickers indentation that was shown to be dependent only on the strain hardening exponent by Jayaraman et al. (1998). The representative plastic strain takes into account the additional strain hardening due to the plastic deformation of the micro-indentation process itself.

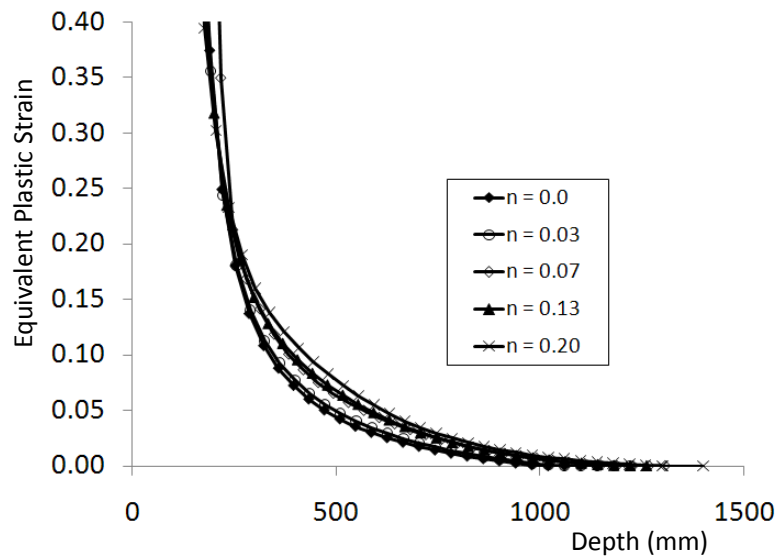


Figure 6-9. Plastic strain gradient along centerline of plastic zone for all material test cases.

Values for the average plastic strain induced by a Vickers indent are shown in Figure 6-10 and taken from Jayaraman et al. (1998). This average plastic strain was

shown to be a valid representative plastic strain in Chapter 4. Calculated values of the constraint factor C for each of the flow curves are shown in Table 6-1.

The predicted increase in hardness within the plastic zone of the Vickers indent of each material is then calculated from $H = C\sigma(\varepsilon_r + \varepsilon_p)$ for each n value as shown in Figure 6-11. If the indented material had one of the specific flow curves shown in Figure 6-5, these results predict the experimentally measured hardness values for each. All hardness trends converge to the same virgin hardness outside of the plastic zone where $\varepsilon_p = 0$. Thus when the predicted and measured hardness values match, a unique flow curve is then determined.

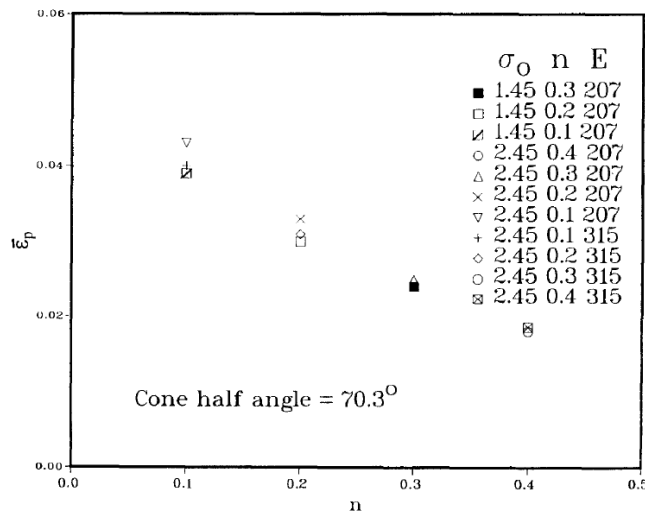


Figure 6-10. Average volumetric plastic strain induced by Vickers indent is function of n only as shown by Jayaraman et al. (1998).

The flow curve corresponding to $n = 0.07$ predicts the closest hardness values when compared to what was experimentally measured out of the test cases that were performed here. Note for $n = 0$, there can be no increase in flow stress or hardness for any amount of plastic strain because the material is perfectly plastic. As n increases,

the change in hardness also increases for a given amount of plastic strain, the distributions of which were shown to be similar for all materials in Figure 6-9.

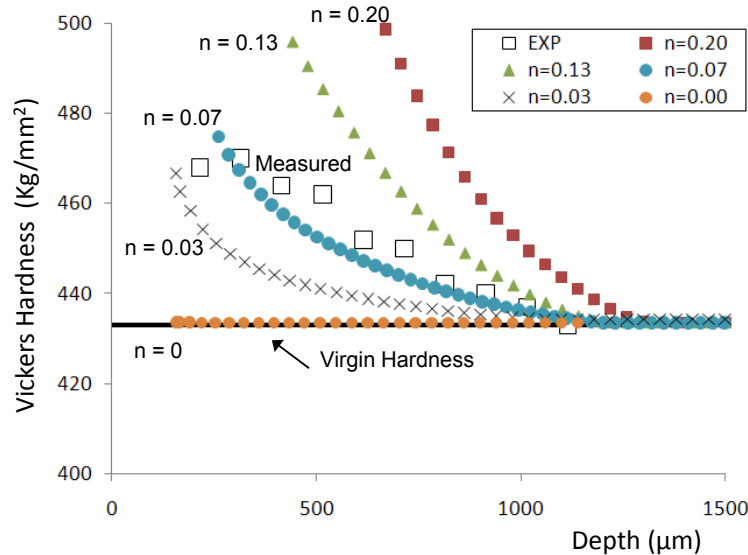


Figure 6-11. Predicted hardness values within plastic zone of macro-Vickers indents. Note all converge to virgin hardness value, but different values for n lead to different increases in hardness for the same macro indent depth.

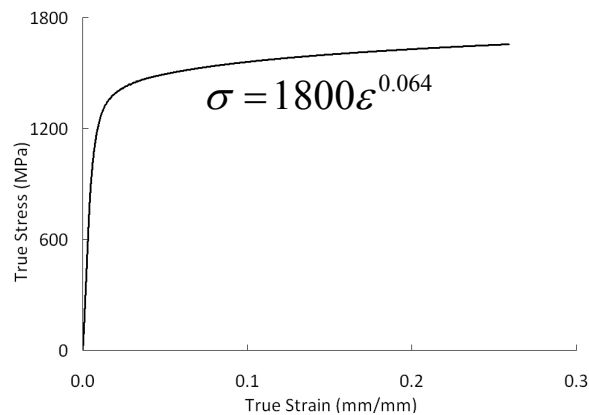


Figure 6-12. Compression test of P675 core region results in power law curve fit with strength coefficient $K = 1800$ MPa and strain hardening exponent $n = 0.064$ and close to what the method predicted. Compression test performed by M.A. Klecka.

To check the validity of this method, a compression test was performed on the core region of the P675 stainless steel. The ample amount of core material available allows for a compression test specimen of 10 mm x 6 mm x 3.175 mm to be extracted.

The compression test was conducted in a MTS load frame up to a failure strain of 0.27.

The power-law curve fit, $\sigma = K\varepsilon^n$, applied to the flow curve obtained from this compression test shown in Figure 6-12 resulted in a strength coefficient $K = 1800$ MPa and a strain hardening exponent $n = 0.064$ which is close to the $K = 1778$ and $n = 0.07$ that was predicted by the method.

Key Points

The results of this analysis have been submitted for peer review for publication in Acta Materialia and the key points of which are summarized here:

- A reverse analysis that predicts the flow behavior of a material based on indentation hardness measurements was presented that utilizes the well established procedures of expanding cavity models, Tabor's rule of converting hardness to flow stress for a given amount of plastic deformation, and representative plastic strain of the indentation process.
- A unique solution for yield strength and strain hardening exponent is determined when the predicted and measured hardness values match over a plastically deformed region. It is unique in the sense that the values for n and σ_y must satisfy the virgin hardness relationship derived by Gao et al. (2006) and match the experimentally-measured increase in hardness in a plastically deformed region.
- The problems with uniqueness of single-indenter reverse analyses that relied on instrumented indentation devices were often solved when the elastic modulus of the indented material was known a priori (Tho et al., 2005; Antunes et al., 2007). This is similar to this analysis where the elastic modulus must be known in order to determine the yield strength and strain hardening exponent from the ECM of Gao et al. (2006). This method is not limited to analyzing the deformation induced by Vickers indentation, but can be used for any plastically deformed region provided the plastic strain magnitude and distribution can be determined by finite element modeling.
- These findings will be used to determine the plastic response of case hardened M50 NiL in the next section of this Chapter which is needed for the spall edge impact analysis of Chapter 7.

Reverse Analysis Graded Materials

The reverse analysis for non-graded materials can be applied to graded materials as well. In this analysis the graded material properties of case hardened M50 NiL will

be determined without knowing the core material properties a priori. Thus, the lower bound of possible plastic behavior is initially unknown. The method presented here will prevent the laborious task of extracting and preparing a tensile test specimen of the core or substrate region. A similar indentation method to that used in Chapter 5 for P675 steel is repeated here for M50NiL steel without the compression test of the core region. The plastic response of M50NiL is needed to repeat the ball-spall edge impact study in Chapter 7 using its specific gradient in plastic response to determine its affect on the magnitude or distribution of residual tensile stress and plastic strain and consequently spall propagation rate.

Experimental

Commercially available, case hardened M50 NiL is the PGM used in this analysis. The M50 NiL samples were extracted from disks donated by AFRL that were originally intended for ball-on-disk wear testing. Specimens were sectioned, ground, and polished on surfaces parallel to the carbon gradient. Standard metallographic polishing procedures which use progressively finer polishing media were used to minimize damage and residual stresses induced by polishing (ASM Handbook, 2009).

Micro Vickers-indentations were conducted on this cross-section using a Wilson® Instruments (Tukon™ 2100B) Vickers indenter at 200g indent loads for 15 seconds loading duration. The indents were spaced 2.5 times the indent diagonal to prevent interactions with neighboring indents as per ASTM E384 standard. This was similar to the indentation procedures used in Chapters 4 and 5. The Vickers hardness profile in Figure 6-13 for the virgin M50 NiL steel displays a nonlinear trend in virgin hardness that varies from 820 Hv at the surface to 455 Hv over a depth of 2.5 mm. Note that the surface hardness is lower than that of P675 steel (930 Hv) as shown in Chapter 5;

however, the virgin hardness trend is now nonlinear as opposed to the linear virgin hardness gradient of P675 steel.

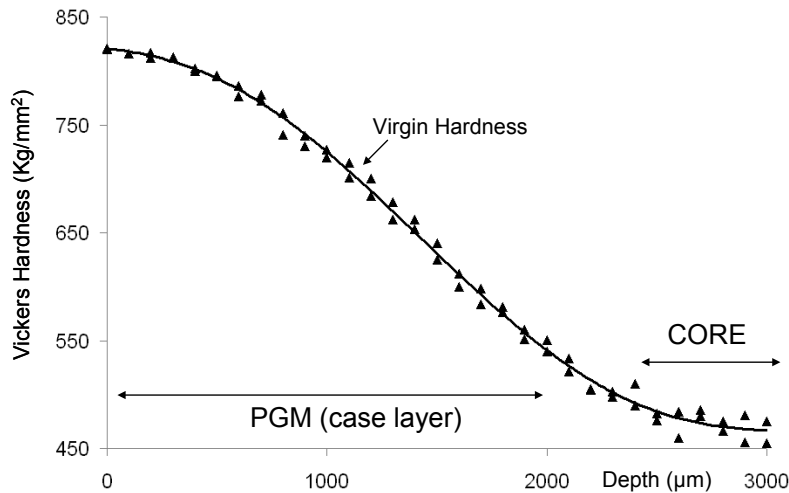


Figure 6-13. Virgin hardness profile for M50NiL. Micro Vickers indents performed by M.A. Klecka.

To induce a large magnitude and gradient in plastic strain within the graded material, a macro-Vickers indent was performed at 300 Kg indent load using a standard Vickers indenter. The indenter was fixed in a custom housing and mounted in a Universal Testing Machine load frame (MTS Alliance™ RT/30) and driven in load control for 15 seconds. The macro-Vickers indent was conducted in the direction of decreasing hardness, (i.e. hard to soft).

This macro-Vickers indent was sectioned and polished up to the indent diagonals which correspond to the maximum indent and plastic zone depths. Standard metallographic polishing procedures were used to prevent residual stress accumulation and additional plastic deformation induced by polishing (ASM Handbook, 2009). Micro-Vickers indents were then conducted along the centerline of this cross-section at 200 grams indent load and 100 µm spacing to measure the increase in hardness within the

plastic zone of the macro-Vickers indent. The resulting increase in hardness along the plastic zone's centerline is shown in Figure 6-14.

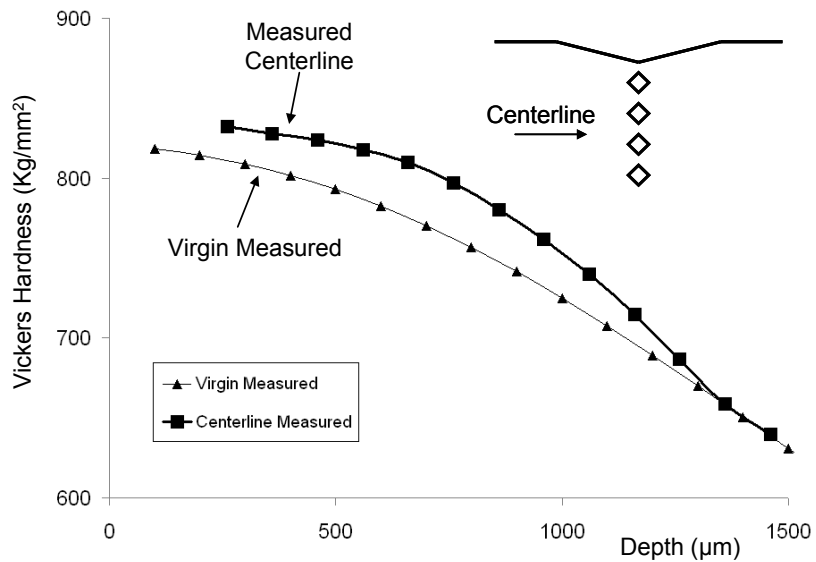


Figure 6-14. Measured increase in Vickers hardness along centerline of plastic zone of M50 NiL. Macro and micro Vickers indents performed by M.A. Klecka.

An increase in hardness within the plastic zone is indicative of the material's capacity to strain harden. The increase in hardness in the region of highest plastic strain is approximately 30 Hv for M50 NiL whereas the P675 steel displayed an increase in hardness of approximately 50 Hv in the similar region, which may or may not indicate lower strain hardening capabilities.

Variation in Flow Curve

In Chapter 5, the plastic response of the core region was known initially which allowed for logical trends in strain hardening exponent to be iterated and then tested for accuracy (Figure 6-15A). For M50NiL, a similar process will be repeated, but the lower bound of plastic response is unknown initially which increases the number of iterations to determine a solution for the variation of n with depth (Figure 6-15B).

The method presented here will combine the concepts of Chapters 4, 5, and the reverse analysis of Chapter 6 to determine the plastic response of case hardened M50NiL. Since the virgin hardness gradient with depth is known (Figure 6-13) and the elastic modulus is assumed to be a constant $E=200$ GPa with depth, logical variations in strain hardening exponent n can be iterated (Figure 6-15B), and the resulting yield strength σ_y and strength coefficient K can be determined from the expanding cavity model derived by Gao et al. (2006) which is discussed in more detail in Chapter 5 and earlier in this Chapter.

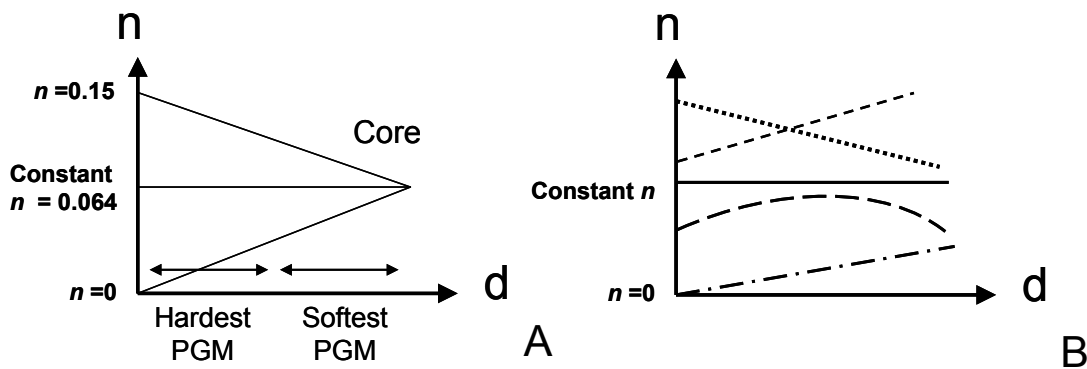


Figure 6-15. (A) For P675 in Chapter 5, all logical trends in n must converge to core value. (B) For M50NiL, there is no upper or lower bound on n , thus increasing the number of iterations to determine a solution for n .

Knowing K , n , and E , with depth allows a flow curve variation with depth to be constructed that represents a specific virgin hardness profile. It was shown earlier in this Chapter that the expanding cavity model of Gao et al. (2006) allows a set of flow curves to be created that have a different values for n and σ_y , but the same virgin hardness. A similar concept is applied here, except now various gradients in flow curves all yield the same gradient in virgin hardness. The strain hardening characteristics will be identified by how well the predicted hardness values match what

was actually measured in a region of plastic deformation as was similarly done by the reverse analysis for nongraded materials earlier in this Chapter.

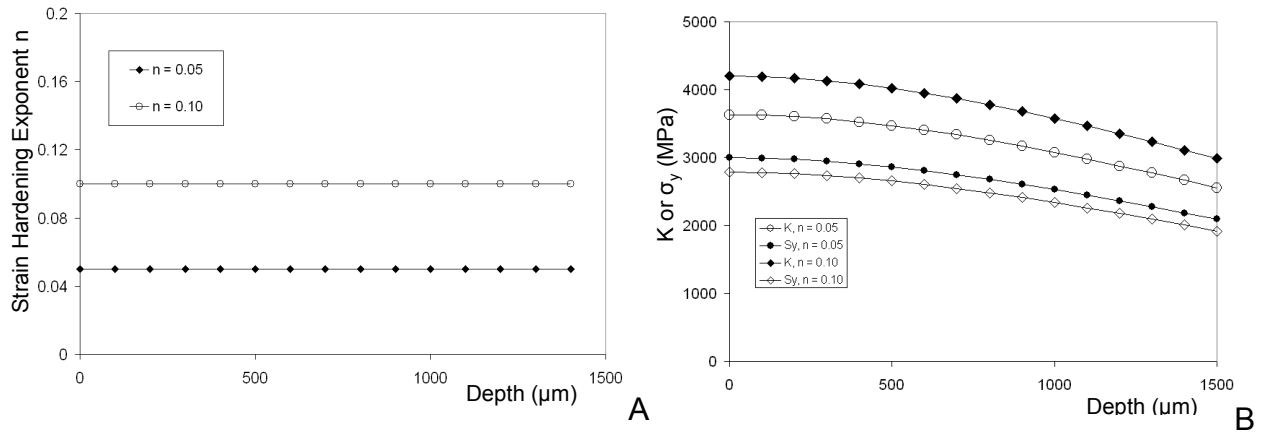


Figure 6-16. (A) Constant strain hardening exponent with depth as two initial test cases. (B) Resulting yield strength and strength coefficient as functions of depth and determined by ECM of Gao et al. (2006).

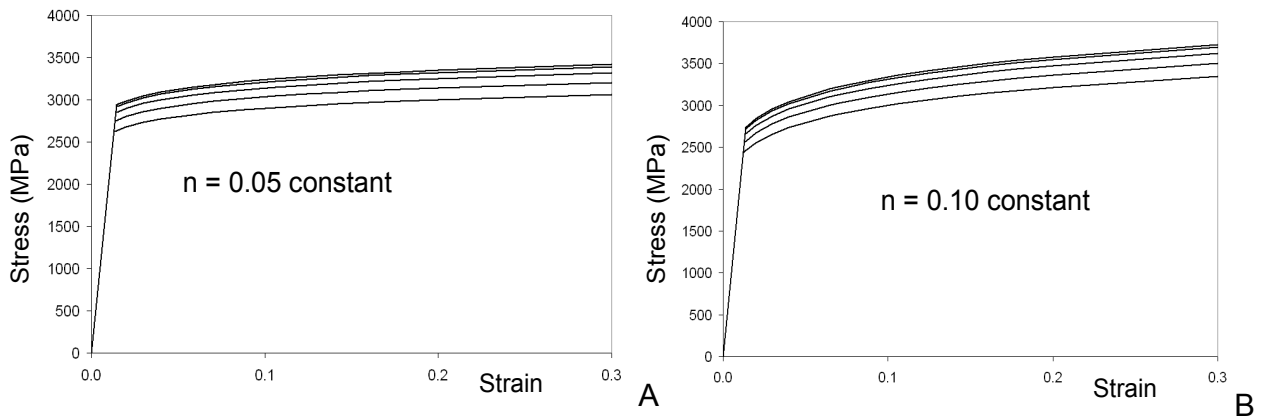


Figure 6-17. Flow curve variation for M50 NiL virgin hardness trend when (A) $n = 0.05$ and (B) $n = 0.10$. The flow curves shown correspond to the following depths, 0 (surface), 200, 400, 600, and 800 μm . The surface flow curve has the highest value for yield strength and strength coefficient, and decreases with depth.

As a first step, two test cases of constant $n = 0.05$ and $n = 0.10$ with depth is assumed since a similar trend provided adequate results for P675 steel of Chapter 5 and shown in Figure 6-16A for M50NiL. The expanding cavity model (ECM) determined the relationship between hardness, yield strength, elastic modulus, and strain hardening exponent by equation 6.1 is then used to determine the resulting yield strength and

strength coefficient as a function of depth (Figure 6-16B). Note that for $n = 0.10$, the yield strength is lower than the $n = 0.05$ test case, and is indicative of the same trends seen earlier in this chapter for nongraded materials, where higher values for n need lower values for yield strength in order to preserve the same virgin hardness.

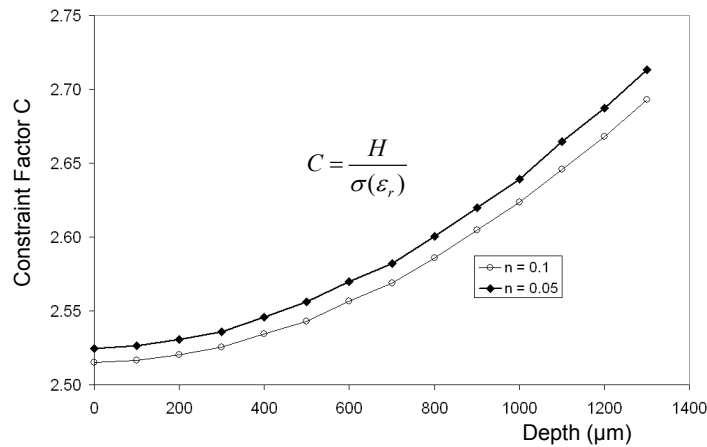


Figure 6-18. Constraint factor C as function of depth for $n = 0.05$ and $n = 0.10$ trends with depth.

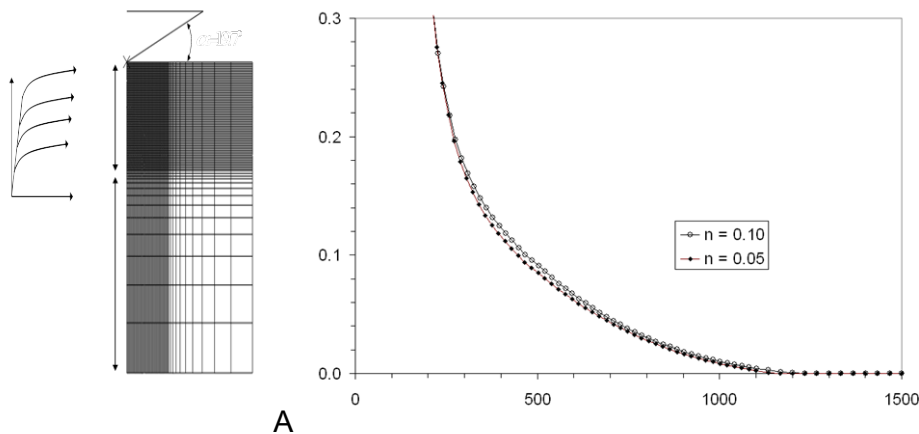


Figure 6-19. (A) Finite element model of macro indentation of M50 NiL, and (B) equivalent plastic strain gradient along plastic zone's centerline.

The resulting flow curve variation is shown in Figures 6-17A and 6-17B for both $n = 0.05$ and $n = 0.10$, respectively. The flow curves at depths of 0, 200, 400, 600, and 800 μm from the surface are shown. The values for constraint factor $C = \frac{H}{\sigma(\epsilon_r)}$ can now

be determined and shown graphically in Figure 6-18. Calculated values for

representative plastic strain ϵ_r as function of strain hardening exponent were shown in Chapters 4 and 5.

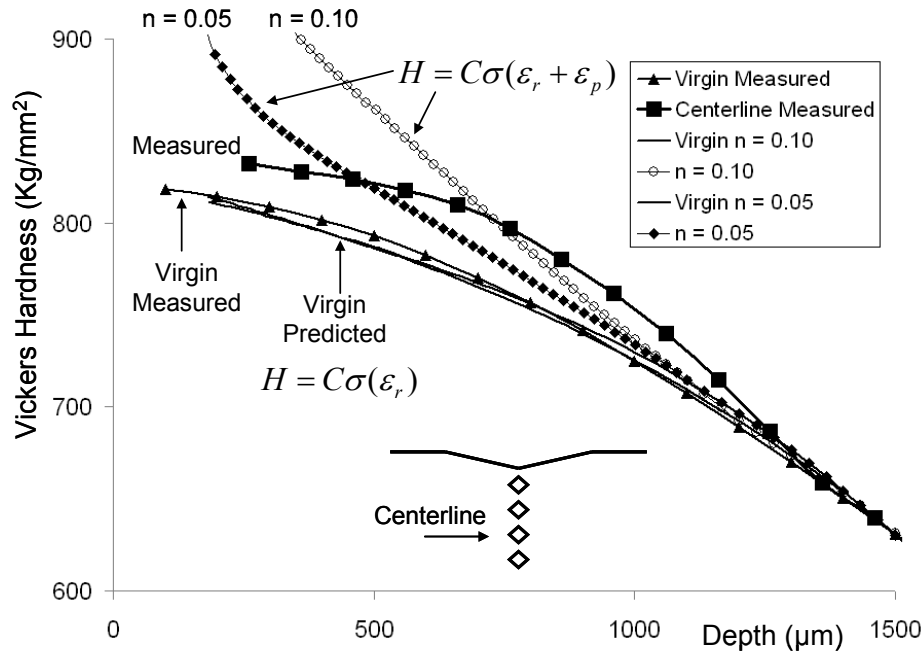


Figure 6-20. Constant trends in strain hardening exponent do not provide adequate match to measured hardness values.

The flow curve variation is inserted into the same finite element model used in Chapter 5 (shown again in Figure 6-19A) and the macro indentation process is simulated for the same indent depth as was used for M50 NiL. The finite element model calculates the equivalent plastic strain gradient along the centerline (Figure 6-19B) which will be used to predict the corresponding increase in hardness for each flow curve that varies with depth.

The increase in hardness within the plastic zone of the macro Vickers indent is predicted through the relationship, $H = C\sigma(\epsilon_r + \epsilon_p)$, where C is the constraint factor, ϵ_r is the representative plastic strain (Chapter 4), and ϵ_p is the equivalent plastic strain at a specific point within the plastic zone (Figure 6-19B). The predicted hardness values can

now be compared to the measured hardness values of Figure 6-14 and shown again in Figure 6-20.

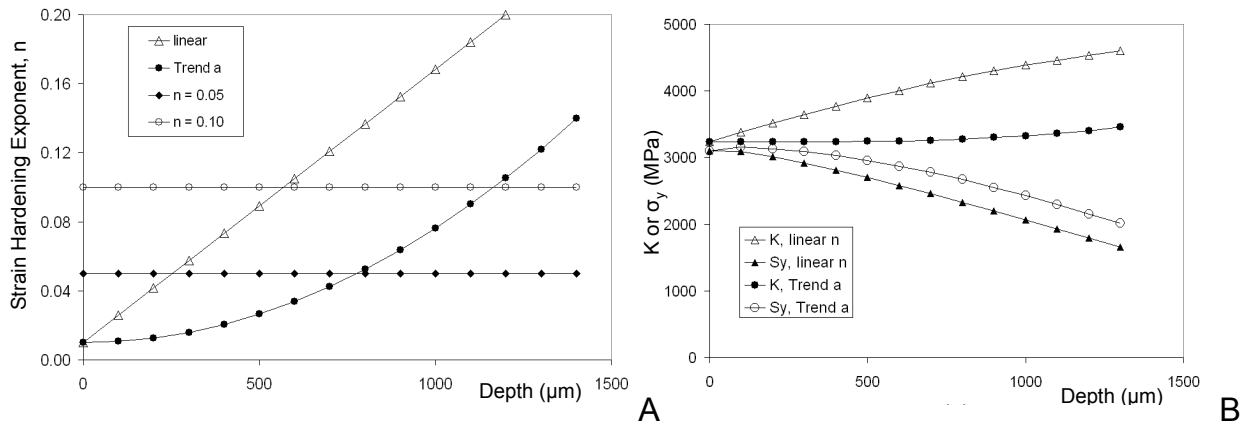


Figure 6-21. (A) Two new trends in strain hardening exponent, “linear” and a nonlinear “Trend a” result in (B) new trends in K and σ_y as calculated by Gao et al. (2006) yet still satisfy the virgin hardness trend of Figure 6-13.

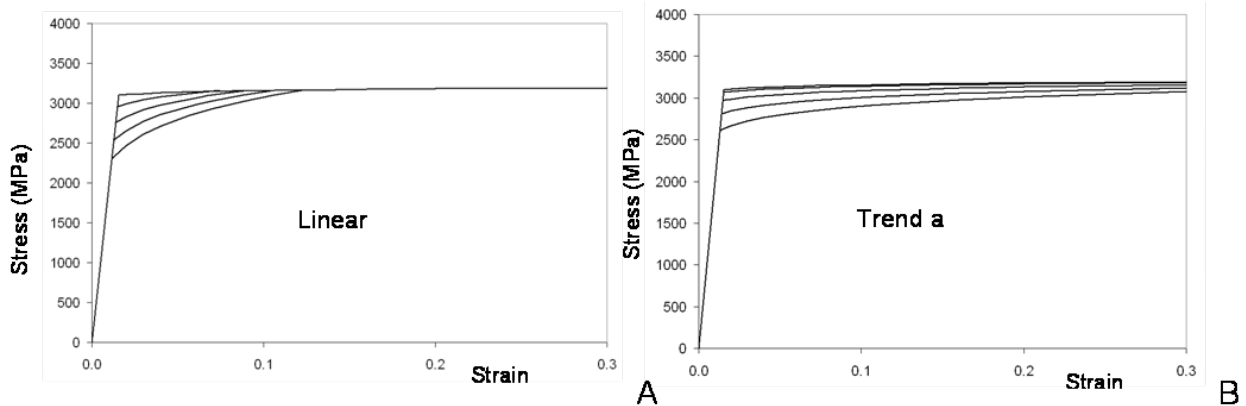


Figure 6-22. (A) Flow curve variation for linear gradient in n with depth, and (B) flow curve variation for “Trend a” – (nonlinear increasing trend in n).

Note the constant $n = 0.05$ trend underestimates the hardness at the deeper regions of the plastic zone while over predicting hardness in regions of large plastic strain. On the other hand, the constant $n = 0.10$ trend also over estimates hardness in regions of large plastic strain but provides a better match to the deeper region of the plastic zone. From these results it can be inferred that the strain hardening exponent is too large in regions close to the surface and too small at the deeper regions. This is

indicative of the relatively small increase in hardness (20 Hv) in a region with a known large amount of plastic strain (close to the surface) and somewhat larger increase in hardness (35 Hv) in the deeper, but lower plastically strained regions.

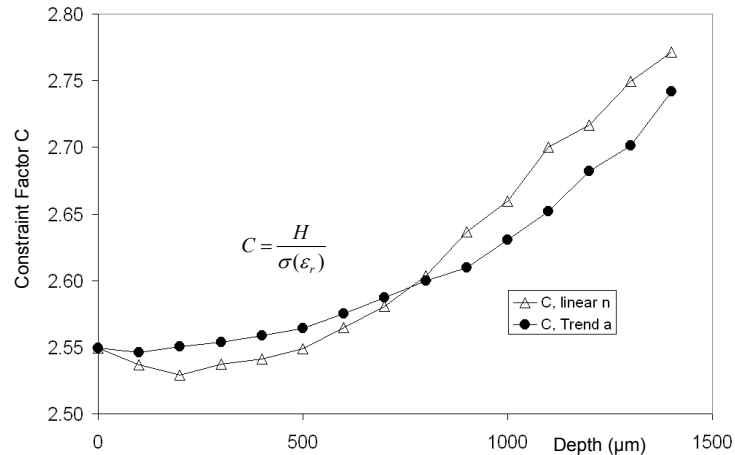


Figure 6-23. Constraint factor C for linear trend in n and for Trend a.

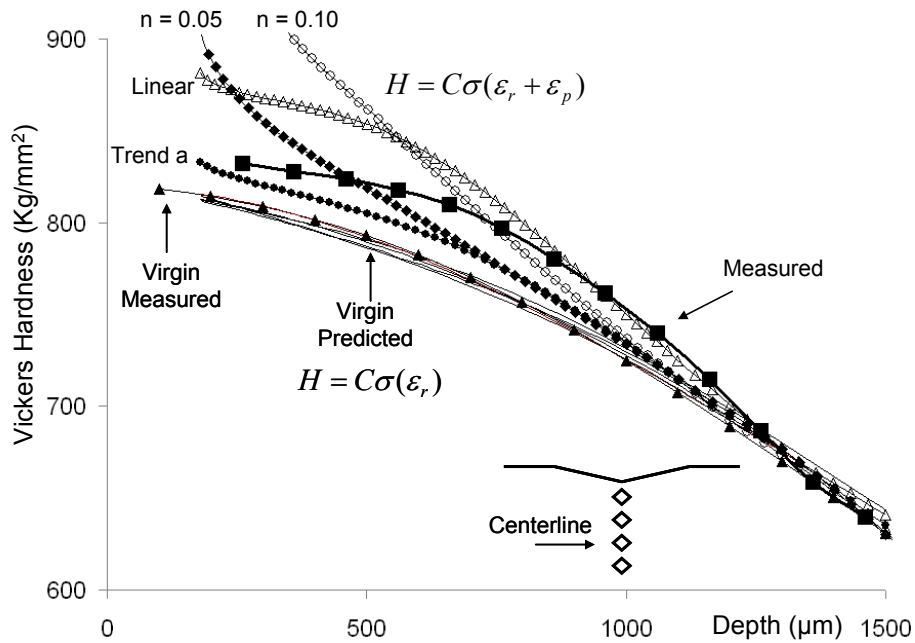


Figure 6-24. “Linear” and “Trend a” test cases provide better fit to measured hardness data but also act as upper and lower bounds of possible trends in strain hardening exponent n .

Based on this information, two new trends in n are assumed and the same process is repeated of determining the variation in flow curve based on the virgin hardness

trend. The value for n will now be relatively low at the surface, $n = 0.01$, and increase linearly to 0.23 at a depth of 1400 μm .

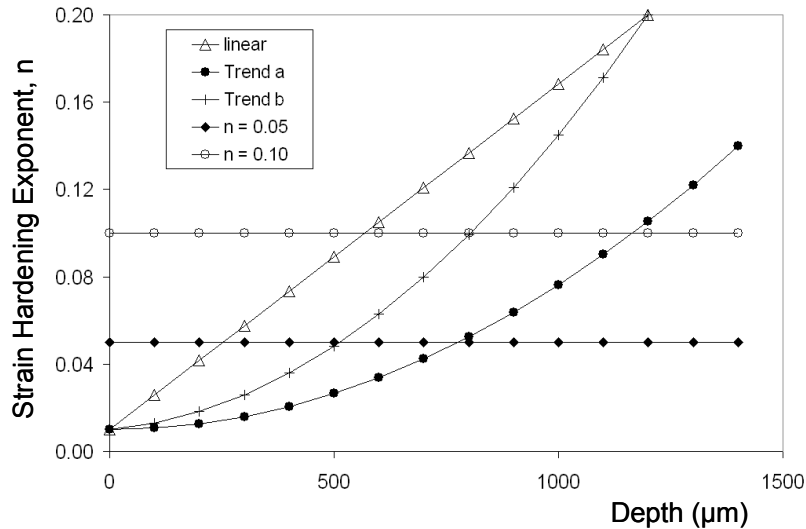


Figure 6-25. Trend b falls between upper and lower bounds determined by trends “linear” and “a.”

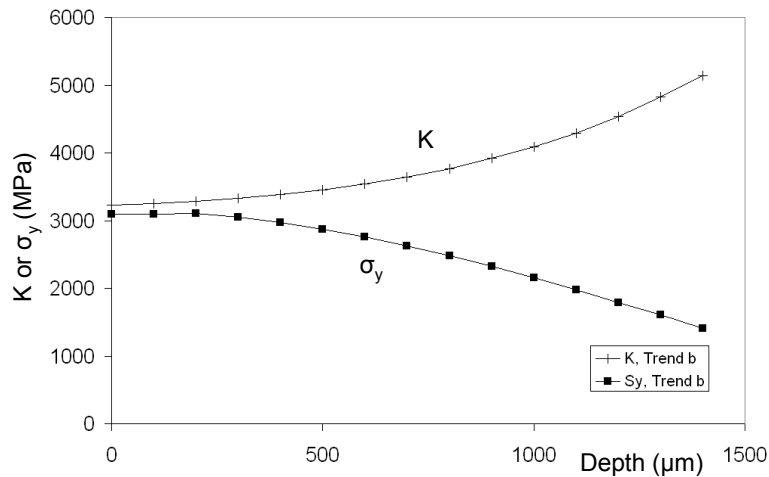


Figure 6-26. Variation in strength coefficient K and yield strength σ_y for Trend b.

The second trend (denoted “Trend a”) will use a nonlinear trend in n with depth which is similar to the nonlinear trend in virgin hardness. Here, n will be relatively low ($n = 0.01$) and increase parabolically to $n = 0.14$ at a depth of 1400 μm (Figure 6-21A). The variation in strength coefficient and yield strength can now be determined from the ECM of Gao et al. (2006) knowing the virgin hardness, elastic modulus and variation in

n with depth (Figure 6-21B). The variation in flow curves are shown in Figure 6-22 and the corresponding constraint factors are calculated and shown in Figure 6-23.

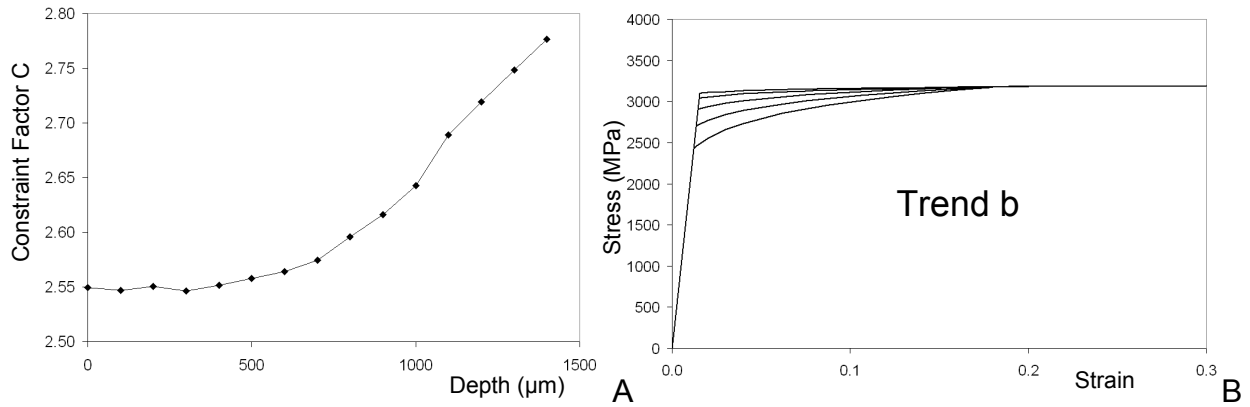


Figure 6-27. (A) Constraint factor C and (B) flow curve variation for Trend b.

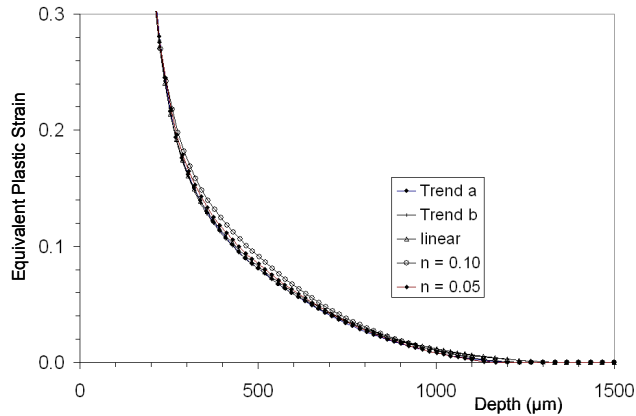


Figure 6-28. Equivalent plastic strain distribution along centerline of plastic zone for all test cases shown here.

The flow curves of Figure 6-22 are inserted into the finite element model and the macro indentation of M50 NiL is simulated. The plastic strain gradient is calculated and converted to hardness using the equation, $H = C\sigma(\varepsilon_r + \varepsilon_p)$ and plotted in Figure 6-24.

Note the “Linear” trend looks better, but the values for hardness are still over-predicted in regions of large plastic strain close to the indent tip. This is somewhat of an “upper bound” of possible plastic response in the sense that the trend is correct, but the values are too high. “Trend a” also has a similar trend, but under predicts the increase in

hardness and thus provides a lower bound on possible variations in strain hardening exponent.

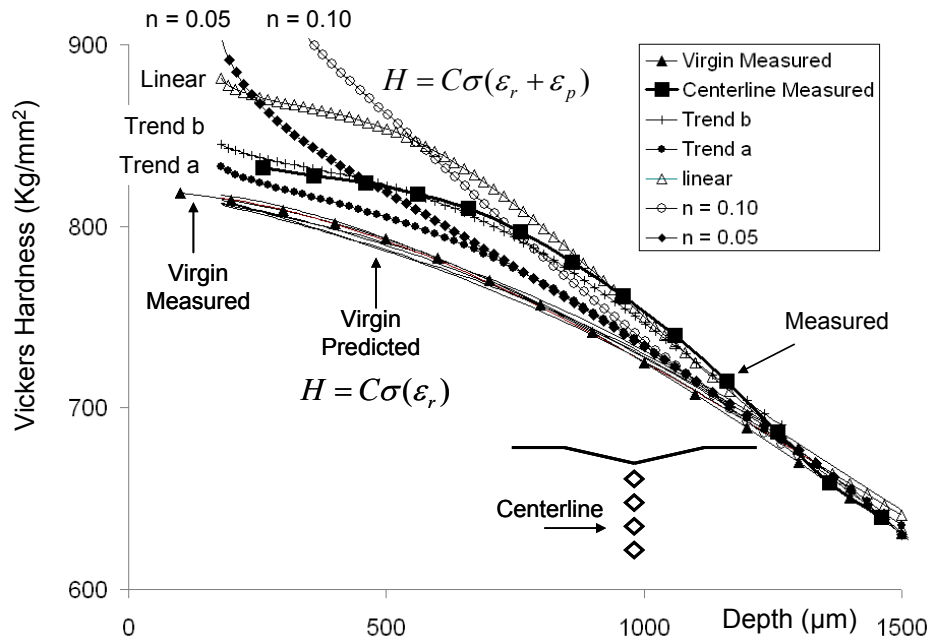


Figure 6-29. Trend b provides best fit to predicted hardness data and falls between upper and lower bounds provided by “Trend a” and “Linear.”

A new, nonlinear, trend in n is assumed and will be denoted Trend b as shown in Figure 6-25. It will fall between Trend a and the linear trend in n as these were the upper and lower bounds of possible variations in n . This trend in strain hardening exponent along with the virgin hardness profile will be used along with the ECM of Gao et al. (2006) to again determine the variation in yield strength and strength coefficient (Figure 6-26) for this specific trend in n . The corresponding variations in constraint factor and flow curve are shown in Figure 6-27.

This trend in flow curve is inserted into the FE model and the macro indentation of the M50 NiL is simulated to the same indent depth. The FE model calculates the corresponding equivalent plastic strain along the plastic zone’s centerline (Figure 6-28)

and this will be used along with the equation $H = C\sigma(\epsilon_r + \epsilon_p)$ to predict the increase in hardness within this region as shown in Figure 6-29.

Note that Trend b provides the best fit when comparing predicted and measured hardness values along the centerline of the macro indent's plastic zone. The equivalent plastic strain decreases asymptotically along the plastic zone's centerline and that all plastic strains below a depth of 700 μm are considerably low, i.e. 0.04 or less. The hardness measurements at these locations correspond to a flow stress on the flow curve at that specific depth, thus the higher the plastic strain, the "farther away" the flow stress is from its original yield strength (Figure 6-30).

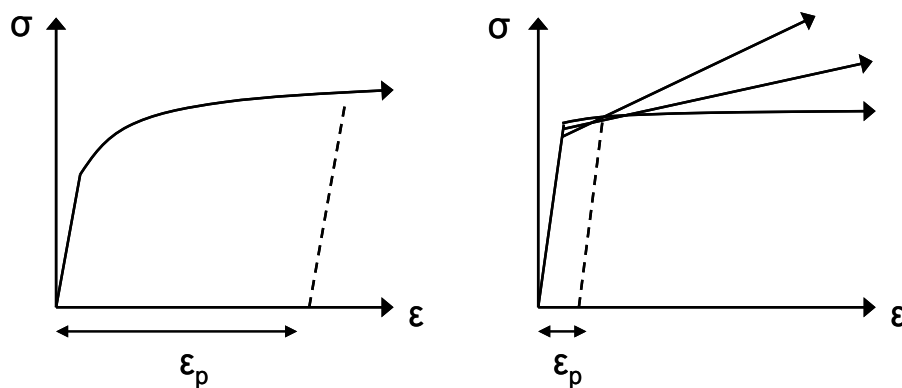


Figure 6-30. The sensitivity to strain hardening exponent decreases with decreasing plastic strain in that flow curves that have similar flow stresses at low plastic strain could have entirely different plastic responses at large plastic strain that this method would not be able to predict.

In other words, this method can only predict the plastic response at any given depth up to the maximum plastic strain that was experienced at that specific depth. This is why the hardness measurements were performed along the centerline because this is where the highest plastic strain occurs along a specific depth. Thus, it is possible to have a set of flow curves that have similar plastic responses at low plastic strains, but an entirely different plastic response at large plastic strain (Figure 6-31) and significantly

different n values. Caution should therefore be taken when considering the plastic response predicted by this method for regions with low plastic strains. This is why the flow curves at depths 0, 200, 400, 600, and 800 μm were shown in this chapter and not the flow curves for the deeper material. The plastic zone extended to 1300 μm and trends for n , K , and σ_y were shown up to these depths, but these values are only valid up to the maximum plastic strain that was experienced along their specific depths. These material properties of Trend b will be used to repeat the spall edge impact analysis of for M50NiL in Chapter 7.

Key Points

- A reverse analysis was presented here for plastically graded materials to determine the plastic response of case hardened M50 NiL in order to repeat a similar spall edge impact analysis of Chapter 3 for this specific material which is presented next in Chapter 7.
- The sensitivity to strain hardening exponent decreases as the maximum plastic strain experienced at a specific depth decreases. More simply, this method can only predict the plastic response up to the maximum plastic strain that was experienced at a specific depth. Plastic strains at larger depths are so small that practically any value for n would result in a predicted hardness that could provide a reasonable fit to what was experimentally measured.
- The reverse analysis for nongraded materials was essentially repeated for every depth within the plastically deformed graded material. In the nongraded reverse analysis, various values for n were assumed and tested for accuracy for a continuous, nongraded material. In the graded material reverse analysis, logical trends in n that vary with depth were tested for accuracy through the prediction of experimentally measured hardness values.
- All of the variations in flow curves that were based on an assumed variation in n reflect the same virgin hardness profile because they satisfy the condition set by Gao et al. (2006) which relates virgin hardness to strain hardening exponent, yield strength, and elastic modulus. The strain hardening characteristics were identified by the measured increase in hardness at a specific depth and the corresponding plastic strain was determined by FE modeling.
- This indentation method to determine the plastic response of graded materials is similar to that presented in Chapter 5 with the exception that the lower bound of the gradation in plastic response is initially unknown.

CHAPTER 7 SPALL MODELING

Spall Propagation for 52100, M50, and M50 NiL Bearing Materials

The flow curve for M50 NiL as a function of case depth that was determined in Chapter 6 will now be used to repeat the ball-spall edge impact analysis introduced in Chapter 3 and compared to M50 and 52100 bearing steels to determine if the FE model can predict the differences in spall propagation characteristics of these materials. In this analysis the magnitude and distribution of plastic strain will be indicative of the amount of damage induced by a ball impact on a spall edge. More damage in the form of plastic strain is expected to cause spalls to propagate sooner and faster since fatigue crack initiation and growth is highly dependent on the extent of plastic deformation.

A concise review of the spall propagation experiments by Rosado et al. (2010) and Chapters 1 and 3 are reprised here. Scaled versions of the bearings used in the actual aircraft engines were tested for spall-propagation in controlled experiments at the Air Force Research Labs, WPAFB, Ohio. The bearings were 208 size (40 mm bore) split inner raceways with 0.5 in diameter balls. Their study investigated 52100, M50 through-hardened, and M50 NiL case hardened bearing steels. The M50 and M50 NiL bearings used silicon nitride balls while the 52100 bearings used 52100 steel balls. Brand new bearings and bearings that had been subjected to as much as tens of billions of stress cycles were both used in their study to see if initial rolling contact fatigue affected spall propagation rate.

Figure 7-1 taken from Rosado et al. (2010) displays the mass loss from the raceway surface for all three types of bearings as a function of millions of stress cycles during spall propagation for new bearing raceways. These raceways were indented

with Rockwell C indents to act as stress risers, initiate fatigue cracks during bearing operation, and reduce the amount of time to spall initiation. The bearings were inserted into a test rig and operated at a maximum contact pressure of 2.41 GPa (350 ksi, as seen on the virgin raceway surface). The mass loss from the spalled bearing was detected by an oil debris monitor (ODM) and the average size of the spalled particles were on the order of 100 μ m Rosado et al. (2010). Note 52100 bearing steel had the shortest amount of time to spall initiation and the fastest spall propagation rate whereas both the M50 and M50NiL steels showed the longest amount of time to spall initiation and a slower spall propagation rate. Note the similarity in both M50 and M50 NiL with two outliers for M50.

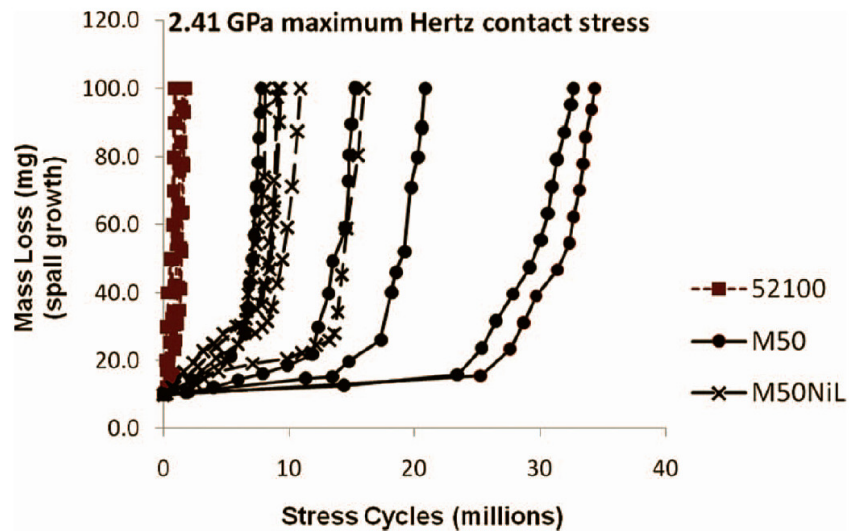


Figure 7-1. Spall propagation characteristics for M50, M50 NiL, and 52100 bearing steels. Spalls initiated by Rockwell C indents on virgin raceways at maximum contact pressure of 2.41 GPa (350 ksi). Rosado et al. (2010)

A similar experiment was performed with a lower contact pressure (2.10 GPa virgin raceway (305 ksi), Figure 7-2) and as expected the amount of time to spall propagation was considerably longer due to the lower contact stresses, but the trends

were similar. Note in both cases M50 NiL and M50 steels outperform 52100 whereas the differences between M50 and M50 NiL are not so obvious.

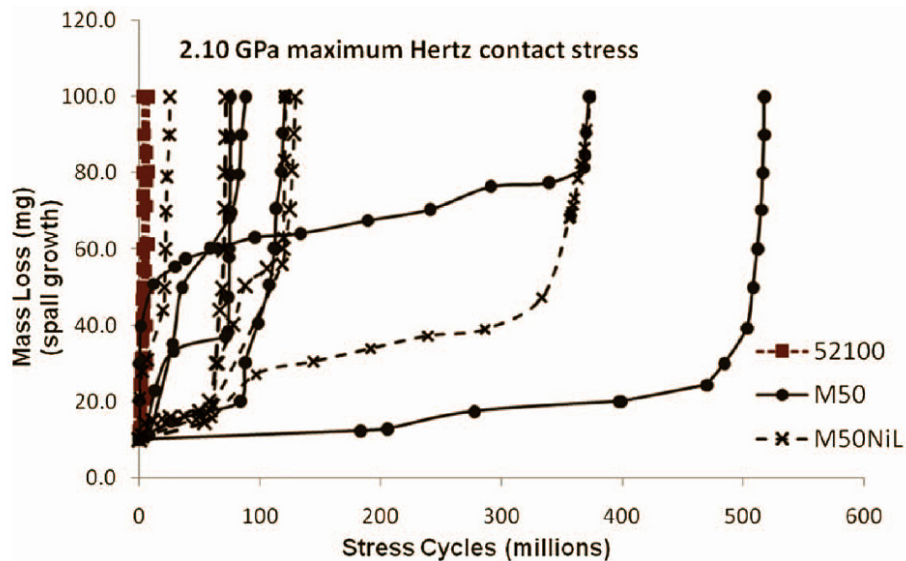


Figure 7-2. Spall propagation trends for new (indented) bearings at 2.10 GPa (305 ksi) maximum contact pressure (Rosado et al., 2010).

Similar tests were done on life-endurance tested bearings that were run continuously at 10,000 rpm for 5 months prior to natural spall initiation or test suspension after approximately 10 billion stress cycles. The suspended bearings were indented with Rockwell C indents to initiate a spall and the consequent mass loss from the surface as a function of stress cycles is shown in Figure 7-3 for a maximum contact pressure of 2.41 GPa.

Due to the cost and amount of time required to perform these tests, there are only 7 bearings available to compare in this graph. But it can be inferred here that M50 NiL out performed the other bearing materials in this study as seen by its longer time to spall growth and relatively slower spall propagation rate. Interestingly, spalls propagated sooner and faster for the M50 life-endurance tested bearings when

compared to 52100 and M50 NiL (Figure 7-1). This suggests that spalls propagate faster and sooner for M50 bearings that have been in service for a considerable time.

These results also suggest that the accumulated cyclic fatigue damage in the neighborhood of a spall is less for the virgin indented raceways than for the life-endurance tested bearings. Even though the spall edges appear similar, the localized accumulated damage is greater for the life endurance tested bearings. This leads to the faster propagation rates shown in Figure 7-3 when compared to those in Figure 7-1, even though they were performed at the same contact stress.

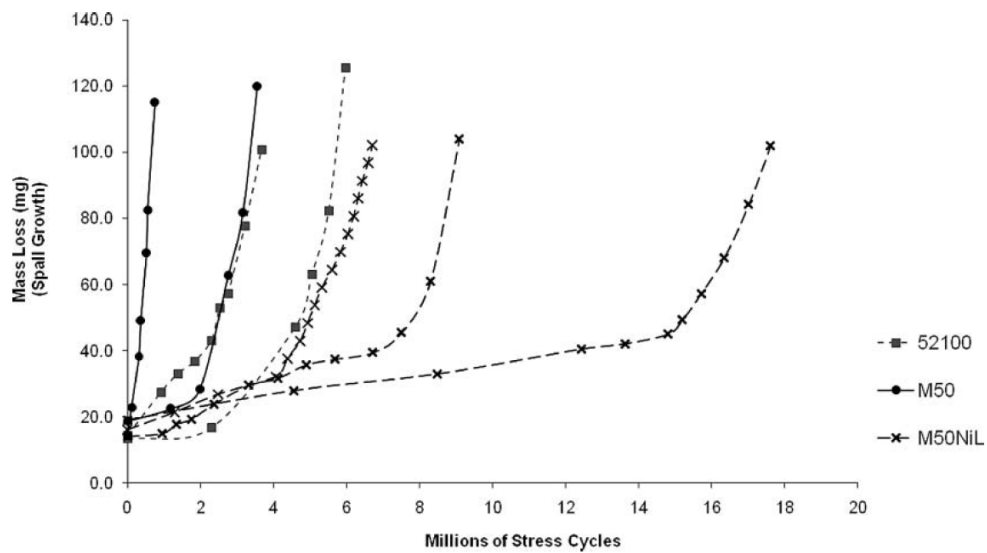


Figure 7-3. Spalls propagate faster on life-endurance bearings when compared to the new indented bearings of Figure 7-1 at the same maximum contact pressure of 2.41 GPa (350 ksi) (Rosado et al., 2010).

The actual dynamics of the interactions between a ball and raceway spall are very complicated, but it is clear that severe damage is occurring within the spall edge due to these interactions. As an illustration, for a clockwise-rotating inner raceway, a ball will unload as it comes off the leading spall edge and then impact the trailing edge as it reestablishes contact between the raceways (Figure 7-4A). In these experiments, cracks were observed to occur on the trailing spall edge (Figure 7-4B) and not on the

leading edge. Only the trailing edge propagates with bearing operation while the leading edge remains. It is currently unknown how or why these cracks are forming, but it is well understood that these cracks grow and liberate material with continued ball impacts and bearing operation.

Both the leading and trailing spall edge experience a “pinch” as the ball unloads and reloads itself between the inner and outer raceway. However, the trailing edge is the only edge that experiences the impact and propagates. The work presented here will provide an explanation for this crack formation within the spall edge due to the ball impact as well as the influence of material plastic response, ball mass, gradient in hardness, and initial compressive residual stress within the raceway.

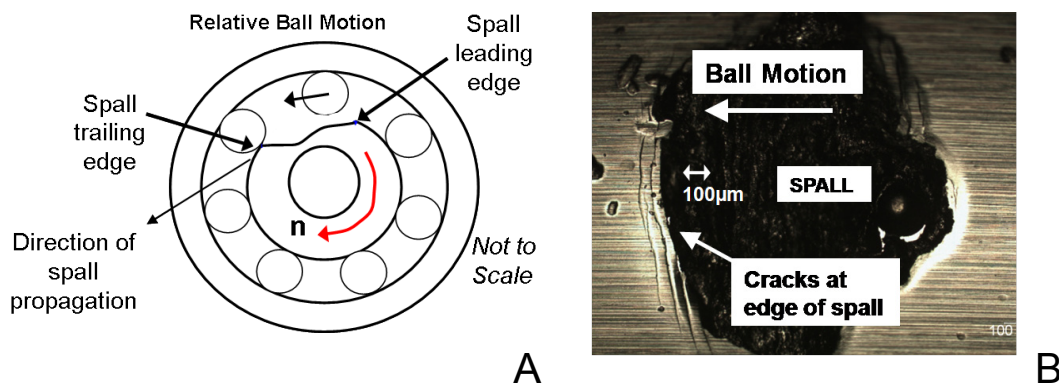


Figure 7-4. (A) Schematic showing relative ball motion between leading and trailing spall edge for clockwise-rotating inner raceway. (B) Cracks form on the trailing spall edge that is subjected to ball impacts. This spall edge is deteriorating with continued bearing operation as these cracks grow and liberate surface material.

Finite Element Model

The same FE model from Chapter 3 that was used to model the ball impact of through-hardened M50 steel will be used again here for both 52100 and M50 NiL bearing steels, a few important details of which are outlined here. Actual bearing dynamics are very complex with interactions between the balls, cage, and both

raceways, but are not considered here in interest of time and simplicity. Also, the effects of the outer raceway are not considered here because both the leading and trailing edges of the spall are subjected to the pinch of the outer race during ball unloading and reloading, respectively. Since only the trailing spall edge is experiencing the ball impact and propagating, only the ball impact will be modeled. The ball is given a mass and velocity and allowed to impact the spall edge (Figures 7-4 and 7-5). The mass of both steel and silicon nitride balls will be used here to determine the influence of ball mass on the stresses and strains that develop within the spall edge due to the impact.

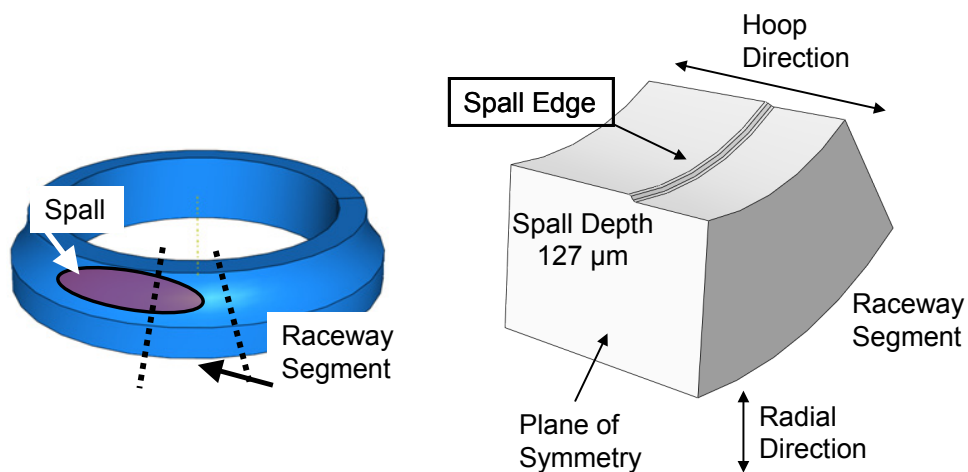


Figure 7-4. Only segment of inner raceway is modeled.

The finite element model will simulate three successive rigid ball impacts on the same spall edge at a ball velocity of 15.24 m/s (50 ft/s) (Figure 7-5). The ball velocity is determined from the kinematics of the known rotational speeds of the cage and raceways of the 208 size bearing used by Rosado et al. (2010). Three impacts were chosen because there was no significant difference in the stresses and strains within the spall edge after the second and third impacts. This is due to the fact that isotropic

hardening was used here, the cyclic hardening laws for these steels are currently unknown, and to reduce model run-time.

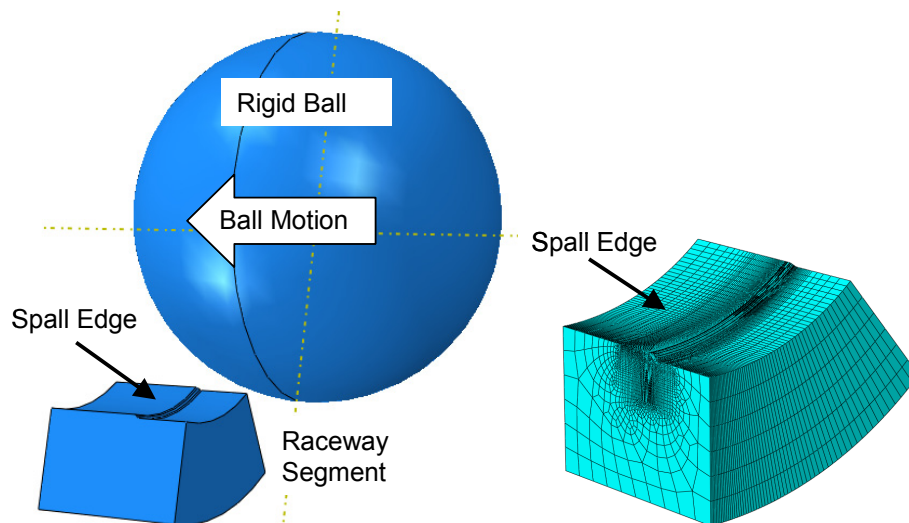


Figure 7-5. Finite element model and mesh of impact analysis.

The ball is not allowed to spin and can only translate within the plane of symmetry. A very fine linear hexahedral mesh is designed around the spall's edge because the most critical stresses and strains are forming in this small region (Figure 7-5). The explicit solver within ABAQUS v6.8-2 was used since this is a transient analysis and has time-dependent properties (the velocity of the ball). The von Mises (J2) failure criterion, associative flow rule, and isotropic hardening are appropriate for bearing steels and implemented here.

Bearing Materials

The flow curve for commercial 52100 bearing steel was obtained from Stickels (1977) where compression tests were performed on specimens that were tempered at temperatures ranging from 149 to 260°C. The 52100 steel used in the spall propagation test was tempered at 200°C (Rosado et al., 2010) and its flow curve is shown in Figure 7-6A. The flow curve for M50 through-hardened steel was obtained by an in-house

compression test discussed in Chapter 3 and agreed with data obtained from Carpenter and shown again in Figure 7-6B. The flow curve obtained by the indentation method presented in Chapter 6 for M50 NiL for the surface is shown alongside those of M50 and 52100 for comparison in Figure 7-7. The flow curves have very low strain hardening characteristics which is common for many high yield strength steels (Lai and Lim, 1991). The flow curves are extrapolated to large strain for the FE model incase this extent of deformation is achieved locally within the spall edge.

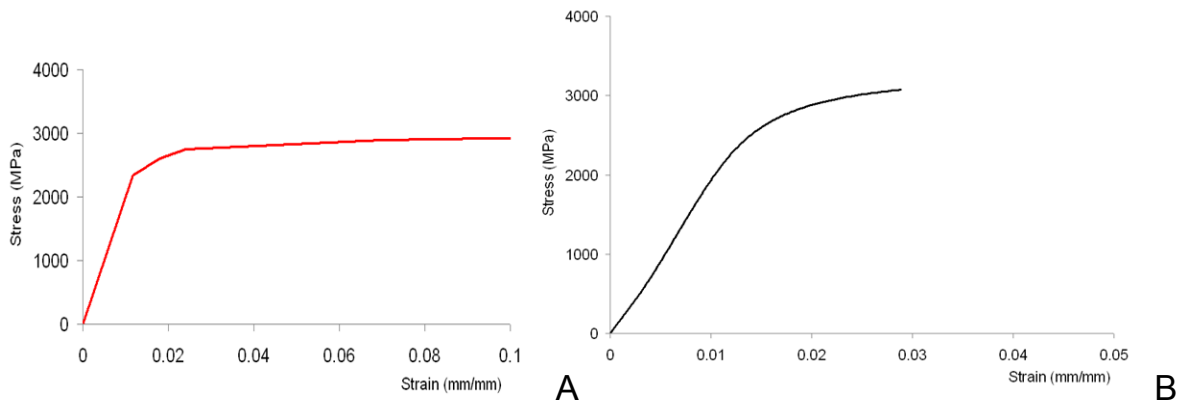


Figure 7-6. Flow curves for (A) 52100 and (B) M50 steel.

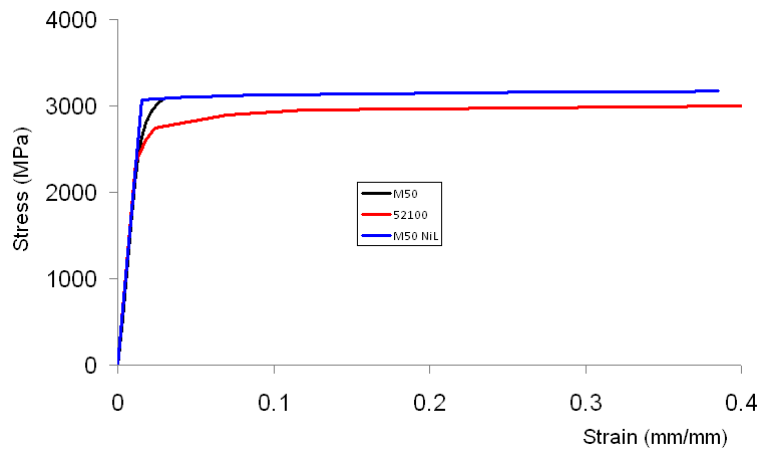


Figure 7-7. Flow curves for M50, 52100, and the surface of M50 NiL.

It is not surprising that the flow curves for M50 and the surface of M50 NiL are similar. Since they both have the same hardness (64.5 HRC), elastic modulus, and considerably low strain hardening exponents, they also have a similar flow curve. This

was predicted by Gao et al. (2006) and similar trends were shown in Chapter 6. Also, the flow stresses of M50 and M50 NiL are 200-300 MPa higher than that of 52100. This is a result of 52100's lower hardness (62.2 HRC) when compared to that of M50 and M50 NiL (64.5 HRC).

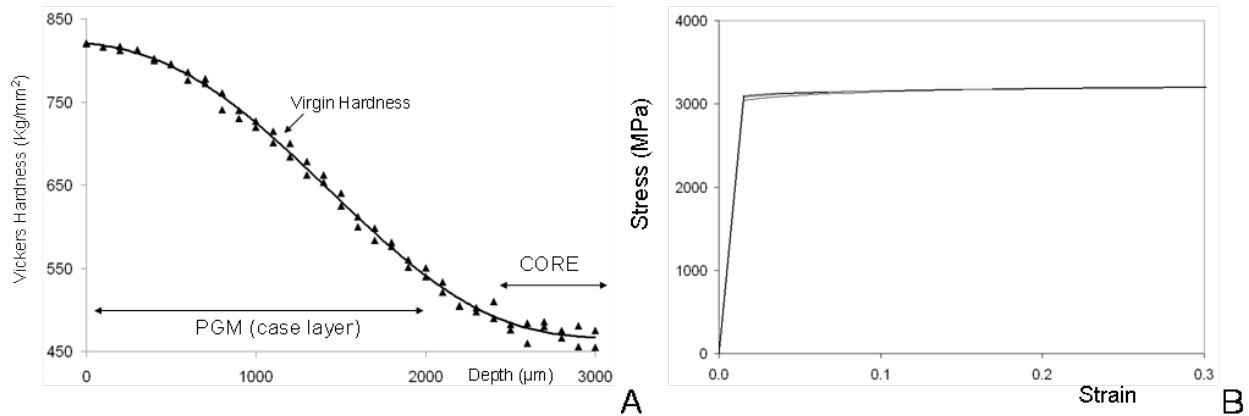


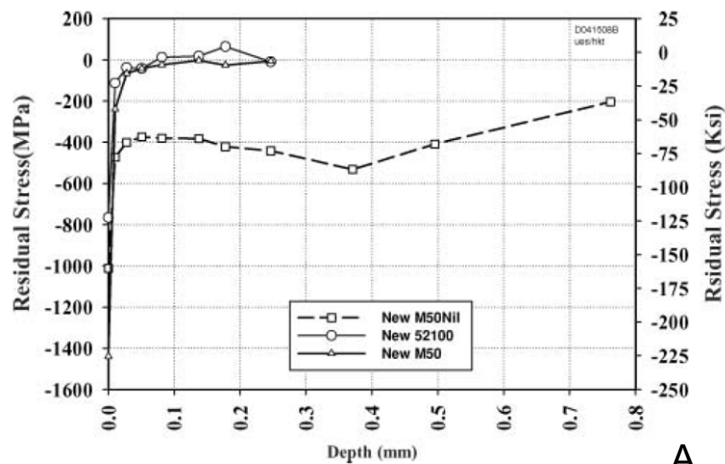
Figure 7-8. (A) Virgin hardness profile for M50 NiL and (B) resulting flow curves at depths of 0, 100, 200, and 300 μm are similar in magnitude.

Note the yield strength determined by the method of Chapter 6 is determined by the intersection of the flow curves $\sigma_y = E\varepsilon$ and $\sigma_y = K\varepsilon^n$. This explains the sharp corner in the stress strain curve at low plastic strain seen in Figure 7-7. Actual material behavior at low plastic strain is closer to what is seen in the M50 compression test where a gradual increase in flow stress is observed at low plastic strain. This discrepancy at low plastic strain will not have a marked effect on the spall propagation results since the maximum plastic strain within the spall edge can be as high as 20 to 30 %.

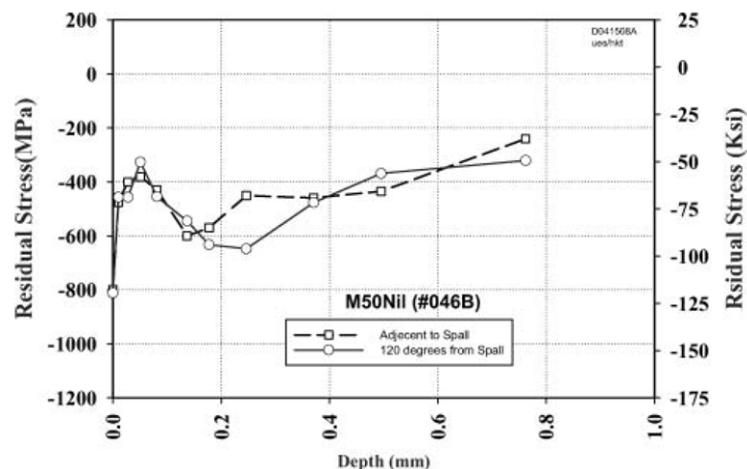
Recall from Chapter 6 that the virgin hardness profile for the case hardened M50 NiL is nonlinear with depth (Figure 7-8A) and nearly constant within 300 μm of depth from the surface. The resulting flow curves were also similar for depths close to the surface (Figure 7-8B). Thus the plastic response for through-hardened M50 and case hardened M50 NiL are similar in regions close to the bearing surface.

Residual Stress Profile M50 NiL

Residual hoop stress profiles obtained from X-Ray Diffraction (XRD) methods and presented in Forster et al. (2010) are shown in Figure 7-9A for the virgin bearing steels used in this study.



A



B

Figure 7-9. (A) Residual hoop stress profile for 52100, M50, and M50 NiL prior to bearing operation. (B) Residual hoop stress profile for M50 NiL next to spall edge and 120 degrees from M50 NiL spall (Forster et al., 2010).

Considerably large residual compressive stresses are present at the immediate surface which is due to the final finishing of the bearing, but drop off substantially over a

depth of 10 μm . There is an initial compressive residual hoop stress profile due to the case-hardening of the M50 NiL bearing steel that is a nearly constant 400 MPa up to a depth of 1 mm. XRD was also performed in close proximity to the spall edge and 120 degrees from the spall edge for a spalled bearing as shown in Figure 7-9B. Note the compressive residual stress is still present in proximity of the spall edge. The irradiated area was on the order of 1 x 1 mm and considerably larger than the resolution needed to compare to the residual stress profiles obtained from finite element models shown next.

Finite Element Model of Initial Residual Hoop Stress

This initial residual compressive hoop stress of 400 MPa must be taken into account in the FE model of the ball-spall edge impact analysis of M50 NiL. The effects of residual hoop stress are believed to retard crack formation and spall propagation (Forster et al., 2010) and is expected to affect the calculation of plastic strain within the impacted spall edge in the FE model. The residual stresses within the FE model can be applied many different ways, but in this analysis an external elastic displacement is applied at either end of the raceway segment to induce the desired compressive hoop stress of 400 MPa. This is similar to applying a temperature and coefficient of thermal expansion to the segment while it is constrained at either end. In that case the segment is allowed to expand a certain amount and then elastically compressed to the desired stress state. Figure 7-10 shows the initial residual hoop stress state of the FE model prior to ball impact.

Note the residual stress is a compressive 400 MPa throughout the raceway segment with the exception of the immediate spall edge. At the free surface of the spall edge, the residual stresses drop to -70 MPa at the location where initial ball contact

occurs. Boundary conditions cannot be applied to the spall edge in order to induce more compressive stress because this is the same location as the ball impact.

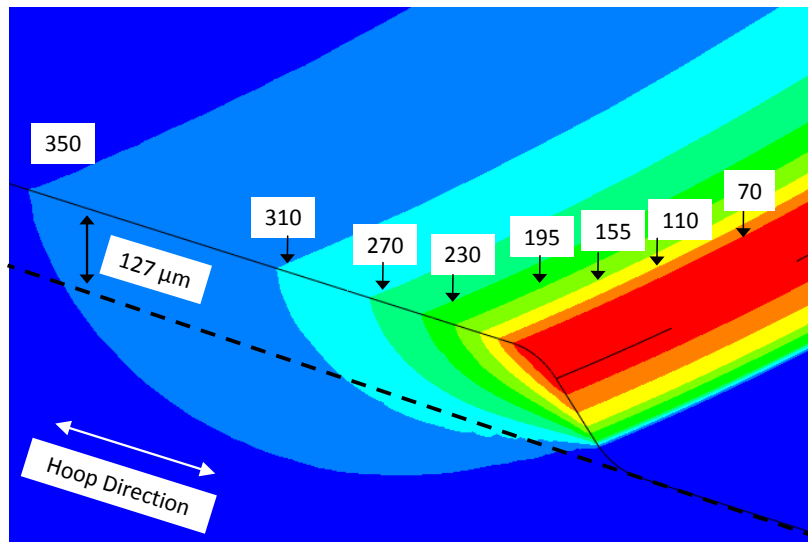


Figure 7-10. Compressive residual hoop stress state within raceway segment prior to ball impact.

The compressive residual stress of 400 MPa is present just below the spall edge at a depth of 127 μm . This is likely to occur in the actual spalled bearing but cannot be verified by XRD because the spot size of 1 x 1 mm is too large to detect this lack of residual stress on the immediate spall edge where the actual cracks are forming. The fact that the residual compressive stresses are so low at the spall edge may not affect the formation of plastic strain within this region when compared to a spall edge with zero initial compressive stress. The effects may become more obvious in the calculation of plastic zone depth, which as seen in Chapter 3, can exceed 250 μm .

RESULTS

M50

The results of the ball impact analysis for M50 through-hardened steel from Chapter 3 are repeated here for convenience in order to compare with the results obtained for 52100 and M50 NiL bearing steels shown afterwards. The mass of silicon

nitride balls were used in this model since the M50 steel raceways were paired with ceramic silicon nitride balls in the spall propagation tests of Rosado et al. (2010). The density of silicon nitride used in this analysis was 3.2 g/cm^3 .

The residual hoop stresses after the impacts are shown in Figure 7-12. The location of high tensile residual hoop stress is in same location as the cracks in actual spalled bearings (Figure 7-4B).

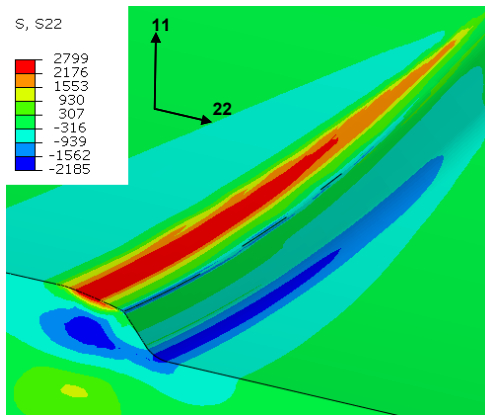


Figure 7-12. Residual hoop (22 direction) stresses in proximity of spall edge. Note region of high tensile residual stress in same region as cracks appear in spall bearing raceway (Figure 7-4B).

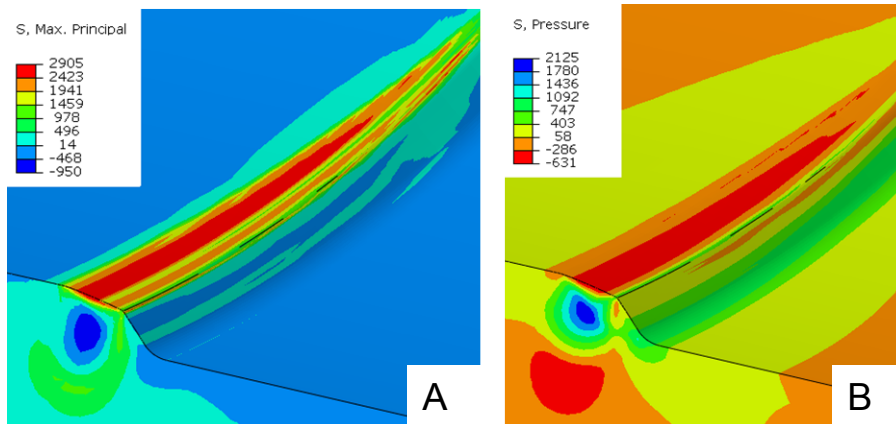


Figure 7-13. (A) Residual maximum principal stress and (B) residual hydrostatic stress in proximity of spall edge for M50 steel. (Tensile hydrostatic stress is negative).

There is also high compressive residual stress just beneath the spall edge which is believed to keep crack growth and spall propagation localized to the immediate surface

as seen in the experiments. The residual maximum principal stress and residual hydrostatic stress profiles are shown in Figure 7-13A and Figure 7-13B, respectively. Note the similarity in the locations of residual tensile and compressive stress within the impacted spall edge. Research conducted by Howell et al. (2004) has shown that fatigue cracks are likely to initiate in regions of large hydrostatic tensile stress and agrees with the locations of cracks in the spalled bearings.

The strain-life approaches summarized in (Suresh, 2004), such as Coffin-Manson shown below, determine that the number of stress cycles required to initiate a crack decreases with increasing plastic strain:

$$\frac{\Delta \varepsilon}{2} = \frac{\Delta \varepsilon_e}{2} + \frac{\Delta \varepsilon_p}{2} = \frac{\sigma'_f}{E} (2N_f)^b + \varepsilon'_f (2N_f)^c \quad (7-1)$$

where the total strain amplitude $\Delta \varepsilon$ is the sum total of the elastic $\Delta \varepsilon_e$ and plastic $\Delta \varepsilon_p$ strain amplitudes. A detailed quantitative fatigue life analysis cannot be made here since the cyclic strain-life data (such as the constants b and c) for these bearing steels is scarce, the plastic strains calculated by the FE model are for a spall that only suffered three impacts, and the cyclic plastic strain amplitudes from the FE model are highly dependent on its cyclic strain hardening law which is also limited for bearing steels. As a qualitative investigation, however, it is worth comparing the distribution of plastic strain within the spall edge with the location of cracks in the actual bearings to see if cracks form in the most damaged region as predicted by the FE model.

The distribution of maximum principal plastic strain is shown in Figure 7-14. The plastic zone size is 250 μm in depth and 315 μm in width and defined by the 0.2 % plastic strain contour. The maximum plastic strain is 0.206 and occurs in the center of

the red-highlighted region within the spall edge. This region of highly plastically deformed material is a likely site of fatigue crack initiation and growth.

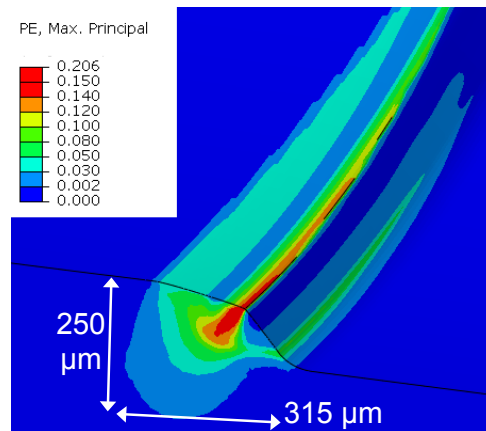


Figure 7-14. Plastic zone size and maximum principal plastic strain within spall edge of M50 material.

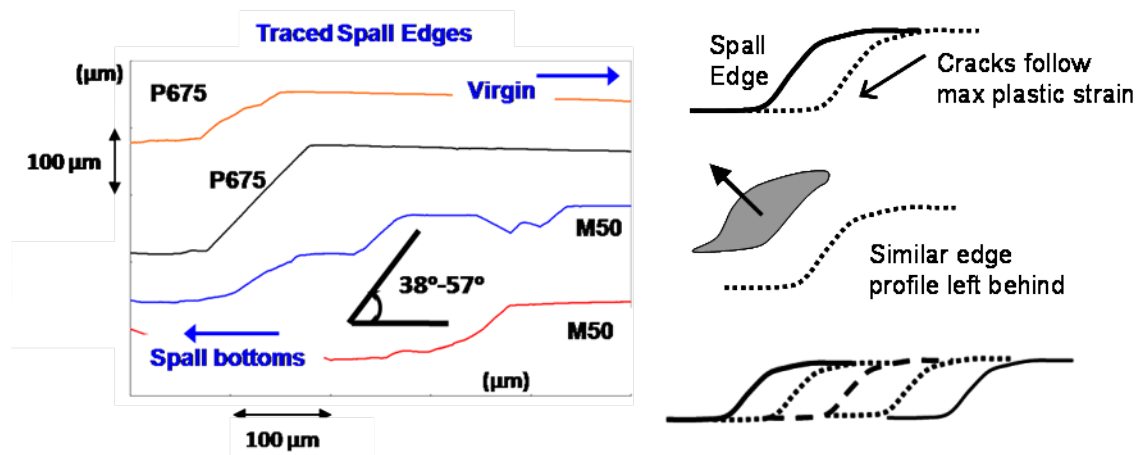


Figure 7-15. Spall edge geometry from profilometer tracings. Spall edge shape is similar throughout spall propagation.

Recall from Chapters 1 and 3 that the spall edge geometry is similar throughout spall propagation as determined by the profilometer tracings done at AFRL on bearings with various spall lengths (Figure 7-15). This suggests that the observed cracks are following the path of most damaged material and leaving behind similar spall edge geometry upon liberation of material. Thus the resulting spall edge shape is supported by the magnitude and distribution of maximum principal plastic strain. The distributions

of the maximum principal plastic strain support a logical path of crack initiation and growth in the sense that cracks are likely to develop and grow in regions of high plastic deformation. However, once a fatigue crack forms and more ball impacts occur, the stress and strain distribution within the spall edge is expected to change dramatically, thus the results of Figure 7-14 are not definitive. Also note that multiple cracks form on a typical spall edge and the deformation that actually occurs is not as “clean” as what the FE model predicts.

52100

The flow curve for 52100 is inserted into the same FE model and the repeated ball impacts are simulated. Steel balls are used in this model since the 52100 spall propagation tests were conducted using 52100 steel balls. The density of steel used in this analysis was 8 g/cm^3 . Similar results are obtained when compared to the M50 steel. The residual hoop stresses are shown in Figure 7-16.

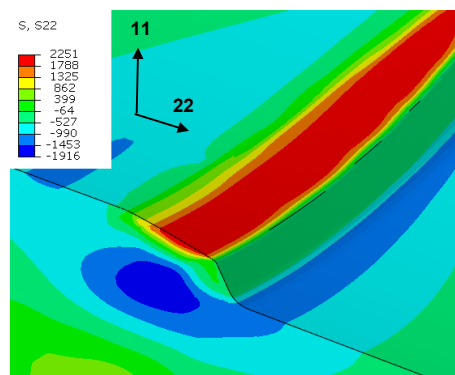


Figure 7-16. Residual hoop (22 direction) stresses in proximity of spall edge. Note region of high tensile residual stress in same region as cracks appear in spall bearing raceway.

Note the location of high tensile residual hoop stress is in same location as cracks in actual spalled bearing. There are also large compressive residual stresses just beneath the spall edge which is believed to keep crack growth and spall propagation localized to the immediate surface. Similar residual hydrostatic stress and residual

maximum principal stress profiles are shown in Figure 7-17A and Figure 7-17B, respectively.

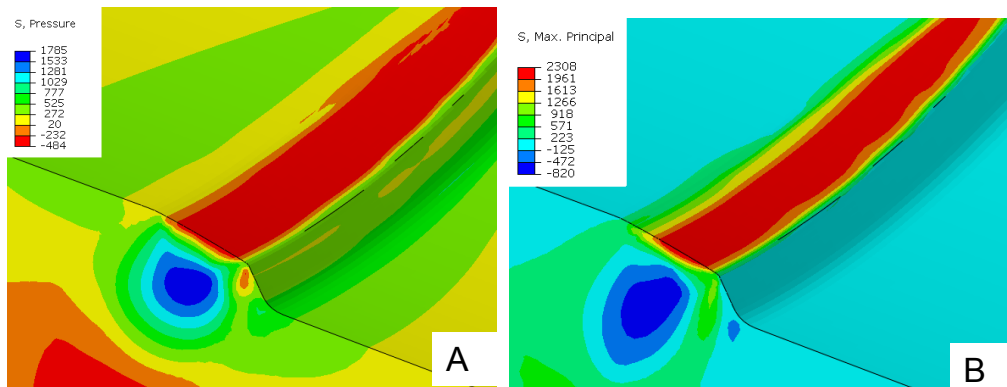


Figure 7-17. (A) Residual hydrostatic stress and (B) residual maximum principal stress in proximity of spall edge for 52100 steel.

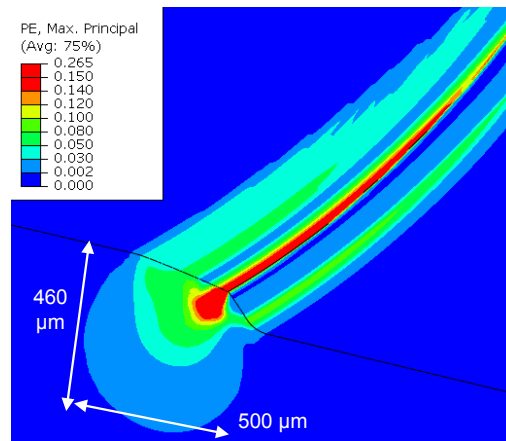


Figure 7-18. Plastic zone size and maximum principal plastic strain magnitude within spall edge of 52100 steel.

The distribution of maximum principal plastic strain is shown in Figure 7-18. The plastic zone size is 460 μm in depth and 500 μm in width which is 84 % deeper and 58 % wider than the M50 test case. The maximum plastic strain is 0.265 and 32 % higher than M50 (0.20). From these results it cannot be determined if the larger amount of plastic deformation is due to the heavier ball mass or lower hardness, but the contributions from each will be determined in a later section. The fact that 52100 exhibits greater plastic strains where cracks are forming and a larger volume of

plastically deformed material is indicative of the faster spall propagation rates seen in Rosado et al. (2010) and earlier in this chapter. Many fatigue failure theories such as Coffin-Manson predict cracks to form sooner in regions of greater plastic strain (Suresh, 2004) which supports the faster spall propagation behavior of 52100.

M50 NiL

The flow curve variation for M50 NiL that was determined in Chapter 6 is inserted into the same FE model and the repeated ball impacts are simulated using ceramic silicon nitride balls. There is also an initial compressive stress of 400 MPa within the raceway segment as discussed earlier in this chapter. Similar residual stress profiles around the spall edge after ball impacts are obtained when compared to the M50 test cases. The residual hoop stresses are shown in Figure 7-19.

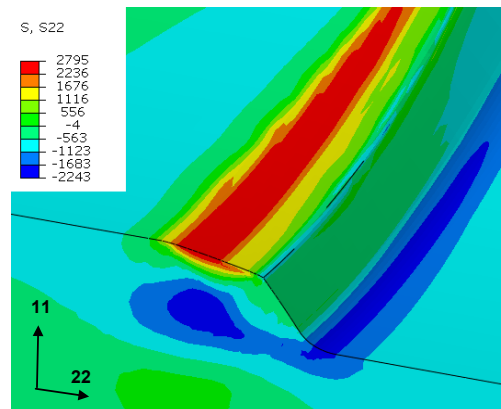


Figure 7-19. Residual hoop (22 direction) stress in proximity of spall edge of M50 NiL. Note region of high tensile residual stress in same region as cracks appear in spall bearing raceway.

Note the location of high tensile residual hoop stress is in same location as cracks in actual spalled bearing and the high compressive residual stress just beneath the spall edge. The residual hydrostatic stress and residual maximum principal stress profiles are shown in Figure 7-20A and Figure 7-20B, respectively. Once again there is similarity in the locations of residual tensile and compressive stress within the impacted

spall edge with the locations of cracks along with a similarity with the other bearing materials.

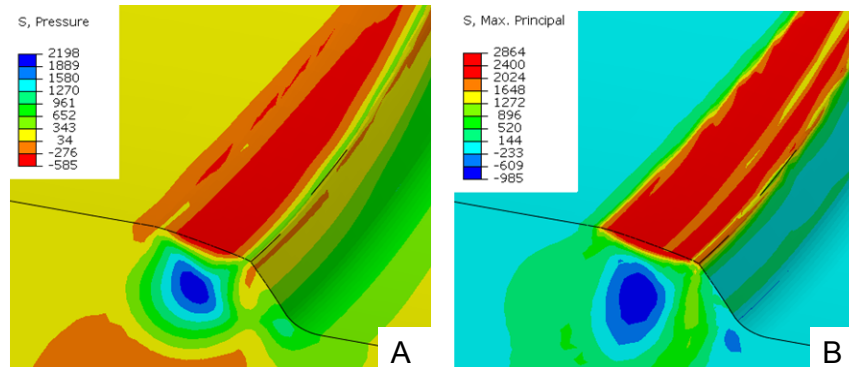


Figure 7-20. (A) Residual hydrostatic stress and (B) residual maximum principal stress in proximity of spall edge for M50 NiL steel. (Tensile hydrostatic stress is negative)

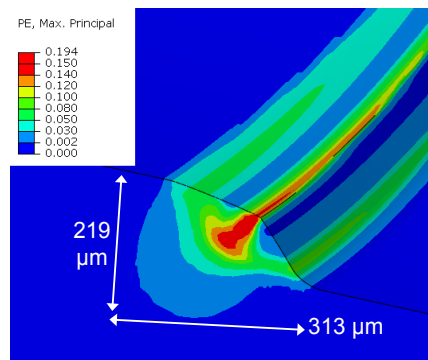


Figure 7-21. Plastic zone size and maximum principal plastic strain within spall edge of M50 NiL.

The distribution of maximum principal plastic strain is shown in Figure 7-21. The plastic zone size is 219 μm in depth and 313 μm in width and 12 % shallower than the M50 test case. The maximum plastic strain is 0.194 and 6 % lower than the M50 test case (0.206). The contributions from the initial residual hoop stress and gradient in flow curve cannot be readily determined from these analyses, but will be explored in more detail in the next section.

The key findings of this analysis are summarized here:

- Greater plastic strains are expected to result in a shorter time to crack initiation and a faster crack growth (Suresh, 2004). Greater maximum principal plastic

strains were determined for 52100 when compared to the lesser values for M50 and M50 NiL. This is indicative of the faster propagation rates observed for 52100 in all spall propagation tests.

- This observed behavior for 52100 is thought to be caused by the combined effects of the heavier ball mass (steel vs silicon nitride balls) and its lower hardness, yield strength, and flow curve inherent to 52100 bearing steel.
- The spall edge of 52100 also displayed a larger plastic zone when compared to M50 and M50 NiL. Thus more material points are experiencing cyclic plasticity, which increases the probability of crack initiation to occur in a shorter amount of time. This was observed experimentally in the faster spall propagation tests of 52100.
- Similar results in plastic strains and residual stresses were obtained for M50 NiL and M50 which agrees with the comparable spall propagation behavior observed in the spall propagation tests.
- The plastic zone depth was 30 μm deeper for the M50 test case when compared to that of M50 NiL. This may be indicative of the compressive residual stress or gradient in flow curve in M50 NiL that may prevent the plastic zone from developing in deeper regions.
- Once a crack forms and balls continue to impact the spall edge, the stress and plastic strain distribution will change dramatically. Thus the results presented here are not comprehensive.
- Although the findings from this FE analysis are supportive of what is observed experimentally, the contributions from ball mass, initial residual stress, surface hardness, and gradient in flow curve cannot be deduced from this limited set of data. The next section will investigate the contributions from each by only changing one variable at a time.

Effects of Individual Contributions

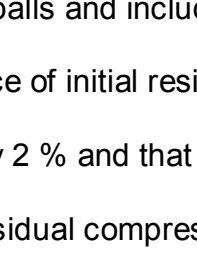
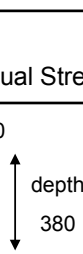
Residual Stress

The spall edge impact model will be repeated for various preconditions in order to determine the contributions from initial residual stress, gradient in flow curve, ball mass, and surface hardness. The M50 NiL test case included an initial residual compressive hoop stress of 400 MPa prior to the ball impacts. From the previous results, it was uncertain how this residual stress affected the formation and severity of the plastic

strain within the impacted spall edge because the gradient in stress strain curve and lighter ball mass were also included.

Here, the residual stress effects will be isolated by comparing the plastic strain magnitude and distribution within an impacted spall edge for various preconditions that only differ by their initial residual stress state. As an example, Table 7-1 shows the maximum principal plastic strain, the plastic zone width and depth, and the residual-tensile hoop, hydrostatic, and maximum principal stresses for two separate ball impact analyses that used steel balls and included the gradient in flow curve. The only variable is the absence or presence of initial residual stress. It is shown that the maximum plastic strain increases by 2 % and that the plastic zone depth can increase by 12 % when there is no initial residual compressive stress present.

Table 7-1. Critical stress and plastic strains for steel balls, M50 NiL gradient in flow curve is included, and with or without the compressive hoop stress prior to ball impacts. Plastic zone depth increases by 12 % when no residual stresses present.

Steel Ball, with gradient in σ - ϵ curve	With Residual Stress	Without Residual Stress	Percent Change (%)
Max Plastic Strain (%)	25.5	26.0	1.9
Plastic zone width & depth (μm)			
Max residual hoop stress (MPa)	2793	2725	-2.4
Max residual hydrostatic stress (MPa)	604	601	-0.5
Max residual principal stress (MPa)	2847	2810	-1.3

Recall from Figure 7-10 that the initial residual stresses were relatively small within the spall edge where the most severe plastic strains are forming. This explains the relatively minimal change in maximum principal plastic strain observed in this region (2%). Beneath the spall (depth = 127 μm), however, where the compressive stresses are present, the plastic zone depth has been reduced by 12 % in this test case.

Similar results are shown in Tables 7-2 and 7-3 for silicon nitride balls with the gradient in flow curve included, and for steel balls without the gradient in flow curve, respectively. Note the absence of initial compressive stress increases the plastic zone depth by as much as 13.5 % and increases the maximum principal plastic strain by as much as 4.6 %.

Table 7-2. Silicon nitride balls, with gradient in flow curve included, and with or without the initial compressive hoop stress. No initial residual stress results in a 13.5 % increase in plastic zone depth.

Silicon Nitride Ball, with gradient in σ - ϵ curve	With Residual Stress	Without Residual Stress	Percent Change (%)
Max Plastic Strain (%)	19.4	20.3	4.6
Plastic zone width & depth (μm)	width: 313 depth: 222	width: 315 depth: 252	width: 0.6 depth: 13.5
Max residual hoop stress (MPa)	2795	2748	-1.7
Max residual hydrostatic stress (MPa)	585	617	5.4
Max residual principal stress (MPa)	2864	2883	0.6

Table 7-3. Steel balls, no gradient in flow curve, and with or without the initial compressive hoop stress. No residual stress results in a 10 % increase in plastic zone depth.

Steel Ball, without gradient in σ - ϵ curve	With Residual Stress	Without Residual Stress	Percent Change (%)
Max Plastic Strain (%)	25.7	25.8	0.4
Plastic zone width & depth (μm)	width: 415 depth: 327	width: 411 depth: 360	width: -1 depth: 10
Max residual hoop stress (MPa)	2783	2761	-0.8
Max residual hydrostatic stress (MPa)	620	618	-0.3
Max residual principal stress (MPa)	2860	2933	2.5

Reduction in plastic zone volume is beneficial to materials undergoing many stress cycles as this reduces the probability of crack initiation when compared to larger plastic zones and a similar number of stress cycles. A 4.6 increase in plastic strain is not insignificant due to the exponential relationship between plastic strain and number of

cycles to crack initiation, but may not have as big of an influence as ball mass or surface hardness as will be shown later.

The residual maximum hoop, hydrostatic, and maximum principal stresses were too close in magnitude to report any significance. Due to the amount of data presented in the following tables the contour plots of the residual plastic strain and stresses will not be shown.

It is well known that initial residual compressive hoop stresses increase the fatigue life of rolling element bearings prior to fatigue spall formation (Forster et al., 2010). However, it was observed in the spall propagation experiments of Figure 7-1 where a few, but not all of the M50 specimens (no initial residual compressive stress) lasted longer than the M50 NiL specimens (initial residual compressive stress was present). This may be due to the combination of lower fracture toughness of the case hardened M50 NiL and compressive residual stresses, which together, yield similar propagation characteristics as M50 which has higher fracture toughness, but no compressive stresses.

Gradient in Stress-Strain Curve

The contributions from the gradient in stress-strain (flow) curve will now be considered. The through-hardened M50 bearing steel has a constant hardness throughout (64.5 HRC). The M50 NiL steel has a nonlinear decreasing gradient in hardness as seen visually in Figure 7-8A, but a similar surface hardness of 64.5 HRC (820Hv) as M50. From the results at the beginning of this chapter it was unclear how the gradient in flow curve affected the magnitude or distribution of plastic strain within the spall edge. It was shown in Figure 7-8A that the hardness is similar within the first 300 μm of depth and the corresponding flow curve variation was also minimal in this

region (Figure 7-8B). This causes similarities in the plastically deformed region of the impacted spall edge as shown in Tables 7-4 and 7-5 where the spall edge impact model is repeated for steel balls with and without residual stress, respectively.

Table 7-4. Effects of gradient in flow curve using steel balls and initial residual stresses are present. Plastic zone depth is only slightly deeper when gradient in flow curve is included.

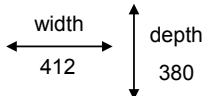
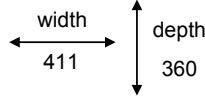
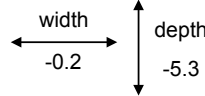
Steel Ball, with Residual Stress	With Gradient in σ - ϵ curve	Without Gradient in σ - ϵ curve	Percent Change (%)
Max Plastic Strain (%)	25.5	25.7	0.7
Plastic zone width & depth (μm)			
Max residual hoop stress (MPa)	2793	2783	-0.4
Max residual hydrostatic stress (MPa)	604	620	2.6
Max residual principal stress (MPa)	2847	2860	0.4

Here, only the gradient in flow curve is present or not for each case with all other contributions kept as constants for comparison. Results with and without the gradient in flow curve are shown in both Tables 7-4 and 7-5. Interestingly, the plastic zone is slightly deeper when there is a gradient in flow curve (Table 7-4), and also occurs when there are no residual compressive stresses present (Table 7-5). This is intuitive since the yield strength is decreasing with depth, so will the resistance to plastic deformation and consequently deeper plastic zones will develop. The maximum principal plastic strain within the spall edge is similar in magnitude (0.7%) for these cases because the gradient in yield strength is minimal within its shallow depth (127 μm).

These results suggest that the gradient in hardness does not reduce the severity of spall propagation and supports what was shown in Figures 7-1 and 7-2 where M50 NiL did not outperform M50 in the spall propagation tests. It is well known that M50 NiL exhibits a longer rolling contact fatigue than M50 prior to spall initiation (Forster et al., 2010) due to the gradient in hardness and presence of residual compressive stress, but

these effects do not appear to reduce spall propagation as seen here and in the experiments.

Table 7-5. Effects of gradient in flow curve using steel balls without initial residual stress present. Plastic zone depth is 10 % deeper when gradient in flow curve is not included.

Steel Ball, without Residual Stress	With Gradient in σ - ϵ curve	Without Gradient in σ - ϵ curve	Percent Change (%)
Max Plastic Strain (%)	26.0	25.8	-0.8
Plastic zone width & depth (μm)			
Max residual hoop stress (MPa)	2725	2761	0.8
Max residual hydrostatic stress (MPa)	601	618	0.3
Max residual principal stress (MPa)	2810	2933	2.5

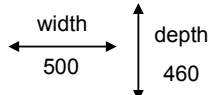
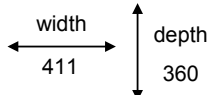
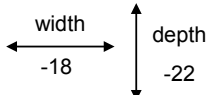
Surface Hardness

The effect of surface hardness on the extent of plastic deformation is now considered using steel balls with all other variables held constant. The results from the 52100 impact analysis are compared to M50 because the effects of residual stress and gradient in stress strain curve were not present in the 52100 and M50 bearing steels. Even though the M50 raceway was paired with ceramic silicon nitride balls in the actual spall-propagation experiments, this analysis will impact the M50 spall edge with steel balls to remove any discrepancy in ball mass. The effects of ball mass will be determined later in the next section, but for now only the effects of surface hardness (flow curve) will be considered.

As was shown in Figure 7-6 the M50 steel has a higher flow stress than 52100 by 200-300 MPa for a large range in plastic strain. The softer 52100 is then expected to experience more plastic deformation and this is observed in Table 7-6 where the plastic strain magnitude and size is shown for these two test cases. The 52100 exhibited nearly 3 % higher plastic strain in the region where cracks are observed to occur in

actual spall edges. Also the plastic zone was 22 % deeper and 18 % wider for 52100 when compared to M50. The effect of surface hardness has a larger impact on plastic deformation than initial residual stress or gradient in flow curve. These results support the spall propagation trends of Figures 7-1 and 7-2 in the sense that larger magnitudes and volumes of plastic deformation result in a reduction of the number of stress cycles to crack initiation and spall growth.

Table 7-6. Effects of surface hardness using steel balls, no initial residual stress, and no gradient in flow curve. Lower surface hardness results in larger plastic zones.

Effect of surface hardness, 52100 (62.2 HRC) and M50/M50NiL (64.5 HRC)	52100	Without Residual Stress, Without Gradient in σ - ϵ curve	Percent Change (%)
Max Plastic Strain (%)	26.5	25.8	-2.7
Plastic zone width & depth (μm)			
Max residual hoop stress (MPa)	2338	2761	18
Max residual hydrostatic stress (MPa)	484	618	27
Max residual principal stress (MPa)	2518	2933	16

Interestingly the M50 showed higher tensile residual hoop, hydrostatic, and maximum principal stress. This is due to the fact that the M50 can strain harden to higher flow stresses during plastic deformation and also has a similar elastic rebound (elastic modulus) as 52100. It is plausible that the magnitude of tensile residual stress as calculated by this method is not indicative of fatigue crack initiation in the sense that M50 displayed better spall propagation characteristics than 52100.

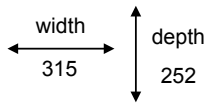
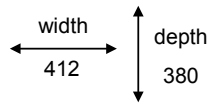
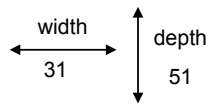
Ball Mass

Ceramic silicon nitride balls are being increasingly used in high performance bearings due to their high hardness, low density, and performance in oil-out conditions. Bearings that use ceramic balls have shown better spall propagation characteristics

than those that use heavier steel balls (Rosado et al., 2010). These effects were captured in the ball impact model in Tables 7-7, 7-8, and 7-9 where the plastic zones and residual stresses were calculated for various test cases that had the same preconditions of residual stress and gradient in flow curve, but only varied ball mass.

The maximum principal plastic strain within the spall edge was increased by as much as 31 % when a steel ball was used over a silicon nitride ball. The plastic zone width and depth also increased by as much as 33 and 53 %, respectively, when the heavier ball was simulated. The maximum principal plastic strain magnitude and distribution is indicative of the severity of damage induced by the ball impact in the form of plastic deformation. From these results it appears that ball mass has the greatest effect on spall propagation than surface hardness, residual stress, and gradient in flow curve. This is believed to be the chief reason why spalls propagated faster in 52100 than in M50 and M50 NiL.

Table 7-7. Effects of ball mass, with gradient in flow curve, and without initial residual stress. Both the maximum principal plastic strain and plastic zone size showed marked increases.

With Gradient in σ - ϵ curve, without Residual Stress	Silicon Nitride Ball	Steel Ball	Percent Change (%)
Max Plastic Strain (%)	20.3	26.0	28
Plastic zone width & depth (μm)			
Max residual hoop stress (MPa)	2748	2725	-0.8
Max residual hydrostatic stress (MPa)	617	601	-2.6
Max residual principal stress (MPa)	2883	2810	-2.5

Spall edges that undergo more plastic deformation will initiate and grow cracks sooner and faster than a spall edge that is more resistant to plastic deformation which would naturally affect spall propagation rate. This is supported by fatigue failure theories such as Coffin-Manson (Suresh, 2004) that show the number of stress cycles

required to initiate a crack decreases as the amount of plastic deformation increases. Interestingly the maximum tensile residual stress state within the spall edge did not show a marked difference with ball mass, but appears to be highly dependent on the material's flow curve as shown in the previous section.

Table 7-8. Effects of ball mass, without gradient in flow curve, and without initial residual stress. Both the maximum principal plastic strain and plastic zone size showed significant increases.

Without Gradient in σ - ϵ curve, without Residual Stress	Silicon Nitride Ball	Steel Ball	Percent Change (%)
Max Plastic Strain (%)	20.6	25.8	25
Plastic zone width & depth (μm)	width ←→ 315 depth ↑↓ 250	width ←→ 411 depth ↑↓ 360	width ←→ 30 depth ↑↓ 44
Max residual hoop stress (MPa)	2799	2761	-1.3
Max residual hydrostatic stress (MPa)	630	618	-1.9
Max residual principal stress (MPa)	2905	2933	-0.9

Table 7-9. Effects of ball mass, with gradient in flow curve, and with initial residual stress. Both the maximum principal plastic strain and plastic zone size increased.

With Gradient in σ - ϵ curve, with Residual Stress	Silicon Nitride Ball	Steel Ball	Percent Change (%)
Max Plastic Strain (%)	19.4	25.5	31
Plastic zone width & depth (μm)	width ←→ 313 depth ↑↓ 222	width ←→ 415 depth ↑↓ 340	width ←→ 33 depth ↑↓ 53
Max residual hoop stress (MPa)	2795	2793	0.0
Max residual hydrostatic stress (MPa)	585	604	3.2
Max residual principal stress (MPa)	2864	2847	-0.6

Key Points

- Based on the assumptions inherent to this investigation, ball mass appeared to have the greatest effect on the magnitude and distribution of plastic deformation within the impacted spall edge. Surface hardness was also observed to have an effect on the plastic zone size but a reduced effect on the maximum plastic strain within the spall edge. The contributions of these two effects are thought to cause the differences in spall propagation characteristics between 52100, M50, and M50 NiL of Figures 7-1 and 7-2.

- The effects of compressive hoop stress and gradient in flow curve were not so obvious. Significant compressive stresses did not develop within the spall edge in the region of large plastic strain because of the spall edge geometry. Thus similar results for maximum principal plastic strain were obtained. However, the plastic zone depth was decreased by the presence of compressive stress beneath the spall edge which may be beneficial to propagation, but a definitive conclusion cannot be made based on the data.
- The effects of the gradient in flow curve were not significant for M50 NiL since the variation in hardness is nearly constant within 300 μm of depth from the surface. The small variation in plastic response obtained from Chapter 6 within this region close to the surface, and explains why the plastic strain results were similar for the test cases examined. The plastic zone was actually deeper for the spall edges that had a gradient in plastic response because the reduction in yield strength with depth is more susceptible to plastic deformation and allows deeper plastic zones to develop.

Limitations

A few limitations of this analysis must be addressed here. A marked difference in spall propagation behavior was noticed between the life-endurance tested bearings and the virgin bearings whose spalls were initiated by Rockwell C indents. After the tens of billions of rolling contact stress cycles experienced by the raceway's ball track the flow curve of a material is expected to change due to material fatigue and cyclic hardening (or softening). This would explain the spall propagation results of the life-endurance bearings of Figure 7-3 where 52100 outperformed the M50 steels.

However, because there were only two bearings tested of each material, definitive conclusions cannot be made. Thus the flow curves used in this analysis are closer to the actual plastic behavior of the virgin bearings that had their spalls initiated by indents than naturally from billions of previous stress cycles. The FE results are supportive of the propagation trends on the virgin raceways and not the life-endurance tested bearings. The cyclic plastic flow behavior of M50 would need to be determined in order to explain this phenomenon.

Also complex bearings dynamics exist in the actual spalled bearings during bearing operation that are not accounted for here. Advanced software such as Advanced Dynamics of Rolling Elements (ADORE) is currently being developed to solve the complex problems of how a ball reloads itself between the inner and outer raceways during spall propagation which may effect the amount of damaged experienced by a spall edge.

The loading and boundary conditions of this FE model were relatively simple when compared to the many complex interactions that occur between the balls, two raceways, and bearing cage. As the spall length increases, the number of unloaded balls also increases which causes more shaft misalignment and leads to greater contact forces on the ball as it reestablishes contact between the raceways. As a spall propagates, severe vibrations occur within the engine or bearing test rig that would affect the dynamics of ball and spall edge interactions. The above mentioned complications were not taken into account in this analysis, but may have an increased effect on the damage induced on a spall edge.

Also the influences of fracture toughness were not accounted for in this analysis but may have an important effect on the rate at which these spalls propagate. The fracture toughness may also change with the large amounts of plastic deformation experienced by the spall edge and may not be accurately represented by the method that the fracture toughness was determined. However, this analysis is the first of its kind in its attempt to capture the extent of damage experienced by a spall edge during spall propagation and the contributions from residual stress, ball mass, surface hardness, and gradient in flow curve. These contributions as determined by this

method were supportive of the spall propagation characteristics of 52100, M50, and M50 NiL presented in Rosado et al. (2010).

The conclusions regarding the individual contributions from ball mass, surface hardness, residual stress, and gradient in stress strain curve are applicable to and supportive of the bearings used in the spall propagation experiments conducted by AFRL and may not apply to all possible types of bearings and operating conditions. For instance, the actual bearings used in the jet engines are much larger than the scaled versions used in the spall propagation experiments, i.e. the engine bearings have larger balls but similar case depths. Thus the gradient in hardness and compressive residual stress may have a larger contribution on spall propagation than what was seen in the smaller bearings due to the larger plastic zones that would develop for the larger balls. Also, the effects of ball mass may diminish at lower rotational speeds than those conducted in these experiments. In other words, the difference in ball momentum between ceramic and steel balls will be less for lower ball velocities but significant for high speed bearing applications.

CHAPTER 8 SUMMARY

Despite their optimized design, bearings cannot escape the damage induced by foreign object debris, improper handling, overloading, or material fatigue which can cause surface fatigue failures to occur in the form of small pits or spalls. Spalls grow and propagate with continued engine use and allow the main engine shaft to misalign leading to total engine failure and possibly loss of aircraft. Thus the amount of time between initial spallation and engine failure is of great importance to pilot safety and mission success.

Spall propagation experiments carried out by the Air Force Research Labs show that M50, M50NiL, and 52100 bearing steels have different spall propagation characteristics, but it is uncertain how certain aspects of bearing design such as initial residual stress, surface hardness, gradient in flow curve, and ball mass affect spall propagation rate. Both static and dynamic analyses were performed here to simulate these contributions and the bearing operating conditions during spall propagation.

The material properties of case hardened M50 NiL bearing steel were initially unknown and it was uncertain how its gradient in plastic response affected spall propagation that occurs within this case hardened region. A new method shown here used indentation experiments and finite element modeling to determine the plastic response of plastically graded, P675 and M50 NiL case hardened bearing steels. The gradient in plastic response was determined without knowing the plastic flow behavior of the core M50 NiL region. The method utilized a material-dependent representative plastic strain that can be used to relate indentation hardness measurements to flow

stress. It was validated for the nongraded materials 303 stainless steel and the core region of P675.

The results of the ball spall-edge impact analysis predicted large amounts of plastic strain and tensile residual stresses to occur where cracks appear in the actual spalled bearings. The contributions from ball mass were shown to have the greatest effect on the magnitude and distribution of plastic deformation within an impacted spall edge. This is supportive of the spall propagation tests of 52100 when compared to M50 and M50 NiL.

The effects of initial residual compressive stress were not significant in the calculation of the maximum principal plastic strain within the spall edge but did reduce the plastic zone size. This is due to the fact that the residual compressive stresses were small in the region where the large amounts of plastic strain develop. However, the plastic zone size was reduced because plastic deformation extended into the compressive stress region.

The effects of the gradient in flow curve were minimal due to the nonlinear subsurface trend in hardness (and flow curve) for M50 NiL which was nearly constant within 300 μm from the bearing surface and the fact that the M50 NiL and M50 have similar plastic flow behavior and hardness in the regions where spalls are forming. Thus the maximum principal plastic strains were similar by comparison. The plastic zone depth was 10 % deeper when the gradient in flow curve was included, with all other contributions kept constant. This was due to the decreasing trend in yield strength which is more susceptible to plastic deformation and consequently allows deeper plastic zones to develop.

The flow curve of a material is expected to change due to material fatigue and cyclic hardening (or softening) and this could explain the spall propagation results of the life-endurance bearings where 52100 outperformed the M50 steels. Thus the flow curves used in this analysis are closer to the actual plastic behavior of the virgin bearings that had their spalls initiated by indents rather than naturally from billions of previous stress cycles. Thus the FE results are supportive of the propagation trends of the virgin raceways and not the life-endurance tested bearings.

The FE model did not consider the many complex interactions that can occur between the balls, raceways, bearing cage, and the severe vibrations that develop during propagation. Also, the influences of fracture toughness were not accounted for in this analysis but may have an important effect on the rate at which these spalls propagate. These complications were not taken into account in this analysis due to the current lack of information regarding cyclic hardening and fatigue crack growth data for these particular bearing steels and to reduce the complexity of the model.

This analysis is the first attempt to capture the extent of damage experienced by a spall edge during spall propagation while taking into account the contributions from residual stress, ball mass, surface hardness, and gradient in flow curve. These contributions as determined by this method were supportive of the spall propagation characteristics of 52100, M50, and M50 NiL presented in Rosado et al. (2010).

APPENDIX
INDENTATION DATA

Table A-1. Micro Vickers indent field below macro indent of hard to soft PGM of P675 case hardened region.

Depth from surface (µm)	Raceway surface indent produced at 328.24 kg, indent diagonal ~ 800 µm.														
	-800	-700	-600	-500	-400	-300	-200	-100	0	100	200	300	400	500	600
120	921	930	930	930	907	900	910	X	X	X	905	900	909	918	922
220	905	901	923	910	891	896	896	909	918	900	890	886	885	909	922
320	864	872	881	874	880	878	878	896	900	880	867	865	878	878	874
420	825	821	840	845	849	856	857	870	870	861	853	845	840	849	837
520	788	791	821	810	804	821	829	829	838	820	820	810	813	805	825
620	755	760	784	777	773	780	798	799	800	784	784	770	780	773	784
720	726	728	736	740	736	739	740	742	748	757	753	739	739	733	739
820	704	710	692	713	707	710	710	720	716	704	707	717	713	713	710
920						683	680	704	695	674	672	677			
1020						650	660	660	659						
1120						623	630	623	620						
1220						601	589	596	604						

Table A-2. Micro Vickers indent field below macro indent of soft to hard PGM of P675 case hardened region.

Reverse raceway surface indent produced at 230 kg, indent diagonal ~ 890 µm (depth ~ 120 µm)											
Depth (µm)	-500	-400	-300	-200	-100	0	100	200	300	400	500
220	526	525	526	535	537	536	536	536	515	517	524
320		558	560	559	539	568	537	555	526	530	
420		564	564	565	567	578	563	555	555	556	
520					590	593	600				
620					610	605	612				
720						629					
820						663					
920						689					
1020						720					

LIST OF REFERENCES

- ASM Handbook, <http://products.asminternational.org/hbk/index.jsp>, June 9, 2009.
- Antunes J.M., Fernandes J.V., Menezes L.F., Chaparro B.M., 2007. A new approach for reverse analyses in depth sensing indentation using numerical simulation. *Acta Materialia*. 55, 69-81.
- Averbach, B.L., Lou, B., Pearson, P.K., Fairchild, R.E., Bamberger, E.N., 1985. Fatigue crack propagation in carburized high alloy bearing steels. *Metallurgical Transactions A*, 16A, 1253-1265.
- Arakere, N. K., Branch, N., Levesque, G., Svendsen, V., Forster, N.H., 2010. On the Rolling Contact Fatigue Life and Spall Propagation Characteristics of M50, M50 NiL and 52100 Bearing Materials: Part II: Stress Modeling, *Tribology Transactions*. 53, 1, 42-51.
- Baxevani E.A., Giannakopoulos A.E., 2009. The Modified Rockwell Test: A New Probe for Mechanical Properties of Metals. *Experimental Mechanics*. 49. 371-382.
- Beswick, J.M., 1989. Fracture and fatigue crack propagation properties of hardened 52100 steel. *Metallurgical Transactions A*, 20A, 1961-1973.
- Boresi A., Schmidt R.J., 2003. *Advanced Mechanics of Materials*. 6th ed. John Wiley and Sons
- Branch, N.A., Arakere, N.K., Svendsen, V., Forster, N.H., 2010. Stress field evolution in a ball bearing raceway fatigue spall. *Journal of ASTM International*. 7, No. 2.
- Bucaille J.L., Felder E., 2002. Finite-element analysis of deformation during indentation and scratch tests on elastic perfectly plastic materials. *Philosophical Magazine A*. 82. No 10. 2003-2012.
- Bucaille J.L., Stauss S., Felder E., Michler J., 2003. Determination of plastic properties of metals by instrumented indentation using different sharp indenters. *Acta Materialia*. 51. 1663-1678.
- Cao T., Huber N., 2006. Further investigation on the definition of the representative strain in conical indentation. *Journal of Materials Research*. 21. No 7. 1810-1821.
- Cao, Y. P., and Lu, J., 2004. A New Scheme for Computational Modeling of Conical Indentation in Plastically Graded Materials. *J. Mater. Res.*, 19 (6). 1703-1716.
- Carpenter. www.carttech.com. September 15, 2009. "Hot Tensile Properties of Carpenter VIM VAR M50 Bearing Steel"
- Chaudhri M.M., 1998. Subsurface strain distribution around Vickers hardness indentations in annealed polycrystalline copper. *Acta Materialia*, 46, No 9, 3047-3056.

Choi, I. S., Dao, M., and Suresh, S., 2008. Mechanics of Indentation of Plastically Graded Materials – I: Analysis. *J. Mech. Phys. Solids*, 56 (1). 157-171.

Choi, I. S., Detor, A. J., Schwaiger, R., Dao, M., Schuh, C. A., and Suresh, S., Mechanics of Indentation of Plastically Graded Materials – II: Experiments on Nanocrystalline Alloys with Grain Size Gradients. *J. Mech. Phys. Solids*, 56 (1).172-183.

Chollacoop N., Dao M., Suresh S., 2003. Depth-sensing instrumented indentation with dual sharp indenters. *Acta Materialia*. 51. 3713-3729.

Chollacoop N., Ramamurty U., 2005. Experimental assessment of the representative strains in instrumented sharp indentation. *Scripta Materialia*. 53. 247-251.

Dao M., Chollacoop N., Van Vliet K.J., Venkatesh T.A., Suresh S., 2001. Computational Modeling of the Forward and Reverse Problems in Instrumented Sharp Indentation. *Acta Materialia*. 49. 3899-3918.

Fischer-Cripps, A.C., 2006. Critical review of analysis and interpretation of nanoindentation test data. *Surface and Coatings Technology*. 200. 4153-4165.

Forster,N.H., Ogden,W.P., Trivedi, H.K., 2010. On the Rolling Contact Fatigue Life and Spall Propagation Characteristics of M50, M50 NiL and 52100 Bearing Materials: Part III - Metallurgical Examination. *Tribology Transactions*. 53, No. 1. 52-59.

Gao X.L., Jing X.N., Subhash G., 2006. Two expanding cavity models for indentation deformations of elastic strain hardening materials. *International Journal of Solids and Structures*. 43. 2193-2208.

Gao, X.L., Wei, X., X., 1991. An exact elasto-plastic solution for a thick walled spherical shell of a strain hardening material. *Pressure vessels and components*. PVP ASME Press, New York, 217. 75-79.

Giannakopoulos, A. E., 2002. Indentation of Plastically Graded Substrates by Sharp Indenters. *Int. J. Solid and Structures*, 39 (9). 2495-2515.

Gu, Y., Nakamura, T., Prchlik, L., Sampath, S., and Wallace, J., 2003. Micro-Indentation and Inverse Analysis to Characterize Elastic-Plastic Graded Materials. *Mater. Sci. Eng. A*, 345 (1-2). 223-233

Hamrock B.J., Dowson D., *Ball Bearing Lubrication*. 1981. John Wiley and Sons

Harris, T.A., *Rolling Element Bearings*. 3rd edition. 1991. John Wiley and Sons

Hill, R., 1950. *The mathematical theory of plasticity*. Oxford Univ. Press.

Hirst, W., Howse, M.G.J.W. 1969. The indentation of materials by wedges. *Proc. Roy. Soc. A* 311, 429-444.

Hoeprich, M.R., 1992. Rolling Element Bearing Fatigue Damage Propagation. ASME Journal of Tribology, 114, April, 328-333.

Howell, M.B., Rubin, C.A., Hahn, G.T., 2004. The Effect of Dent Size on the Pressure Distribution and Failure Location in Dry Point Frictionless Rolling Contacts. ASME Journal of Tribology, July, 126, 413-421.

Ioannides, E., and Harris, T., 1985. A New Fatigue Life Model for Rolling Bearings. ASME Journal of Tribology, 107, 367-378.

Jayaraman S., Hahn G.T., Oliver W.C., Rubin C.A., Bastias P.C. 1998. Determination of Monotonic Stress Strain Curve of Hard Materials from Ultra-low-load Indentation Tests. International Journal of Solids and Structures. 35. (5-6). 365-381.

Johnson, K.L. 1987. Contact Mechanics, Cambridge Press, Cambridge. 361-366.

Koeppel, B.J., Subhash, G., 1999. Characteristics of residual plastic zone under static and dynamic Vickers indentations. Wear. 224. 56-67.

Kotzalas, M., Harris, T.A. 2001. Fatigue Failure Progression in Ball Bearings, Trans. ASME. 123, 238-242.

Lai, M.O., Lim, K.B. 1991. On the prediction of tensile properties from hardness tests. Journal of Materials Science. 26 (8). 2031-2036.

Lundberg, G., and Palmgren, A. 1947. Dynamic Capacity of Rolling Bearings. Acta Polytechnica, 1 (3).

Marsh, D.M., 1964. Plastic flow in glass. Proc. R. Soc. Lond. A 279. 420-435.

Nakamura, T., Wang, T., and Sampath, S., 2000. Determination of Properties of Graded Materials by Inverse Analysis and Instrumented Indentation. Acta Materialia, 48 (17). 4293-4306.

Nayebi, A., El Abdi, E., Bartier, O., and Mauvoisin, G. 2002. Hardness Profile Analysis of Elasto-Plastic Heat-Treated Steels with a Gradient in Yield Strength. Mat. Sci. and Eng. A333. 160-169.

Ogasawara N., Chiba N., Chen X., 2006. Measuring the plastic properties of bulk materials by single indentation test. Scripta Materialia. 54. 65-70.

Ogasawara N., Chiba N., Chen X., 2005. Representative strain of indentation analysis. Journal of Materials Research. 20 (8). 2225-2234.

Ogasawara N., Chiba N., Zhao M., Chen X., 2007. Measuring Material Plastic Properties with Optimized Representative Strain-Based Indentation Technique. Journal of Solid Mechanics and Materials Engineering. 1 (7). 895-906.

Pavlina E.J., Van Tyne C.J., 2008. Correlation of Yield Strength and Tensile Strength with Hardness for steels. ASM International. 17. 888-893.

Rosado, L., Forster, N., Thomson, K. 2010. On the Rolling Contact Fatigue Life and Spall Propagation Characteristics of M50, M50 NiL and 52100 Bearing Materials: Part I - Experimental Results. Tribology Transactions. 53. 29-41.

Sadeghi, F., Jalalahmadi, B., Slack, T. S., Raje, N., Arakere, N. K. 2009. A Review of Rolling Contact Fatigue. ASME Journal of Tribology. 131 (4). 1-15.

Sonmez F., Demir A. 2007. Analytical relations between hardness and strain for cold formed parts. Journal of Materials Processing Technology. 186. 163-173.

Srikant G., Chollacoop N., Ramamurty U. 2006. Plastic strain distribution underneath a Vickers indenter: role of yield strength and work hardening exponent. Acta Materialia. 54. 5171-5178.

Stickels, C.A., 1977. Plastic deformation of quenched and tempered 52100 bearing steel in compression. Metallurgical Transactions A. 8A. 63-70.

Suresh, S., Fatigue of Materials. 2004. 2nd Ed. Cambridge University Press

Tabor D., 1970. The Hardness of Solids. Review of Physics in Technology. Surface Physics, Cavendish Laboratory, Cambridge. 145-179.

Tekkaya A.E. 2000. An improved Relationship between Vickers Hardness and Yield Stress for Cold Formed Materials and its Experimental Verification. CIRP Annals-Manufacturing Technology. 1 (1). 205-208.

Tho., K.K., Swaddiwudhipong, S., Liu, Z.S., Zeng, K., 2005. Simulation of instrumented indentation and material characterization. Materials Science and Engineering. A 390. 202-209.

VanLandingham M.R., 2003. Review of Instrumented Indentation. Journal of Research of the National Institute of Standards and Technology. 108 (4). 249-265.

Xu, G., Sadeghi, F. 1996. Spall initiation and propagation due to debris denting, Wear, 201, 106-116.

Zaretsky, Erwin V., 1996. Comparison of Life Theories for Rolling Element Bearings. Tribology Transactions, 39, 2, 237-248.

BIOGRAPHICAL SKETCH

Nathan Branch was born and raised in south Louisiana. He graduated magna cum laude from Louisiana State University with an undergraduate degree in mechanical engineering. He served as President of the LSU student chapter of the American Society of Mechanical Engineers as a senior. Nathan then moved to Gainesville, Florida and was admitted to the Ph.D. program at the University of Florida's Mechanical and Aerospace Engineering department. He worked at the Propulsion Directorate and Turbine Engine Division at the Air Force Research Laboratory at Wright Patterson Air Force Base, Ohio for two summers while in graduate school. Nathan also completed his Master of Science degree in mechanical engineering at the University of Florida. Nathan enjoys reading, exercising, and mountain biking at San Felasco.